Cosmic Voids in Large-Scale Structure Surveys

Giorgia Pollina

München 2018

Cosmic Voids in Large-Scale Structure Surveys

Giorgia Pollina

Dissertation
an der Fakultät für Physik
der Ludwig–Maximilians–Universität
München

vorgelegt von
Giorgia Pollina
aus Como

München, den 10.8.2018

Erstgutachter: Prof. Dr. J. Weller
Zweitgutachter: Prof. Dr. K. Dolag
Tag der mündlichen Prüfung: 05.10.2018

ZUSAMMENFASSUNG

Das aktuelle Standardmodell der Kosmologie beruht auf zwei grundlegenden Fundamenten: zum einen auf dem Vorkommen einer nichtrelativistischen (kalten), nur gravitativ wechselwirkenden (dunklen) Form der Materie - besser bekannt als Kalte Dunkle Materie (CDM) - und zum anderen auf der Existenz eines *unbekannten Fluids*, welches das gesamte Universum durchsetzt und dessen späte Dynamik auf sehr großen Skalen dominiert. Die CDM ist für die Erschaffung der Potentialtöpfe verantwortlich, in denen Baryonen kühlen und kondensieren können, um all die Galaxien zu bilden, welche wir am Himmel beobachten. Das *unbekannte Fluid* ist die sogenannte Dunkle Energie (DE) - welche die Beschleunigung der derzeitigen Ausdehnung des Universums antreibt - in ihrer einfachsten Form: eine Konstante, Λ.

Dieses ΛCDM-Modell ist allerdings sehr erfolgreich, da es genaue Vorhersagen macht und den Großteil aller verfügbaren Beobachtungen korrekt beschreibt. Die sechs Parameter, auf denen das ΛCDM-Modell fußt, können mit derart hoher Genauigkeit gemessen werden, dass Physiker heute von einer ära der "Präzisionskosmologie" sprechen. Obwohl die Leistungsfähigkeit dieses Modells ausgesprochen bemerkenswert ist wird oft vergessen, dass die Errungenschaften von ΛCDM auf den zwei obigen Fundamenten basieren, deren Ursprung immer noch völlig unbekannt ist.

Sowohl DE, als auch CDM können mithilfe großräumiger Strukturen (LSS) des Kosmos erforscht werden. Insbesondere der Einfluss von Λ auf die LSS des Universums wird schon seit Jahrzehnten studiert, wobei der Fokus hauptsächlich auf die statistischen Eigenschaften der massivsten Objekte (Galaxienhaufen) gelegt wurde. Seit einigen Jahren ist es auch möglich geworden dieses Bestreben auf die Statistik großer Regionen geringer Materiedichte im Universum auszuweiten, sogenannter kosmischer Leerräume. In diesen Gebieten, wo kaum Materie vorhanden ist, dominiert DE, ein Umstand der Leerräume möglicherweise zu den besten Kandidaten macht, um Licht auf den Ursprung der DE zu werfen.

Um die Statistik der Leerräume für kosmologische Zwecke gänzlich ausschöpfen zu können ist ein umfassendes Verständnis darüber vonnöten, wie diese von den begrenzten Informationen beeinflusst wird, welche wir direkt von Beobachtungen leuchtender Himmelsobjekte erhalten; dies ist der Gegenstand dieser Dissertation. Vor einer derartigen Analyse ist es jedoch hilfreich, sich zunächst den Grundaufbau des ΛCDM-Modells ins Gedächtnis zu rufen.

Der erste Teil dieser Doktorarbeit ist der Zusammenfassung von den theoretischen Konzepten und Beobachtungen gewidmet, die zur Etablierung des heutigen Standardmodells geführt haben. Nach einem kurzen überblick zu allen Annahmen des Standardmodells wird in Kapitel 1 die Beschreibung des Universmums als Ganzes besprochen, indem die Theorie der Gravitation und die wichtigsten Entdeckungen diskutiert werden, auf welchen diese Beschreibung aufbaut. In Kapitel 2 wird das Thema der Strukturbildung behandelt: wir umreißen die Entwicklung kleiner Dichteschwankungen zu kollabierten Halos und ausgedehnten Leerräumen, fassen die theoretischen Grundlagen zusammen, die für die Erforschung großräumiger Strukturen in unserem Kosmos notwendig sind, und führen schließlich das Konzept des tracer bias ein.

Im zweiten Teil dieser Arbeit wird der eigenständige Beitrag zu diesem Themengebiet präsentiert. In Kapitel 3 wird ein Test basierend auf Simulationen konkurrierender kosmologischer Modelle behandelt. Wir zeigen auf, dass obwohl Leerraum-Statistiken formal die Effekte einer möglichen (fünften Kraft) modifizierten Gravitation wahrnehmen, diese nicht zwischen verschiedenen Modellen der dunklen Energie unterscheiden können, wenn die Leerräume mithilfe von nicht repräsentativen Objekten der Materieverteilung identifiziert werden, wie beispielsweise kollabierten Halos aus dunkler Materie. Das Ergebnis der Forschungsarbeit in Kapitel 3 ist, dass ein Modell zur Einbindung des tracer bias in die Leerraum-Statistik notwendig ist, um Leerräume zur Erforschung des Ursprungs der dunklen Energie zu verwenden.

In Kapitel 4 wird ein erster Versuch vorgestellt, wie die Eigenschaften von Leerräumen, welche in der Verteilung leuchtender Objekte identifiziert werden, mit Leerräumen in der gesamten Materieverteilung in Verbindung gebracht werden können. Durch Analyse des mittleren Dichteprofils von Leerräumen, welche in der Verteilung leuchtender tracer einer hydrodynamischen Simulation definiert wurden, ermitteln wir eine lineare Beziehung zu der zugrunde liegenden Materieverteilung. Wir stellen fest, dass für die größten Leerräume lediglich der lineare bias als einziger Parameter vonnöten ist, um die beiden Verteilungen zu verknüpfen.

In Kapitel 5 wird eine erstmalige experimentelle überprüfung der Resultate aus Kapitel 4 vorgestellt. Zu diesem Zweck verwenden wir Daten des Dark Energy Survey, der derzeit größten Beobachtungskampagne für LSS. Da die räumliche Verteilung der gesamten Materie im Universum nicht direkt beobachtbar ist, beruht unsere Analyse auf den relativen Eigenschaften von Leerräumen, welche durch unterschiedlich repräsentative Haufen definiert sind. Es wird nachgewiesen, dass das lineare Verhalten in diesem Falle ebenfalls besteht. Als Nebenprodukt dieser Arbeit beurteilen wir den Einfluss photometrischer Messungenauigkeiten auf die Identifikation von Leer-

räumen in drei Dimensionen und schlagen eine konsistente Methode vor, welche den Fehler von Distanzmessungen in Leerraum-Statistiken vermindert.

Kapitel 6 fasst alle Resultate zusammen und gibt einen Ausblick auf zukünftige Forschungsarbeit.

ABSTRACT

The current standard cosmological model is based on two fundamental pillars: the existence of a non-relativistic (Cold) gravitationally interacting only (Dark) type of Matter - better know as Cold Dark Matter (CDM) - and the presence of an *unknown fluid* that permeates the Universe and dominates its late-time dynamics on very large scales. The CDM is responsible for the production of the potential wells in which baryons can cool and condense to form the galaxies that we observe in the sky. The *unknown fluid* is the so-called Dark Energy (DE) - which powers the acceleration in the present expansion of the Universe - in its simplest form: that of a constant, Λ.

ΛCDM is indeed a successful model, capable of making sensible predictions and correctly describing most of the available observations. The six parameters which ΛCDM relies on can be measured to such a high accuracy that physicist often refer to the current epoch as "precision cosmology" era. Although the effectiveness of this model is incredibly remarkable, we tend to forget that the accomplishments of ΛCDM lay on top of the two pillars we introduced earlier, the nature of which remains completely unknown.

Both DE and CDM can be studied via the Large Scale Structure (LSS) of the Cosmos. In particular, the impact of Λ on the LSS of the Universe has being studied for decades, mainly focusing on how statistical properties of the most massive objects (clusters of galaxies) are affected by it. Nevertheless in recent years it was possible to extend this effort to the statistics of the very large and low density regions of the Universe, known as cosmic voids. In such locations, mostly devoid of matter, DE is dominant, possibly indicating that voids are the best candidates to shed light on its nature.

To fully exploit void statistics for cosmological purposes, it is necessary to have a comprehensive understanding of how they are influenced by the limited information we can access directly observing luminous tracers, which is the subject of this dissertation. Before describing such effort, it is convenient to recall how the ΛCDM framework is constructed.

The first part of this thesis is dedicated to the summary of the theoretical concepts and observational evidence that has led to the establishment of the current concordance model. More specifically, after a brief synopsis of all the assumptions of the standard model, in Chapter 1 we review the description of our Universe as a whole, by revising the theory of gravity and the major discoveries on which such description is based. In Chapter 2 we outline the topic of structure formation: we will sketch the evolution of a small density fluc-

tuations to collapsed halos and empty voids, sum up the theoretical background necessary to study of the LSS of our Cosmos, and finally introduce the concept of tracer bias.

In the second part of this work, we present our original contribution on these matters. Namely, in Chapter 3 we describe a test run with simulations of competing cosmological models. We demonstrate that while void statistics are formally sensible to the effect of a possible deviation from a vanilla ΛCDM, they are unable to discriminate between different dark energy models if voids are traced in a sample of biased objects, such as collapsed dark matter haloes. The conclusion of the research project presented in Chapter 3 is that a paradigm to include the tracer bias into the void statistics is needed, if we want to employ voids to study the nature of dark energy.

In Chapter 4 we present a first attempt to model how properties of under-densities traced in luminous objects can be linked to the matter under-density. Studying the average density profiles of voids defined in samples of luminous tracers extracted from a hydro-dynamic simulation, we assessed its linear relation to the underlying matter density. We determine that, for the largest voids in the sample, the only parameter necessary to link the two statistics is the linear bias.

In Chapter 5, we report a first observational test of the findings presented in Chapter 4. To this end we employ data by the Dark Energy Survey, currently the largest LSS survey available. As the three-dimensional distribution of matter in the Universe is not directly observable, we rely on the relative properties of voids traced with differently biased clusters. We establish that the linearity in this case also holds. As a by-product of our work, we evaluate the impact of photometric uncertainty on three-dimensional void-finding and propose a consistent method to trace voids, which mitigates the error from distance estimation in void statistics.

In Chapter 6 we review all results and provide an outlook to future work.

CONTENTS

LIST OF TABLES

Part I

INTRODUCTION

In the first part of this thesis is dedicated to the summary of classical cosmological topics.

1

THE HOMOGENEOUS UNIVERSE

Cosmology is arguably among the most challenging branches of physics that mankind has ever dared to confront: the quest of explaining the whole Universe - *the totality of existing things* - from the beginning of time, up to when these words are written, cannot be described differently. Perhaps by capturing the task of Cosmology with these words, we might understand why the current standard cosmological model, incapable of assessing the nature of $\approx$ 95% of the Cosmos, is considered incredibly successful. In fact, although many fundamental constituents of this model remain greatly mysterious from a fundamental physics point of view, the effectiveness of the minimal 6-parameter ΛCDM model is striking to the limit of the unthinkable: spanning from the last scattering surface to the present day, from few Mpc scale to the Hubble Scale, all the information we have gathered in the last two decades about our Cosmos reasonably fit into the prescriptions of ΛCDM, and have delineated its indisputable establishment.

The major general assumptions which the concordance model relies on are the following:

- physics is the same throughout the observable Universe, which - on large scales - is statistically homogeneous and isotropic everywhere (see the Section 1.1);
- General Relativity provides an adequate description of gravity all over the Cosmos;
- the Universe has been expanding since early times, and it was once hotter and denser;
- there are 5 basic cosmological ingredients:
  - Dark Energy, which behaves like energy density of the vacuum;
  - Cold Dark Matter, which interacts with regular matter only gravitationally, and it is pressure-less for structure formation purposes;
  - atomic matter, that behaves just like on Earth;
  - photons;
  - neutrinos, that are almost mass-less;

- the early Universe was endowed with density fluctuations at early times, that are Gaussian, adiabatic, and nearly scale invariant;
- the observable Universe has a simple topology (i. e. trivial like $\mathbb{R}^3$);
- the Cosmos is (very close to) flat[1];

Relying on these assumptions a large variety of observations can be predicted with a small number of parameters.

In this first part of the thesis we provide an overview on how these assumption were placed and tested, leading to the construction of the concordance model. In this chapter we focus in particular on the description of the Universe as a single entity. In the summary of the topics covered in Chapter 1, we follow the work of Baldi [12] (chapter 1), Mana [126] (chapter 1), Weller [218] (chapter 1), Komatsu [109] (chapter 1).

1.1 THE COSMOLOGICAL PRINCIPLE

The cosmological principle: why gravity is our only concern (for now)

The very first assumption on which cosmology is based has somewhat an historical and philosophical taste. The *cosmological principle*, in fact, states that there is no privileged position nor direction in the space-time, or, analogously, that the Universe is *homogeneous* and *isotropic*. In our everyday life we have the clear experience that does not apply locally and, in fact, such assumption has to be intended true on very large scales (larger than $\approx 1000\,\mathrm{Mpc/h}$). In perfect contradiction with the geocentric and anthropocentric view of the World in place for hundreds of years, the cosmological principle states that there are no "special locations" in the Universe, which is remarkably helpful to make a first step in the direction of modeling it.

The cosmological principle furthermore guarantees that to describe the background evolution of the Universe our only concern should be gravity, i. e. the only interaction that can play a role at such large scale. The most general and comprehensive theory of gravity at our hands is *General Relativity* (GR) [70]. We shall thereby present how, starting from the General Theory of Gravitation, we can write down the equations that follow the evolution of the Universe.

1 Generally speaking, ΛCDM allows deviation from a flat Universe. However, curvature is measured to be very small. Therefore, this might be considered an assumption as much as constraint, but operatively one might simply assume the Universe to be flat as a consequence of an early inflationary expansion stage of the Cosmos.

1.2 THEORY

NOTATION CHOICE In this thesis we will always assume that:

- greek indeces span over the space-time components, e. g. $\nu = (0, 1, 2, 3)$;
- latin indeces span over the space-space component, e. g. $i = (1, 2, 3)$;
- our convention for the metric signature is $(-, +, +, +)$;
- the Planck system of units is valid (unless otherwise stated),i. e. $\hbar = c = 1$;
- a dot on top of a function indicates its derivative with respect of time, e. g. $\dot{x} \equiv \frac{dx}{dt}$, $\ddot{x} \equiv \frac{d^2x}{dt^2}$.

1.2.1 *General Relativity*

The equation at the very basis of the dynamic of the Universe is the field equation of GR, that links the geometrical properties of the space time with its energy content. Such equation reads as follows:

The field equation of general relativity

$$G_{\mu\nu} = \kappa^2 T_{\mu\nu} \tag{1.2.1}$$

where $\kappa^2 \equiv 8\pi G$, G being the Newton's gravitational constant.

On the left hand side of Equation 1.2.1 the *geometrical properties* of the space-time are reported. They are encoded in the *Einstein Tensor*, defined as:

The left-hand side: the geometrical properties of the Universe

$$G_{\mu\nu} \equiv R_{\mu\nu} - \frac{1}{2} R g_{\mu\nu} \tag{1.2.2}$$

where two contraction of the *Riemann Tensor* $R^{\sigma}_{\lambda\mu\nu}$ that appear in Equation 1.2.1 are the *Ricci Tensor*

$$R_{\mu\nu} \equiv R^{\sigma}_{\mu\sigma\nu}\,, \tag{1.2.3}$$

and the *Curvature Scalar*

$$R \equiv R^{\mu}_{\mu} = g^{\mu\nu} R_{\mu\nu}\,, \tag{1.2.4}$$

while $g_{\mu\nu}$ is the 4×4 *metric tensor* constituted by ten independent components (the time-time component g_{00}, three space-time components g_{0i} and six space-space components g_{ij}).

The geometry of the space-time is determined by the term on the right hand side of Equation 1.2.1, where all the information on the energy distribution of the Universe are reported within the *Stress-Energy Tensor*. For a perfect fluid in its own rest-frame with pressure p, energy density ρ and 4-velocity u_μ the Stress-Energy Tensor is given by:

The right-hand side: the energy content of the Universe

$$T_{\mu\nu} = (\rho + p)u_\mu u_\nu + p\rho_{\mu\nu} \,. \tag{1.2.5}$$

The Equation of State (EoS) of perfect fluids is given by the ratio of their pressure and energy density:

$$w \equiv \frac{p}{\rho} \,. \tag{1.2.6}$$

Different kind of fluids are present in the Universe, each of them with its own EoS. The stress energy tensor incorporates all of the components in the Cosmos so it simply amounts to the sum of multiple terms like Equation 1.2.5, each with its specific value of p and ρ. For future purposes, it is worth recalling that ordinary perfect fluids fulfill the *Strong Energy Condition*:

The Strong Energy Condition

$$\rho + 3p \geqslant 0 \,. \tag{1.2.7}$$

Equation 1.2.1 clarifies how the energy content (or matter) and geometry (or space) interact in the GR framework: matter takes care of bending the space, determining its curvature; the space-time geometry, on the other hand, configures the dynamic of its matter content. Ultimately, the Field Equation of GR sets a general perspective of Cosmology: by determining the content of the Universe we can deduce its intrinsic properties.

1.2.2 *Friedmann-Lemaître-Robertson-Walker Metric*

To completely determine how the Universe evolves we must choose a metric and solve Equation 1.2.1. The metric tensor $g_{\mu\nu}$ defines the *line element* of the space time as:

$$ds^2 = g_{\mu\nu} dx^\mu dx^\nu \,. \tag{1.2.8}$$

The cosmological principle allows us to slice the Universe in space-like hypersurfaces that are homogeneous and isotropic on large scales. This defines a global time-like parameter called *Cosmic Time*, t, which is constant for all hypersurfaces and, for all practical purposes, can

Cosmic Time and Scale Factor

be considered a global time variable. This furthermore allows us to simply express the line element of space-time by confining the time dependency of the metric tensor within a single function of the cosmic time, also known as the *Scale Factor* $a(t)$:

$$ds^2 = dt^2 - a^2(t)dl^2 \,. \tag{1.2.9}$$

The line element in comoving spatial polar coordinates

When switching to comoving spatial polar coordinates (r, θ, ϕ), the line element can be re-written as

$$ds^2 = dt^2 - a(t)\left[\frac{dr^2}{1-Kr^2} + r^2(d\theta^2 + sin^2\theta d\phi^2)\right] \,, \tag{1.2.10}$$

known as the *Friedmann-Lemaître-Robertson-Walker* metric [FLRW, 80, 83, 119, 177]. K embodies the *Curvature* of the space-like hypersurfaces of constant cosmic time. The three values that K can assume correspond to different curvatures and geometries, namely:

Curvature and geometry

$$\begin{aligned} K = -1&\text{: negative curvature, hyperbolic geometry} \\ K = 0&\text{: no curvature, Euclidean geometry} \\ K = +1&\text{: positive curvature, spherical geometry} \end{aligned} \tag{1.2.11}$$

1.2.3 *The Friedman equations*

Employing the FLRW metric (Equation 1.2.10), Christoffel symbols, Ricci Tensor and Ricci Scalar can be computed and inserted in the Field Equation, Equation 1.2.1. By solving the time-time component G_{00} and the space-space components G_{ij} we obtain the *Friedmann Equations* (FE), that, following the evolution of $a(t)$, describe the dynamic of the Universe as whole. These equations read:

$$\frac{\dot{a}^2}{a^2} = \frac{\kappa^2}{3}\left(\rho_k + \sum_i \rho_i\right) \,, \tag{1.2.12}$$

$$\frac{\ddot{a}}{a} = -\frac{\kappa^2}{6}\sum_i (\rho_i + 3p_i) \,, \tag{1.2.13}$$

where ρ_k is the curvature density, defined as

$$\rho_k \equiv -\frac{3}{\kappa^2}\frac{K}{a^2} \,, \tag{1.2.14}$$

and ρ_i and p_i are the energy density and the pressure of each fluid[2] in the Universe, respectively. Since ordinary perfect fluids obey the Strong Energy Condition presented in Equation 1.2.7, it is straight

Static solution missing

forward to understand that the Friedman Equations as written in Eqs. 1.2.12 and 1.2.13 cannot have a static solution: the second derivative of the scale factor will always be negative if ordinary perfect fluids only are included in the left hand side of the second Friedmann Equation.

1.2.4 *The cosmological constant*

The lack of static solutions to the Friedmann Equations led Einstein to introduce, in 1917, a *Cosmological Constant* term, Λ, in the field equation [71]. Λ must effectively produce a negative pressure capable of balancing the pull of gravity. With this revision, the field equation Equation 1.2.1 becomes:

The field equation of GR revisited

$$\hat{G}_{\mu\nu} \equiv R_{\mu\nu} - \frac{1}{2}Rg_{\mu\nu} + \Lambda g_{\mu\nu} = G_{\mu\nu} + \Lambda g_{\mu\nu}\,. \tag{1.2.15}$$

The introduction of the cosmological constant might look like a mere artefact, advocated *ad hoc* by Einstein to enforce the possibility of recovering a static solution to the Friedmann Equations. Nevertheless, a Cosmological Constant term is formally allowed by the theory, since it can arise as a constant of integration. In fact the most general action, S, that can be written in terms of the metric tensor $g_{\mu\nu}$ (being g its determinant) and of its first and second derivatives with respect to the space-time coordinate x^μ is:

The Cosmological Constant as a constant of integration

$$S = \frac{1}{2\kappa^2}\int d^4x\sqrt{-g}(R - 2\Lambda + \mathcal{L}) \tag{1.2.16}$$

where Λ is a constant and $\mathcal{L}$ is the Lagrangian density of all the various energy fields in the Universe. The field equation of General Relativity can be obtained by applying the *Least Action Principle* to Equation 1.2.16 in the following form

$$\hat{G}_{\mu\nu} = \kappa^2 T_{\mu\nu}\,, \tag{1.2.17}$$

where $\hat{G}_{\mu\nu}$ is defined as presented in Equation 1.2.15. The field equation we initially introduced in Equation 1.2.1 is derivable by setting $\Lambda = 0$.

A fluid-component named Λ

The Cosmological Constant term can be moved to the right hand side of Equation 1.2.17: in this case Λ is formally treated like new fluid in the Universe, i. e. an additional component to those described by the Lagrangian $\mathcal{L}$. By doing so the field equation can be further rewritten as follows

2 Typically $i = (r, m)$, i. e. radiation, r and matter m.

$$G_{\mu\nu} = \kappa^2 \hat{T}_{\mu\nu} \equiv \kappa^2 \left(T_{\mu\nu} - \frac{\Lambda}{\kappa^2} g_{\mu\nu} \right) . \tag{1.2.18}$$

The energy density and pressure to be associated to Λ, ρ_Λ and p_Λ respectively, are determined applying stress energy tensor equation presented in Equation 1.2.5 to $\hat{T}_{\mu\nu}$ and they amount to

$$\rho_\Lambda = \frac{\Lambda}{\kappa^2} , \tag{1.2.19}$$

$$p_\Lambda = -\frac{\Lambda}{\kappa^2} , \tag{1.2.20}$$

Equation of State of the Λ-component

implying for the Λ-fluid an EoS

$$w = \frac{p_\Lambda}{\rho_\Lambda} = -1 \tag{1.2.21}$$

which violates the Strong Energy Condition presented in Equation 1.2.7. Such property constitutes a peculiarity of the Cosmological Constant and describes its impact on the dynamic of the Universe: Λ accomplishes the goal for which it was advocated, namely it counteracts the gravitational pull of other ordinary fluids modifying the Friedmann Equations as follows:

The Friedmann Equations with the Cosmological Constant

$$\frac{\dot{a}^2}{a^2} = \frac{\kappa^2}{3} \left(\rho_k + \rho_\Lambda + \sum_i \rho_i \right) , \tag{1.2.22}$$

$$\frac{\ddot{a}}{a} = -\frac{\kappa^2}{6} \left[-2\rho_\Lambda + \sum_i (\rho_i + 3p_i) \right] . \tag{1.2.23}$$

The Friedmann Equations presented in Eqs. 1.2.22, 1.2.23 have static solutions, albeit unstable, for a geometrically spherical, close Universe ($K = +1$) and for non-negative values of ρ_i, p_i and Λ.

After the discovery of the expansion of the Universe by Hubble [102], the necessity for a static solution ceased to exist, and the whole concept of a Cosmological Constant was abandoned. Rumor has it, Einstein himself called the introduction of Λ "the biggest blunder" of his scientific career [144]; while it is not of interest whether Einstein really said or wrote those words, it is worth mentioning that the introduction of Λ was probably one of the most notorious cases of confirmation bias in Cosmology: at the beginning of the 20th century it was a common belief among scientist (at least) that the Universe was static, and Einstein did want to provide a cosmological solution that could meet such a requirement. Twenty years ago our *Weltanschauung* was subverted again by a new striking evidence, and the Cosmological

Constant's odyssey took another unpredictable twist: thanks to the discovery of the present acceleration in the expansion of the Universe [154, 176], the interest in the the Λ term was renewed. Its role was to provide an (anti-)pressure stronger than the gravitational pull on the matter content of the Universe, driving the accelerating expansion of the Cosmos. We will revise these discoveries in Section 1.3.

The Cosmological Constant problem and the Coincidence problem

It is worth emphasising that the choice of Λ as dominant component opens up to an unpleasant conundrum. In fact, if we associate the Cosmological Constant to the energy vacuum density (i. e. the background energy in absence of matter), we find that the observed value of Λ is smaller by a factor $\sim 10^{120}$ than the value of the vacuum energy predicted by quantum field theory. This catastrophic discrepancy is known as *Cosmological Constant Problem*. Another enigma of the current cosmological paradigm is that we are living in a very peculiar moment of the Universe's history, namely the epoch in which the Dark Energy is taking over as dominant component of the Universe. The latter peculiar conjunction is referred to as the *Coincidence Problem*. These two long-standing difficulties are still far from being solved.

1.2.5 *The critical density and the energy density components*

The continuity equation

The Friedmann Equations can be rearranged into a single equation by differentiating Equation 1.2.22 and inserting it in Equation 1.2.23. The resulting equation represents the mass-energy conservation and it is better known as *continuity equation*, which, for a single component (with pressure p and energy density ρ), reads:

$$\dot{\rho} + 3\frac{\dot{a}}{a}(\rho + p) = 0\,. \tag{1.2.24}$$

The Hubble parameter

It is convenient to introduce the *Hubble parameter*

$$H \equiv \frac{\dot{a}}{a} \tag{1.2.25}$$

which quantifies the relative expansion rate of a homogeneous and isotropic FLRW Universe. The scale factor $a(t)$ today, i. e. at $t = t_0$ is conventionally set to unity: $a(t_0) = 1$. Substituting the Hubble parameter in the first Friedmann Equation, Equation 1.2.22, and in the continuity equation Equation 1.2.24 rewritten to include all components in the Universe, we obtain

$$H^2 + \frac{K}{a^2} = \frac{\kappa^2}{3}\left(\sum_i \rho_i + \rho_\Lambda\right)\,, \tag{1.2.26}$$

$$\sum_i \dot{\rho}_i + 3H\sum_i (\rho_i + p_i) = 0\,. \tag{1.2.27}$$

The critical density of the Universe

By considering a flat Universe ($K = 0$), Equation 1.2.26 defines the *critical density* of the Universe as:

$$\rho_c(t) = \frac{3H^2(t)}{\kappa^2}\,. \tag{1.2.28}$$

If a sphere of radius $a(t)$ is filled with matter at critical density, then the gravitational potential of the sphere is equal to its kinetic energy: this means that such a sphere contains just enough matter to *halt its expansion at infinite time*. The curvature and geometry of the Universe depend on the balance between expansion rate and the counter action of gravity (produced by ρ_m); depending on the relation between ρ_c and ρ_m we expect that:

- if $\rho_m > \rho_c$ then the Universe is closed, with positive curvature (sphere). Gravity will eventually win: the Universe will stop expanding and start collapsing on itself in a *Big Crunch*;
- if $\rho_m = \rho_c$ then the Universe is flat with zero curvature (plane surface). It will expand forever, with a decreasing expansion rate (virtually stopping at $t \to \infty$);
- if $\rho_m < \rho_c$ then the Universe is open with negative curvature (saddle surface). Expansion is fated to dominate the Universe, which will be expanding forever.

Ω_i, the dimensionless parameters of energy densities

The critical density provides a natural unit for the energy density, thus it is convenient to define dimensionless parameters of the energy density contents of the Universe by expressing them in units of the critical density, ρ_c, as follows:

$$\Omega_i(t) \equiv \frac{\rho_i(t)}{\rho_c(t)}\,, \tag{1.2.29}$$

$$\Omega_{i,0} \equiv \frac{\rho_i(t_0)}{\rho_c(t_0)} \equiv \frac{\rho_{i,0}}{\rho_{c,0}}\,, \tag{1.2.30}$$

where the subscript 0 always refers to the Universe today. Considering Equation 1.2.19, we can write down the dimensionless Cosmological Constant parameter as:

$$\Omega_\Lambda(t) \equiv \frac{\rho_\Lambda}{\rho_c} = \frac{\Lambda}{3H^2(t)}\,, \tag{1.2.31}$$

$$\Omega_{\Lambda,0} = \frac{\Lambda}{3H_0^2}\,, \tag{1.2.32}$$

and, since $\Omega_{\text{tot}} = \sum_i \Omega_i = 1$ the dimensionless parameter associated with the curvature, can be defined as:

$$\Omega_k(t) = 1 - \Omega_m(t) - \Omega_r(t) - \Omega_\Lambda(t) = -\frac{K}{H^2(t)a^2(t)}\,, \quad (1.2.33)$$

$$\Omega_{k,0} = -\frac{K}{H_0^2}\,, \quad (1.2.34)$$

or it can be simply computed using Equation 1.2.14. Using this notation it is easy to calculate explicitly solutions to the Friedmann Equations for each component of the Universe. Specifically, assuming that each component is separately conserved, the continuity Equation 1.2.27 can be integrated, giving the evolution of the energy density component with the scale factor:

$$\rho_i \propto a^{-3(1+w_i)}\,. \quad (1.2.35)$$

By combining this result with Equation 1.2.26 we furthermore obtain the evolution of the scale factor as a function of the cosmic time:

$$a(t) \propto t^{-3(1+w_i)/2}\,. \quad (1.2.36)$$

Substituting in Eqs. 1.2.35 and 1.2.36 the EoS of each component we can write down the evolution of the scale factor and of the cosmic time in a single component universe.

1.2.6 *Single component universes*

A universe of radiation only

Let us consider how the Universe would evolve in specific cases, in which only one of its component is relevant. We might begin by exploring a Universe constituted exclusively by radiation. The radiation component (typically photons) has a large pressure, which amounts to:

$$p_r = (1+\epsilon)\rho_r \frac{k_B T}{\langle E \rangle}$$

where

$$\epsilon \approx 0.05$$

for Bosons, k_B is Boltzmann's Constant, T is the temperature and $\langle E \rangle$ is the mean energy per particle, which is given by $\langle E \rangle = 3(1+\epsilon)k_B T$. By substituting this last expression of $\langle E \rangle$ in that of the pressure of relativistic fluids, we obtain:

$$p_r = \frac{\rho}{3} \Rightarrow w = \frac{1}{3}\,, \quad (1.2.37)$$

thus finally we get that the energy density of the radiation component, ρ_r, is

$$\rho_r(t) \propto \frac{1}{a^4(t)}\,, \quad (1.2.38)$$

COMPONENT	PRESSURE p	EOS w	$\rho(t)$	$a(t)$
matter	0	0	$\propto a^{-3}(t)$	$\propto t^{2/3}$
radiation	$\rho/3$	$1/3$	$\propto a^{-4}(t)$	$\propto t^{1/2}$
curvature	$-\rho/3$	$-1/3$	$\propto a^{-2}(t)$	$\propto t$
Λ	$-\rho$	-1	$\propto a^{0}(t)$	$\exp(H_\Lambda t)$

Table 1.1: Summary of the evolution of single component universes.

and consequently the evolution of the scale factor in a radiation only Universe is:

$$a_r(t) \propto t^{1/2} \tag{1.2.39}$$

Einstein – De Sitter Universe

The matter component (baryons, cold dark matter, or any other non-relativistic fluid) has a negligible pressure compared to its energy density, $p_m \ll \rho_m$. With this assumption we obtain that the energy density of the matter component is:

$$\rho_m(t) \propto \frac{1}{a^3}\,, \tag{1.2.40}$$

and that the scale factor of a single component Universe filled with matter only is given by

$$a_m(t) \propto t^{2/3} \tag{1.2.41}$$

A Λ only Universe

In a Λ dominated Universe, we obtain from the Friedmann Equations that $H(t) \equiv \dot{a}/a =$ constant. Therefore:

$$a_\Lambda = \exp(H_\Lambda t) \tag{1.2.42}$$

where H_Λ is an integration constant.

The Milne Universe

Finally, we consider a very simple (albeit non-physical) Universe, in which there is no matter, no radiation and no Cosmological Constant, i. e. an empty Universe. The Friedmann Equations in this case allow either a flat ($K = 0$), static universe or closed ($K = -1$) universe with $\dot{a} =$ constant implying $a \propto t$.

We summarize the solutions in Table 1.1.

Thanks to Eqs. 1.2.35 and 1.2.36 we can rewrite Equation 1.2.26 in a much compact manner:

$$H^2(z) = H_0^2 E^2(z)\,, \tag{1.2.43}$$

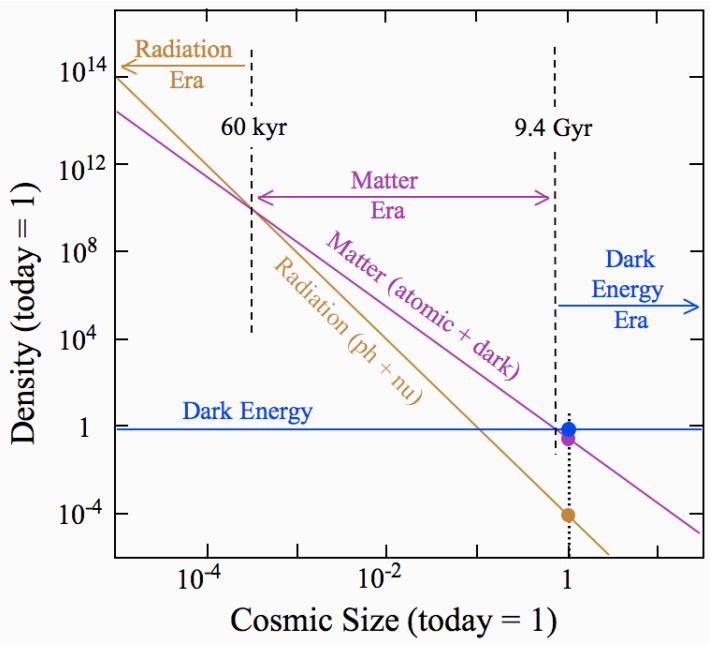

Figure 1.1: Energy density evolution of various components. Credit www.virginia.edu

where E^2 is defined as

$$E^2(z) \equiv \Omega_m(1+z)^3 + \Omega_\Lambda + \Omega_k(1+z)^2 + \Omega_r(1+z)^4 \,. \quad (1.2.44)$$

Dominant component over the history of time

Knowing how the energy density of each single component evolves as a function of the scale factor (and as a function of the Cosmic Time), we can infer which was the dominant component in the Universe during its history. Soon after decoupling the Universe entered a radiation dominated era, its expansion was following the regime $a \propto t^{1/2}$. After the time of equality between matter and radiation (i. e. $t_{eq} \,:\, \rho_r(t_{eq}) = \rho_m(t_{eq})$) the dominant component of the Universe becomes matter: the scale factor of the Universe evolves following $a \propto t^{2/3}$. In very recent time the constant value of ρ_Λ began to be significant enough to take over the dynamics of the Universe leading to its current accelerated expansion (See Figure 1.1).

1.3 OBSERVING THE UNIVERSE'S EXPANSION

So far we have discussed an overall very theoretical view of the Universe, which, as mentioned at the end of Section 1.2.4, was profoundly influenced by two observational facts: the Universe is expanding, and there is an increasing rate in this expansion. In this subsection we review such discoveries.

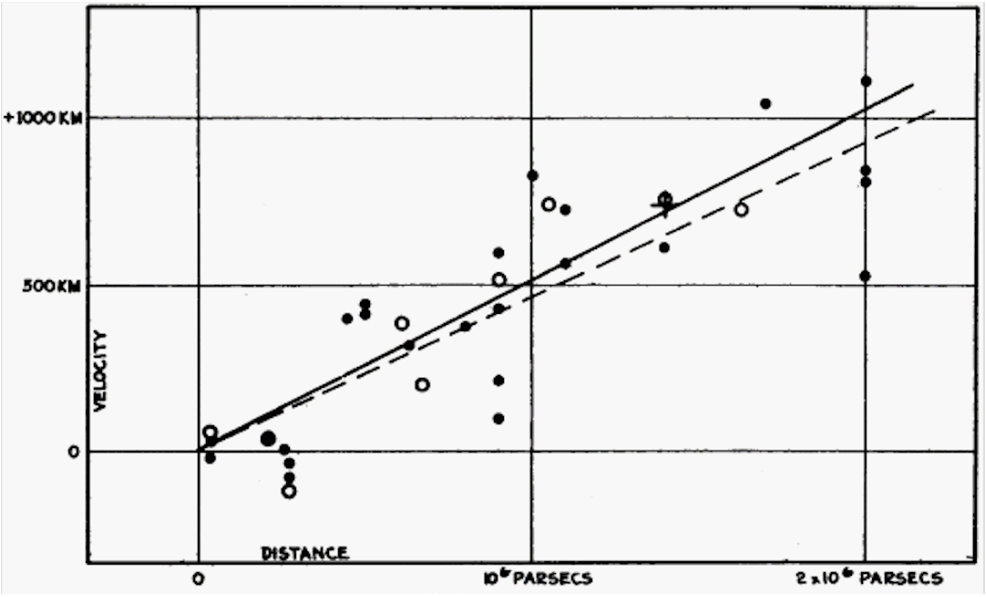

Figure 1.2: Original Hubble diagram, from the 1929 paper. It displays the velocities (in km/s, mistakenly reported in *km* in the original figure) of galaxies outside the Local Group as function of their distances (in parsec). In some cases the velocities of the galaxies (black dots) were corrected for the motion of the Sun: the best fit for these points is shown by the solid line. Circles represent galaxies for which such correction was not possible: these points are interpolated by the dashed line. The slope of the linear fit provides the value the value of H_0.

1.3.1 *The Hubble law*

In 1929 Edwin Hubble observed that the galaxies outside the Local Group were receding from the Earth with a rate proportional to their distance from it. More specifically, Hubble measured that the galaxy radial recession (v) is proportional to the distance from the observer D; hence, the *Hubble Law* reads:

$$v = H_0 D \tag{1.3.1}$$

where $H_0 \equiv H(t_0)$ is the value of the Hubble parameter (constant) today (in Hubble's paper something around $\approx 500\,h\,\mathrm{kms}^{-1}\mathrm{Mpc}^{-1}$, where h is a dimensionless number). The value of H_0 was estimated with linear regression from the *Hubble diagram*, see Figure 1.2, in which v was plotted as function of D and H_0 was inferred as the slope of the line that interpolates the points. The results presented by Edwin Hubble are inconsistent with a static Universe, but they are compatible with an expanding Universe for which H_0 is providing the scaling factor for such expansion. Many follow up observations independently confirmed this last possibility.

The discovery of the expansion of the Universe

This effect can be quantified in terms of a shift of each galaxy spectrum toward its red end, hence the definition *redshift*, z. Such shift is

associated to the linear stretch of the intrinsic wavelength (λ) of the light coming from the emitting galaxies due to the expansion of the Universe, implying that $\lambda(t) \propto a(t)$. More quantitatively, for galaxies that emit photons with wavelength $\lambda_{\rm em}$ and frequency $\nu_{\rm em}$, the observed redshift can be defined as:

$$z \equiv \frac{\lambda_{\rm obs}}{\lambda_{\rm em}} - 1 = \frac{\nu_{\rm em}}{\nu_{\rm obs}} - 1 = \frac{a(t_{\rm obs})}{a(t_{\rm em})} - 1 \tag{1.3.2}$$

where $\lambda_{\rm obs}$ and $\nu_{\rm obs}$ are the observed wavelength and frequency. If the receiver (observer) is located today ($t = t_0$), then $a(t_{\rm obs}) = a(t_0) = a_0 = 1$, we find:

$$a = \frac{1}{1+z}\,. \tag{1.3.3}$$

The more a galaxy is further away from the observer, the greater is the redshift observed on Earth.

1.3.2 *Cosmological distances*

As a consequence of the Hubble law, the Euclidean concept of distance has to be generalised in order to account for the expansion of the space-time. In a flat Universe, photons travel to us on a null geodesic, $cdt = a(t)dr$, (where in this case $dr = dl$ in Equation 1.2.9, and we have explicitly reported c). Therefore, the *comoving radial distance* can be defined as:

$$r = c\int_t^{t_0} \frac{dt'}{a(t')} = c\int_a^{a_0} \frac{da'}{a'^2 H(a')} = c\int_0^z \frac{dz'}{a_0 H(z')}\,, \tag{1.3.4}$$

where H as function of redshift is given by Equation 1.2.43.

Angular diameter distance

The *angular diameter distance* of an object, $D_{\rm A}$ is defined as its physical size, χ, over its angular size θ. In a flat universe $D_{\rm A}$ can be computed as the scale factor times the comoving radial distance:

$$D_{\rm A}(z) = a(z)r = \frac{c}{1+z}\int_0^z \frac{dz'}{H(z')}\,. \tag{1.3.5}$$

Such definition can be used to measure $H(z)$. In fact, if the comoving separation between two objects A and B (or the intrinsic size of an object) $x_{\rm AB}$ is known, then (for $z \ll 1$):

$$H(\bar{z}) = \frac{c\Delta z}{x_{\rm AB}}$$

where $H(\bar{z})$ is the Hubble parameter at redshift $\bar{z} = (z_A + z_B)/2$ (being z_A and z_B the redshift at A and B), and Δz is equal to $z_B - z_A$. Unfortunately the intrinsic size or separation of two object is commonly not known.

Another method to constrain $H(z)$ was proposed by Alcock and Paczynski [6] (also known as AP test). This method relies on the statical isotropy of the Universe and, although it does not require prior knowledge on intrinsic size or separation, it can only be performed with a population of spheres of diameter L. By measuring the redshift difference along the line of sight, Δz, we find $H(z) = c\Delta z/[L(1+z)]$. Furthermore, the angular extension of this spherical distribution, θ, is related to the the intrinsic physical size, L, via the angular diameter distance: $\theta/D_A(z)$. Therefore by measuring the angular extension, θ, and the redshift difference, Δz, and combining them, we finally obtain (for $z \ll 1$):

Alcock Paczyński test

$$D_A H(z) = \frac{c\Delta z}{\theta(1+z)}\,. \tag{1.3.6}$$

The right hand side of Equation 1.3.6 contains observables, hence the AP test allows to determine $D_A H$. A challenge for this method is to find a population of spherically symmetric objects. Recently, large empty regions of the Universe have been advocated as such population with promising results [see e.g. 127, 205, 206].

Finally, we recall the definition of *luminosity distance*, D_L, which links the bolometric observable flux F (i. e. the energy per unit of time per unit of area from the source to the observer) to the bolometric intrinsic luminosity of the source, L:

Luminosity distance

$$D_L = \sqrt{\frac{L}{4\pi F}}\,. \tag{1.3.7}$$

This implies that farther objects appear dimmer to us. Nevertheless, if the intrinsic luminosity of an object is known (i. e. we are observing a *standard candle*) we are able to infer the luminosity distance form its apparent luminosity. On top of that, in a FLRW metric, it is possible to link the luminosity distance to the angular distance with a rather simple relation. By considering that

- The energy emitted by a luminous object is diluted by the surface area $4\pi r^2 a_0^2$;
- Each emitted photon loses energy as $E \propto a/a_0 = 1/(1+z)$;
- The rate at which photons are received per unit of time is dilated by a factor $a/a_0 = 1/(1+z)$ (compared to the rate at light-emission);

we can write down the *cosmological inverse squared law* formula, that is:

$$F = \frac{L/(1+z)^2}{4\pi r^2 a_0^2}\,. \tag{1.3.8}$$

Considering the definition of luminosity distance Equation 1.3.7 and Equation 1.3.8, we conclude that the following relation applies:

$$D_{\mathrm{L}}(z) = a_0(1+z)r = (1+z)^2 D_{\mathrm{A}}(z)\,. \tag{1.3.9}$$

If Equation 1.3.9 is applied to a population of standard candles (such as Supernovae Type Ia, as we will later describe in Section 1.3.3) at known redshift, it can be used to measure $H(z)$.

1.3.3 *The accelerating expansion of the Universe*

After the discovery of the Hubble law and of the consequent expansion of the Universe, the common (and sensible) belief was that, due to the effect of gravity on matter, such expansion had to slow down. With no evidence for positive or negative curvature, the only known components were matter and radiation. The contribution of the latter was irrelevant after the time of matter-radiation equality. Therefore the model typically *in auge* from the thirties till the nineties was that of a flat, matter dominated Universe.

First evidence-based discrepancy from a matter dominated Universe

It is worth recalling that the first observational measurement displaying inconsistency with Standard Cosmological Model at that time, came from the study of the large-scale structure of the Universe in 1990. In particular the large-scale angular correlation function of galaxies in the APM Galaxy Survey [125], was not compatible with the theoretical predictions produced by a flat, matter dominated Universe. Later the same year, Efstathiou, Sutherland, and Maddox [69] displayed that such discrepancy could be removed by assuming a flat Universe in which the matter content was very low, $\approx$ 20% of the total energy density, and in which the remaining missing energy was provided by a Cosmological Constant Λ. Furthermore, in their conclusions, Efstathiou, Sutherland, and Maddox [69] solicited further investigations on these matters, such as new geometrical tests to measure the deceleration rate of the Cosmos, in order to confirm or constrain the hypothesis of a Cosmological Constant dominating the dynamic of the Universe.

The Supernovae experiment

A few years later two independent observational campaigns, *The Supernova Cosmology Project* [176] and *The High-z Supernova Search Team* [154], provided the invoked evidence. The two groups employed Supernovae Type Ia (SNIa) to study the relation between magnitude and redshift. This particular kind of Supernova is originated by a

binary system, in which one of the stars is a white dwarf (WD): as the evolution of a binary system proceeds, the companion massive star might expand touching its Roche lobes, losing mass to the WD, which undergoes an accretion fase. WD's hydrostatic equilibrium is very well understood: such a compact object does not collapse thanks to the electron degeneration pressure, which balances the strong gravitational pull exerted by the WD itself[3]. Such equilibrium can be reached only within a certain mass range, to which an upper limit is given by the Chandrasekhar mass ($\approx 1.36 M_\odot$). As soon as the accretion breaks this mass limit, the WD explodes in a SNIa: the advantage for cosmological purposes is that, knowing the mass of the progenitor, it is possible to characterize with extremely high accuracy the intrinsic magnitude of such supernovae explosions (i. e. SNIa are standard candles).

SNIa as standard candles

The SNIa magnitude evolution with redshift is incompatible with a decelerating Universe: in fact, both groups found evidence for negative values of the deceleration parameter today, q_0, defined as

$$q_0 \equiv -\frac{\ddot{a}_0 a_0}{\dot{a}_0^2} = -\frac{\dot{H}_0 + H_0^2}{H_0^2} \,. \tag{1.3.10}$$

Fluids fulfilling the strong energy condition - presented in Equation 1.2.7 - cannot account for positive values of $\ddot{a}$: therefore, the evidence for negative values of q_0 reported by Riess et al. [176] and Perlmutter et al. [154] suggests the presence in the Universe of a unknown component that violates Equation 1.2.7 and factually drives such acceleration in the expansion. The simplest fluid meeting these requirements is Λ. Many other probes in last 20 years confirmed the accelerated expansion, and, so far, there is no particular evidence for ruling out an elementary Cosmological Constant as late time dominant component.

3 WDs are objects with sizes similar to that of the Earth but with typical masses around one solar mass, $M_\odot$.

2

THE LARGE SCALE STRUCTURE OF THE UNIVERSE

In Chapter 1 we have clarified how the Universe behaves as a whole, by assuming the Cosmos to be homogeneous and isotropic. However, the skies are populated with a plethora of structures: stars are usually embed in globular clusters or in galaxies, galaxies are distributed over the *Cosmic Web* of the Universe, in filaments or clumped together in cluster of galaxies, leaving some other regions mostly under-dense or empty. We shall revise how this large variety of structures materialized.

This Chapter is entirely devoted to the summary of the processes that led to the formation of structure in the Cosmos. We will review how, starting from small fluctuations in the energy density content of the Universe, over-densities grew by means of a gravitational collapse and under-densities expanded to form large and almost empty regions. The treatment of these subjects is mostly based on the following books, notes and reviews (including references therein): Coles and Lucchin [54] (Chapter 10), Mana [126] (Chapter 1), Tormen [216] (Chapters 1-5), Weller [218] (Chapters 4, 5), Komatsu [109] (Chapters 3), Hamaus [91] (Chapter 1-3), Zentner [223].

Let's start back where we left after the discovery of the Hubble law in Section 1.3.1. If the Universe is expanding, it is reasonable to assume that in the past the Cosmos was smaller, denser and hotter than now. The early Universe was in fact so hot and dense that ordinary matter was ionised and radiations tightly coupled to electrons via Thomson scattering. As the expansion of the Universe proceeded, when the Universe was roughly 380000 year old ($z \approx 1100$), (its temperature $\approx$ 3000 K) was small enough to finally allow protons and electrons to form hydrogen, the Cosmos to become optically thin, and photons to free stream across the Universe. These photons can be observed today as a relic of the decoupling process, better known as Cosmic Microwave Background (CMB). The discovery of the CMB radiation is perhaps one of the best known examples of serendipity in science: in 1964 two radio-astronomers, Penzias and Wilson [153], while calibrating their antenna, accidentally found a background noise coming from every direction of the sky. The excess of temperature detected by their instrument was "isotropic, unpolarised and free from seasonal variations" [153]. The origin of the noise discovered by Penzias and Wilson [153] was cosmic microwave background itself, as speculated soon after its detection. The discovery of the CMB is fully predicted by *The big bang theory*, which pro-

"...And there was light"

The CMB as proof of a Hot Big Bang

poses that our Cosmos was originated by a singularity with infinite density and temperature, in which all forces were unified. In such picture the coupling between electrons and photons occurs naturally in the early Universe. When the recombination process is finally over, it is expected to leave a relic at the last scattering surface. The existence cosmic microwave background radiation is still considered one of most important successes of the big bang theory.

The CMB appears to us as an isotropic radiation filling the whole Universe, a thermal bath of photons, with a characteristic black body spectrum at the temperature of $T_{\rm CMB} = 2.73$K. It is of vital importance that the CMB radiation has very small fluctuations in its temperature, that, under adiabatic conditions, produce also density perturbations:

$$\frac{\Delta T}{T} = \frac{\Delta \rho_m}{\rho_m} \approx 10^{-5}\,. \tag{2.0.1}$$

The general idea is that thanks to these small fluctuations in the initial conditions, we now see the structures that form the cosmic web.

The discovery of such primordial anisotropies was made by the COsmic microwave Background Explorer (COBE) in 1992 [195]. The CMB is today one of the most important cosmological probes, extensively studied by 2 major missions in recent years [110, 159, WMAP, Planck], that exploited its cosmological potential: the constraints provided by the study of the CMB are currently the ones with highest precision. However, the CMB also represents the very end (or beginning) of the observational Universe: currently we cannot look at anything that happened before $z \approx 1100$.

On the inflationary expansion of the very early universe

Hence, we can try to infer stages occurring earlier than CMB time only with theoretical speculation. It is possible and plausible that the Universe underwent a phase of inflationary expansion before CMB time, which would explain a number of things: why the whole Universe was causally connected at $z \approx 1100$ (as shown by the uniform temperature of the CDM), why the Universe is flat, why the magnetic monopoles cannot be observed. Moreover, some predictions made by the inflation theory were successful (small Gaussian fluctuations of the CMB, spectral index n_s close to unity but smaller than 1). Nevertheless, the details of such theory pose a lot of questions that can not be easily addressed, such as what drove that expansion and how and why did it start. The CMB could provide a further test to inflactionary theories: if an exponential growth of the universe occurred at very early stage, it should be possible to find an imprinting of the gravitational waves produced by it in the polarization of the cosmic microwave background. Such measurement is possible, but complicated by dust contamination in the foreground.

2.1 STRUCTURE FORMATION: LINEAR THEORY

Provided that small fluctuations of the density field did exist at early times, we should now understand under which condition they collapsed. In a static, homogeneous and isotropic fluid, small perturbations in density and velocity will generally evolve as follows: if pressure is negligible, an over-dense region - attracting the surrounding material - tends to become denser and denser, eventually collapsing into a gravitationally bound system. The threshold in the length scale that a fluid (with mean density ρ) should exceed to experience such collapse is given by the *Jeans lenght* of a fluid:

The Jeans lenght

$$\lambda_{\rm J} = c_s \sqrt{\frac{\pi}{G\rho}}\,, \tag{2.1.1}$$

where c_s is the speed of sound.

There are different ways to qualitatively understand why $\lambda_{\rm J}$ has this form: the easiest is probably provided by the comparison of the free fall time $\tau_{\rm ff} \propto 1/\sqrt{G\rho}$ (i. e. the typical time that a fluctuation needs to collapse under its own gravity) with the hydrodynamical time $\tau_{\rm h} \propto \lambda/c_s$ (i. e. the typical time needed by the perturbation to adjust its pressure and density variations) of the fluid. By imposing $\tau_{\rm ff} = \tau_{\rm h}$ we can estimate that $\lambda \approx \lambda_{\rm J}$, and we obtain that $\lambda_{\rm J} \propto c_s/\sqrt{G\rho}$ as more precisely displayed in Equation 2.1.1. If $\lambda > \lambda_{\rm J}$, then the fluctuation will grow. Otherwise (if $\lambda < \lambda_{\rm J}$) fluctuations will oscillate as acoustic waves. To study the collapse of cosmological objects this simple theory is generally employed, although further complications (expanding background, average density evolving with time, horizon scales) must be included.

The first over-densities to form were those of dark matter: in fact, before decoupling, the radiation pressure was preventing the collapse of the fluctuation in the radiation component (which was dominant in the early Universe), and baryonic matter, being coupled to radiation, could not collapse as well. The interplay between gravitation and radiation pressure produced oscillations in the baryon-photon plasma, known as *Baryonic Acoustic Oscillations* (BAO). Cold Dark Matter inhomogeneities, on the other hand, were able to start to condensate and grow earlier, as radiation pressure did not impede them to do so.

After recombination, when the baryons fully decoupled from radiation, the first local over-densities of ordinary matter could finally form, but, at that stage, dark matter was already providing some potential wells in which baryons could collapse, forming structure much faster. In a Universe with baryonic matter only, structures would form at a much later time than we observe, or, in other words, the existence of CDM boosted structure formation.

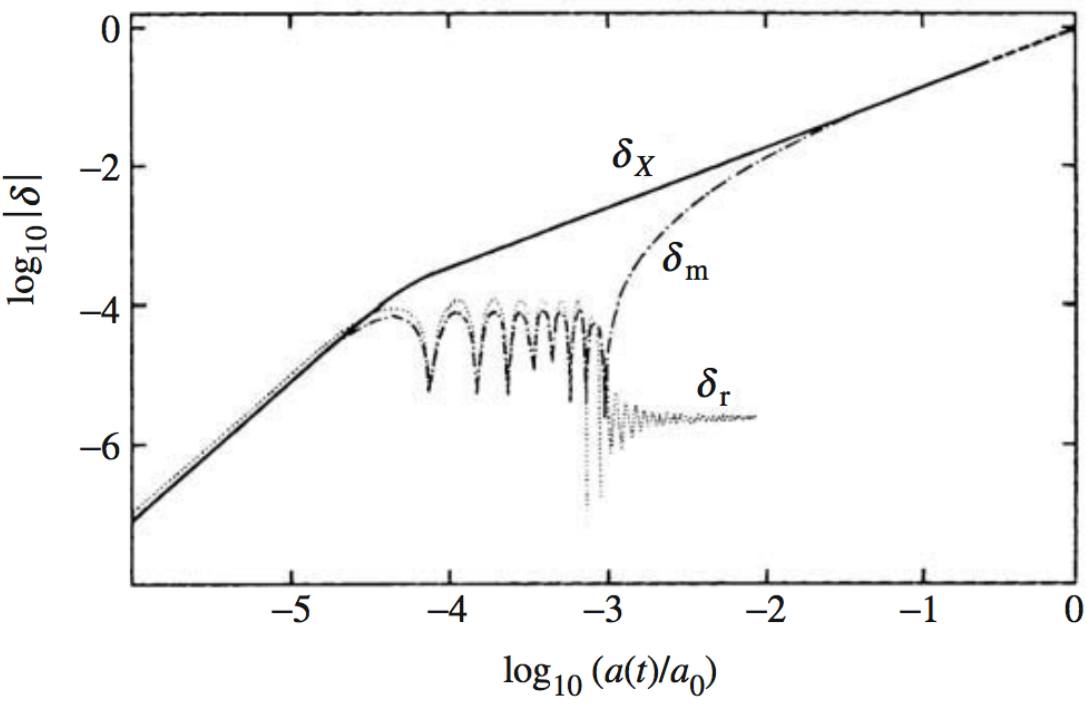

Figure 2.1: Evolution of perturbations, corresponding to a mass-scale of $10^{15} M_\odot$, for the cold component δ_x, the baryonic component δ_m and radiation component δ_n. Credit: Coles and Lucchin [54]

Although after recombination it is possible to treat the evolution of matter over-densities with the same physical description, regardless if baryons or dark matter are under study, the power spectrum of fluctuations in baryonic matter or in dark matter are quite different: BAO dominate the power spectrum of baryonic fluctuations at early time, while such signature is almost negligible in the dark matter power spectrum. In Figure 2.1 it is shown how the evolution of density perturbation in dark matter δ_x is not significantly altered by the other components, while δ_m and δ_r are oscillating before decoupling. After that, δ_m rapidly catches up with the dark matter evolution.

2.1.1 *Jeans instability*

The density contrast

In order to understand more generally how λ_J was derived by Jeans, we must follow the evolution of a inhomogeneity of a fluid with mean density $\bar{\rho}(t)$; it is convenient to define its *density contrast* as

$$\delta(\vec{x}, t) = \frac{\rho(\vec{x}, t) - \bar{\rho}(t)}{\bar{\rho}(t)} . \tag{2.1.2}$$

In order to simplify the study of the evolution of density fluctuations, we make the following assumptions:

- dark matter and baryons evolve together, i. e. we treat them as a single fluid;
- the fluctuations collapse only gravitationally;
- the process is adiabatic;
- the fluctuations are small ($\delta \ll 1$), which allows us to treat them linearly (considering only first order terms in δ) and to ignore general relativistic effects (i. e. we can treat gravity in a Newtonian fashion);
- the fluctuations arise in an ordinary perfect fluid (that we fully know how to treat).

To analyse the evolution of a Newtonian perfect fluid with density $\rho = \rho(\vec{x}, t)$, flow velocity $u = u(\vec{x}, t)$, we generally need five equations, that link the five field (density ρ, velocity $\vec{u}$, pressure p, entropy S and gravity Φ) of the fluid as follows:

The five Equations that describe a Newtonian perfect fluid

- the Continuity Equation expressing mass conservation

$$\frac{\partial \rho}{\partial t} + \vec{\nabla} \cdot (\rho \vec{u}) = 0\,; \tag{2.1.3}$$

- the Euler Equation, signifying the momentum conservation

$$\frac{\partial \vec{u}}{\partial t} + (\vec{u} \cdot \vec{\nabla})\vec{u} = -\frac{1}{\rho}\vec{\nabla} p - \vec{\nabla}\Phi\,; \tag{2.1.4}$$

- the Poisson equation, that links the gravitational field to its source

$$\nabla^2 \Phi = 4\pi G \rho\,; \tag{2.1.5}$$

- An equation that describes the evolution in time of the entropy, S, which, assuming the adiabatic condition is simply

$$\frac{dS}{dt} = 0\,; \tag{2.1.6}$$

- Finally we need and Equation of State, that - since $S =$ constant, does not depend on the entropy - simply relates pressure and density

$$p = p(\rho)\,. \tag{2.1.7}$$

Static solution

A static solution to this set of equation is given by[1]:

1 Please note that such set of solutions is formally inconsistent, as a constant gravitational potential it is not allowed by the Poisson Equation unless $\rho = 0$. Anyway this simplified treatment still allows to find reasonable solutions in case of small perturbations.

$$\begin{cases} \rho & = \text{constant} \equiv \rho_0 \\ p & = \text{constant} \equiv p_0 \\ \vec{u} & = 0 \\ \Phi & = \text{constant} = \Phi_0 \end{cases}, \tag{2.1.8}$$

plus the obvious $S = \text{constant}$ that from now on we are going to ignore. The static solution presented in Equation 2.1.8 can be perturbed by adding small fluctuation to it, as follows:

$$\begin{cases} \rho & = \rho_0 + \delta\rho \\ p & = p_0 + \delta p \\ \vec{u} & = \delta\vec{u} \\ \Phi & = \Phi_0 + \delta\Phi \end{cases}. \tag{2.1.9}$$

By inserting the perturbed equations (Equation 2.1.9) into the system of equations provided by the continuity equation, the Euler's equation and Poissons equation, neglecting terms with order higher than linear, we obtain the following system of equations:

$$\begin{cases} \dfrac{\partial\delta\rho}{\partial t} + \rho_0 \vec{\bigtriangledown}\delta\vec{u} = 0 \\ \dfrac{\partial\delta\vec{u}}{\partial\delta t} = -\dfrac{c_s^2}{\rho_0}\vec{\bigtriangledown}\delta\rho - \vec{\bigtriangledown}\delta\Phi \\ \bigtriangledown^2\delta\Phi = 4\pi G\delta\rho \end{cases} \tag{2.1.10}$$

which can be recast into a single differential equation: Wave equation

$$\ddot{\delta\rho} - c_s^2 \bigtriangledown^2 (\delta\rho) = 4\pi G\rho_0(\delta\rho)\,. \tag{2.1.11}$$

Equation 2.1.11 is a wave equation with solution:

$$\delta\rho(\vec{x},t) \propto \delta(\vec{x},t)\exp(-i\vec{k}\cdot\vec{x} + i\omega t)\,, \tag{2.1.12}$$

where ω and $\vec{k}$ satisfy the dispersion relation:

$$\omega^2 = c_s^2 k^2 - 4\pi G\rho_0\,, \tag{2.1.13}$$

with $k = |k|$. By imposing this equation to be zero, we obtain the *Jeans wave number*

$$k_\mathrm{J} = \sqrt{4\pi G\rho_0/c_s} = 2\pi/\lambda_\mathrm{J}\,,$$

from which Equation 2.1.1 can be derived. If ω is imaginary, the perturbations will oscillate as sound waves, while, if ω is real, we will have exponentially growing and decaying modes.

2.1.2 *Gravitational instability in an expanding Universe*

The treatment we presented in the previous Section, Section 2.1.1, has to be adapted to an expanding Universe. This means we shall link the evolution of small fluctuations with the scale factor. Furthermore the Jeans length should be computed under different regimes and for various typical scales: the relevant epochs in this framework are separated by the equality time $t_{\rm eq}$ and the recombination time $t_{\rm rec}$, while, besides $\lambda_{\rm J}$, important scales to consider in this context are the dissipation scale $\lambda_{\rm D}$ (below which the acoustic waves are cancelled by micro-physics processes), and the horizon scale

$$R_{\rm H} = a(t) \int_0^{t'} \frac{cdt}{a(t)} ,$$

outside of which there is no causal connection. Before introducing how the Jeans length may be computed in all of these cases, it is useful to present a very qualitative but rather general solution (which will be presented following the notes by Tormen [216]). If we consider an over-dense fluctuation as a closed locally over-dense universe (to which we refer to with the suffix loc) immersed in a flat, matter only Universe, then the two Friedmann equations to consider in order to describe this system are:

A simple and yet general perspective

$$\begin{cases} H^2 = \dfrac{\kappa^2 \rho}{3} , & K = 0 \\ H_{\rm loc}^2 = \dfrac{\kappa^2 \rho_{\rm loc}}{3} - a^{-2} , & K = 1 \end{cases} . \tag{2.1.14}$$

If we decide to study the behaviour of such fluctuation at $t = t'$: $H(t') = H_{\rm loc}(t')$, we obtain

$$\frac{\kappa^2 \rho_{\rm loc}}{3} - a^{-2} = \frac{\kappa^2 \rho}{3} ,$$

from which, by defining $\delta = (\rho_{\rm loc} - \rho)/\rho$, we can write:

$$\delta(t) = \frac{3}{\kappa^2 \rho a^2} , \delta \propto a^{-2} \rho^{-1} \tag{2.1.15}$$

which is valid if $\delta \ll 1$. Remembering Equation 1.2.35, we finally get

$$\delta(t) \propto a^{3(1+w)-2} = a^{1+3w} .$$

For scales $\lambda > R_H$, as no causal connection is possible, gravity is the only interaction in place therefore all components follow the dominant component. Thus, we conclude that, before equality:

$$\begin{aligned} t < t_{\rm eq},\ \lambda > R_H \Rightarrow \rho \approx \rho_{\rm rad} \Rightarrow w = 1/3 \Rightarrow & \delta \approx \delta_{\rm rad} \propto a^2 \propto t \\ & \delta_{\rm bar} \propto \delta_{\rm rad} \\ & \delta_{\rm m} \propto \delta_{\rm rad} \end{aligned}$$

and, after equality:

$$t > t_{\rm eq},\ \lambda > R_H \Rightarrow \rho \approx \rho_{\rm m} \Rightarrow w = 0 \Rightarrow \delta \approx \delta_{\rm m} \propto a \propto t^{2/3}\,. \qquad \delta_{\rm m} \propto \delta_{\rm m} \qquad \delta_{\rm bar} \propto \delta_{\rm m}$$

These qualitative solutions might also be valid for scales $\lambda_{\rm J} \gg \lambda < R_H$, but, in general, for scales $\lambda < R_H$, perturbations in the non-dominant components behave differently, as other interactions have to be considered.

A perturbed static solution in the expanding Universe

To determine more quantitatively the evolution of small fluctuations at all scales and time in an expanding Universe, we shall include the expansion in the system of equations including Poisson's, Euler's and Continuity Equation. In this case it also convenient to use comoving coordinates i. e. $\vec{x}_{\rm com} = \vec{x} = a\vec{x}_{\rm phys}$. The velocity of the fluid, that can be obtain by taking the derivative with respect to time of $\vec{x}$. This is $\vec{u} = H\vec{x} + \vec{u}_{\rm int}$, i. e. is given by an intrinsic velocity $\vec{u}_{\rm int}$ term and by the expansion of the Universe. Using this notation the system of equations we should solve reads as follow:

$$\begin{cases} \dfrac{\partial \rho}{\partial t} + \vec{\bigtriangledown} \cdot (\rho \vec{u}) = 0 \\ \dfrac{\partial \vec{u}}{\partial t} + (\vec{u} \cdot \vec{\bigtriangledown})\vec{u} = -\dfrac{1}{\rho}\vec{\bigtriangledown} p - \vec{\bigtriangledown}\Phi \\ \bigtriangledown^2 \Phi = 4\pi G \rho \end{cases} . \tag{2.1.16}$$

A perturbation of a static solution to the system of Eqs. 2.1.16 is given by:

$$\begin{cases} \rho = \rho_0 (1 + \delta) \\ \vec{u} = H\vec{x} + \vec{v} \\ p = p_0 + \delta p \\ \Phi = \Phi_0 + \phi \end{cases} . \tag{2.1.17}$$

Substituting these perturbed solutions in the system of Eqs. 2.1.16, and selecting only the linear terms, the system to be solved reads:

$$\begin{cases} \dfrac{\partial \delta\rho}{\partial t} + \dfrac{\rho_0}{a}\vec{\bigtriangledown}\vec{u}_{\rm int} + 3H\delta\rho = 0 \\ \dfrac{\partial \vec{v}}{\partial t} + H\vec{v} = -\dfrac{c_s^2}{a}\vec{\bigtriangledown}\delta - \dfrac{1}{a}\vec{\bigtriangledown}\phi \\ \dfrac{1}{a^2}\bigtriangledown^2 \phi = 4\pi G \rho_0 \delta \end{cases} . \tag{2.1.18}$$

To solve system of Eqs. 2.1.18 we move to Fourier space, and we recast the system into a single differential equation. In this case, the system depends on the scale factor and on its first derivative over time:

$$\ddot{\delta}_k + 2\frac{\ddot{a}}{a}\dot{\delta}_k + \delta_k\left(\frac{k^2c_s^2}{a^2} - 4\pi G\rho_0\right) = 0\,. \tag{2.1.19}$$

Equation 2.1.19 is a damped wave equation. If we neglect the expansion term and identify $|k|/a$ as the physical wave number, with $\vec{k}$ being the the *comoving wavenumber*, we recover the wave equation we formerly obtained in a static Universe. Similarly to what we have seen in the previous , the Jeans wave number

$$k_J^2 \equiv \frac{4\pi G\rho_0 a^2}{c_s^2} \tag{2.1.20}$$

separates the stable modes from the gravitationally unstable ones.

If we assume that the Universe is flat ($K = 0$) and matter dominated, with

$$\frac{\dot{a}}{a} = \frac{2}{3}t^{-1}\,, \text{ and } \rho_0 = (6\pi G t^2)$$

we obtain

$$\ddot{\delta} + \frac{4}{3t}\dot{\delta} - \frac{2}{3t^2}\delta = 0\,,$$

where, as already motivated earlier, the pressure term was neglected being not relevant in a matter dominated Universe ($c_s^2k^2/a^2 \ll 4\pi G\rho_0$). This last equation has two independent solutions, a growing mode, δ_+, and a decaying mode, δ_-, that, by choosing a time t_i conveniently for normalization purposes, can be written as follows:

$$\delta_+(t) = \delta_+(t_i)\left(\frac{t}{t_i}\right)^{2/3}\,, \tag{2.1.21}$$

and

$$\delta_-(t) = \delta_-(t_i)\left(\frac{t}{t_i}\right)^{-1}\,. \tag{2.1.22}$$

The effect of expansion on EdS Universe

From Eqs. 2.1.21 and 2.1.22 we see the effect of the background expansion of the Universe: it slows down the otherwise exponential growth of the perturbation, resulting in a power law growth of the unstable modes. Generally speaking, Equation 2.1.19 has to be solved in all specific conditions occur at various scales and epochs of interest to determine how the growing modes behave.

2.2 NON-LINEAR THEORY

In the previous Section we have recapped under which condition the collapse can happen and what is the impact of the expansion

of the Universe on it. We saw that gravitational instability produces growing and decaying modes, whose evolution should be followed to further investigate the formation of the large scale structure of the Universe.

During the matter dominated era (or, analogously, in a Einstein-De Sitter Universe), the linear density fluctuation, δ, grows as $\delta \propto a$, as depicted in previous . The linear treatment, though, break down quite fast: it is valid only for $\delta \ll 1$ hence it cannot be used to follow the evolution of non-linear density fluctuations that will eventually grow from the initially small fluctuations. Specifically, when $\delta \gg 1$, density fluctuations collapse into gravitationally bound objects i. e. a *haloes*, where galaxies that we observe in the sky are hosted.

Since the total matter must be conserved, the fact that some regions have $\delta \gg 1$ implies that other regions have $\delta < 0$. We have a limit to how under-dense these region can be in terms of density contrast, as the minimum value of $\delta \equiv \rho/\overline{\rho} - 1$ is -1 indeed. Such empty regions, or nearly so, are called *voids*. In the followings we will summarize what are the key results coming from non-linear theory evolution of over-dense and under-dense fluctuations.

2.2.1 *Spherical collapse of dark matter halos*

Following the non-linear regime of structure formation is rather complicated. Its precise treatment is very hard, and usually N-body simulations are the most appropriate instrument to study the formation and evolution of haloes. We will describe some of these simulations in the second part of this thesis (see e. g.Section 3.2.2).

Despite that, it is useful to work out a simplified case known as *spherical collapse* for a gravitationally bound objects. Consider a spherical region of mass M and radius r. Due to the expansion of the Universe, initially $\dot{r} > 0$. As the mass enclosed within r must be conserved, $\dot{M} = 0$ holds. During the matter dominated era, the equation of motion is given by Newton's law,

$$\ddot{r} = -\frac{GM}{r}\,; \tag{2.2.1}$$

after multiplying both sides by $\dot{r}$ and integrating them, we obtain that the kinetic energy and the potential energy:

$$\frac{1}{2}\dot{r}^2 - \frac{GM}{r} = E\,, \tag{2.2.2}$$

sum up to E, which is an integration constant. Since we would like to evaluate the case in which the expansion of this region eventually stops, *turns around*, and collapses, we shall consider the case in which $E < 0$. In this particular case the solution to Equation 2.2.2 is known

The turn around

as the *cycloid*, and it is given by

$$\begin{cases} r = A(1-\cos\theta) \\ t = B(\theta - \sin\theta) \\ A^3 = GMB^2 \end{cases}, \tag{2.2.3}$$

where A and B are constants, and the zero point of time was chosen such as $t \to 0$ as $\theta \to 0$. The evolution of matter density within this region is expressed as a function of a new parameter θ as:

$$\rho = \frac{M}{\frac{4\pi}{3}r^3} = \frac{3}{4\pi GB^2(1-cos\theta)^3}. \tag{2.2.4}$$

Spherical collapse in the matter dominated era

To understand how the mean density $\overline{\rho}$ depends on θ, we recall that the Friedmann equation during the matter dominated era reads

$$H^2 = \frac{8\pi G}{3}\overline{\rho} = \frac{4}{9}\frac{1}{t^2}, \tag{2.2.5}$$

therefore:

$$\overline{\rho} = \frac{1}{6\pi Gt^2} = \frac{1}{6\pi GB^2(\theta-\sin\theta)^2}. \tag{2.2.6}$$

By considering the ratio between ρ (Equation 2.2.4) and $\overline{\rho}$ (Equation 2.2.6), we obtain the following result

$$\delta = \frac{9}{2}\frac{(\theta-\sin\theta)^2}{(1-cos\theta)^3} - 1. \tag{2.2.7}$$

A sanity check for small fluctuations

The collapse time corresponds to $\theta = 2\pi$, at which δ approaches infinity. In practice this is an artefact of the spherical symmetry: a finite angular momentum makes it impossible for particles to fall straight down to the centre $r = 0$, forming an object with finite size. If we consider an early time limit to this treatment, then $\theta \ll 1$, and

$$\delta \approx \frac{3}{20}\theta, \ (\theta \ll 1). \tag{2.2.8}$$

As δ in Equation 2.2.8 is also $\ll 1$, we should be able to recover the linear limit ($\delta \propto a \propto t^{2/3}$), and, if fact, looking at the second equation of the cycloid, we get that $t \propto \theta^3$ for small θ, and thus $\delta \propto t^{2/3} \propto \theta^2$.

The time at which the density fluctuation collapses ($\theta = 2\pi; \delta \to \infty$) is given by

$$t_c = 2\pi B\,. \tag{2.2.9}$$

To summarise, following the non-linear spherical collapse, we find that at $t = t_c$, the overdensity becomes a bound halo $\delta \to \infty$. It is interesting to determine which value would δ have in the linear treatment at the same time. Using $\delta \approx (3/20)\theta^2$ and $t \approx (B/6)\theta^3$ (for $\theta \ll 1$), the linear evolution is given by

A linear threshold to the non-linear collapse

$$\delta_L = \frac{3}{20}\left(\frac{6}{B}\right)^{2/3} t^{2/3}\,, \tag{2.2.10}$$

and, finally, by inserting Equation 2.2.10 in the expression for the collapse time Equation 2.2.9, we derive

$$\delta_c \equiv \delta_L(t_c) = \frac{3(12\pi)^{2/3}}{20} \approx 1.686\,. \tag{2.2.11}$$

This last result is quite interesting because it allows us to link the non-linear evolution of the density fluctuations, which is remarkably difficult to model, to the linear evolution, which is known. If we start evolving small fluctuations, we know that some of them will collapse, and some other will not. But, more specifically, some density *peaks* collapse, which, in the real world have a very high density ($\to \infty$). In the corresponding linear world, though, this collapsed regions have $\delta_L(\vec{x}) > \delta_c \approx 1.686$. This simple property will be of help in the calculation of the number of collapsed object at a given time.

2.2.2 *Shell-crossing of empty regions*

In analogy to what we saw in Section 2.2.1, we shall find a way to link the non-linear theory of void expansion to its linear model. Underdensities never reach a turn-around time, and they keep expanding forever unless they encounter an over-density at larger scales that embeds them (void-in-cloud scenario). Furthermore, their density has a lower limit, as there is nothing less dense than empty.

A possible way to determine the moment in which non-linearity kicks in during void evolution is constituted by the so-called *shell-crossing*: two adjacent shells of different initial radius start crossing each other, leading to the formation of a void and of its ridge. The shell-crossing condition depends on the initial slope of the underdensity. In the simplest case this could be an inverted top-hat. Following such evolution we find that the typical density contrast of a shell crossing region is [191]

Voids as shell-crossing regions

$$\delta_{0,\mathrm{sc}} \backsimeq -0.795 \tag{2.2.12}$$

and compared to its initial size, the comoving void radius has expanded of a factor 1.697. Also in this case, we may compute the linear approximation for the average density contrast, using an approach analogous to that reviewed for the halo-case. The corresponding density contrast inside a top-hat is known as the linear density threshold for void-formation

$$\delta_{\mathrm{v}} \equiv -2.717\,, \tag{2.2.13}$$

which, due to linear extrapolation, amounts to an non-physical negative density. Nevertheless, also in this case, such quantity will be important to predict the number of voids that we expect to see in data.

The derivation of Equation 2.2.13 relies on the assumption of an inverted top-hat, which is not representative of a realistic initial underdensity. It is possible to demonstrate numerically that - in a Gaussian random field - density profiles around minima evolve similarly, and evolve in a top-hat like configuration by the time of shell crossing [20, 191]. Despite the similarities, the final density contrast becomes more negative in the centre and the void radius grows slightly less in a more realistic case [191].

Bernardeau [22] provides a useful relation to link linear and non-linear densities inside voids

$$\delta_{\mathrm{v}} = C[1 - (1 + \delta_{0,\mathrm{sc}})^{(-1/C)}]\,, \tag{2.2.14}$$

where C is a constant with value ≈ 1.594. Equation 2.2.14 will be helpful to relax some of the hypothesis we made so far in the context of evaluating the abundances of voids.

2.3 STATISTICAL PROPERTIES OF THE LARGE-SCALE STRUCTURE

To study the statistical properties of the Large Scale Structure it is convenient to introduce some definitions and revise some seminal work that pioneer these studies. In this Section we particularly make use of Hamaus [91], Zentner [223] and references therein.

Correlation function and power spectrum We consider fluctuation in the density field $\rho(\vec{x})$ described by the density contrast $\delta(\vec{x})$. As previously depicted, the Universe is endowed with primordial density fluctuations, with the primordial density contrast being a statistically homogeneous and isotropic Gaussian random field.

The homogeneity condition requires that both the mean of the distribution, $\langle \delta(\vec{x}) \rangle$, and the two point correlation function,

$$\langle \delta(\vec{x_1}) \delta(\vec{x_2}) \rangle \equiv \xi(\vec{x_1}, \vec{x_2}) \,,$$

to be translation invariant: this implies the two-point function to be a function of the separation vector between points, i. e.

$$\xi(\vec{x_1}, \vec{x_2}) = \xi(\vec{x_1} - \vec{x_2}) \,.$$

The correlation function is translation and rotation invariant

Furthermore, the assumption of isotropy requires the two-point correlation function to be invariant under rotation. Hence, $\xi(\vec{x})$ is only a function of the distance between the two points, i. e.:

$$\langle \delta(\vec{x_1}) \delta(x_2) \rangle \equiv \xi(\vec{x_1}, \vec{x_2}) = \xi(|\vec{x_1} - \vec{x_2}|) = \xi(r) \,, \tag{2.3.1}$$

where $r \equiv |\vec{x_1} - \vec{x_2}|$. By definition, the Fourier transform of the density contrast is given by

$$\delta(\vec{k}) = \int d^3x \, \delta(\vec{x}) e^{i\vec{k}\cdot\vec{x}} \,, \tag{2.3.2}$$

with the inverse transform being

$$\delta(\vec{x}) = \frac{1}{(2\pi)^3} \int d^3k \, \delta(\vec{k}) e^{-i\vec{k}\vec{x}} \,. \tag{2.3.3}$$

It is possible to compute the correlation function in terms of Fourier coefficients, averaging over the whole space. As we argued at the beginning of this Section, the two point function depends only on the amplitude of $\vec{r}$ due to the cosmological principle. Thereby, employing the latest equation we can re-write the correlation function as follows:

$$\xi(r) = \frac{1}{2\pi^2} \int k^3 V^{-1} |\delta(k)|^2 \frac{\sin(kr)}{kr} \, d\log k \,. \tag{2.3.4}$$

The correlation function is the Fourier transform of the power spectrum:

$$P(k) \equiv V^{-1} \langle |\delta(k)|^2 \rangle \,, \tag{2.3.5}$$

where the average is over an ensemble of universes with the same statistical properties. The correlation function $\langle \delta^2(\vec{x}) \rangle$ is therefore simply the variance of the field.

The power spectrum has the dimension of a volume, but it is convenient to define its dimensionless form, *the Dimensionless Power Spectrum* which is more easily lent to direct interpretation

$$\Delta^2(k) \equiv k^3 P(k)/2\pi^2 \,. \tag{2.3.6}$$

Typically, $\Delta^2(k)$ increases with wave-number (until some exceedingly small scales), but, in practice, we observe the density field smoothed with some finite resolution, due to observational or computational limits. Hence, we are interest in defining the density field smoothed on a particular scale R_W,

$$\delta(\vec{x}, R_W) \equiv \int d^3\vec{x}' W(|\vec{x}' - \vec{x}|;\, R_W)\delta(\vec{x}') \,, \tag{2.3.7}$$

The window function

where the function $W(x; R_W)$ is the window function that filters the density field in the desired manner. One of the most commonly employed window functions is the real-space top-hat filter

$$W(x; R_W) = \begin{cases} \text{const}\,, \; |\mathrm{x}| \leq \mathrm{R_w} \\ 0\,, \; \text{elsewhere} \end{cases} \,, \tag{2.3.8}$$

which has the following Fourier transform

$$W(k; R_W) = \frac{3[\sin(kR_W) - kR_W \cos(kR_W)]}{(kR_W)^3} \,. \tag{2.3.9}$$

The density field of fluctuations is assumed to be a Gaussian random variable. Therefore, the smoothed density fluctuation field $\delta(\vec{x}; R)$ is also a Gaussian random variable, as it stands for a sum of Gaussian random variables. The variance of $\delta(\vec{x}, R)$ hence amounts to:

The variance

$$\sigma_R^2 = \langle \delta^2(\vec{x}; R) \rangle = \int d \log k \, \Delta^2(k) |W(k; R)|^2 \,. \tag{2.3.10}$$

If we consider, for example, a power spectrum $P(k) \propto k^n$ and a Fourier space top-hat filter, we get

$$\sigma_R^2 \propto \int_0^\infty P(k) W_R^2(k; R) k^2 dk \propto \int_0^{1/R} k^{n+2} \propto R^{-n-3} \,. \tag{2.3.11}$$

The hierarchical clustering scenario

By associating a mass $M = \frac{4\pi}{3} R^3 \overline{\rho}$ to regions of size R, we can write

$$\sigma_R^2 \propto M^{-\frac{n}{3}-1} \,; \tag{2.3.12}$$

this implies that as long as $n > -3$, σ_R^2 is a decreasing function of M. Smaller objects arise from larger density fluctuations, and therefore form at earlier times. Such picture is referred to as the *hierarchical clustering scenario*.

2.3.1 *Abundances of halos*

As mentioned at the beginning of this Section, we seek a statistical approach to the subject of Structure Formation. The first-order statistic we might investigate is the number counts of haloes and voids. Let us start by describing how to forecast the abundances of the collapsed haloes.

Press and Schechter formalism for over-densities

Press and Schechter [167] calculated a relation for the abundances of virialized objects from a hierarchical density field. We consider the smoothed density contrast δ_R to be initially a Gaussian random field with probability distribution function as described by:

$$P(\delta; R)d\delta = \frac{1}{\sqrt{2\pi\sigma_R^2}} \exp\left(-\delta^2/2\sigma_R^2\right) d\delta \,. \tag{2.3.13}$$

where $P(\delta; R)$ is the probability of attaining a value of $\delta(\vec{x}; R)$ between δ and $\delta + d\delta$.

In a hierarchical model, there are structures on all scales and the variance tends to infinity as the smoothing scale, R, approaches zero.The Press and Schechter [167] hypothesis is that objects will collapse on a scale within regions of R, once the smoothed density on that particular scale exceeds a threshold value. We may pick as critical density $\delta_c = 1.686$, which - as presented in Equation 2.2.11 - is the threshold for the non-linear collapse in the linear theory.

The mass within a region in which the smoothed density fluctuation reaches the critical value δ_c, corresponds to an object that has just virialized with mass $M(R)$. The relation between mass and scale is set by the volume of the window function (e.g. $M = 4\pi\rho_M R^3/3$ for a top-hat filter). Any region that exceeds the threshold δ_c, will have density equal to δ_c if smoothed on a larger scale R', where $R' > R$. Thus, the fraction of collapsed objects with size equal to or larger than R can be calculated as cumulative probability for a region to have a smoothed density above the threshold; by integrating Equation 2.3.13 we find this probability to be:

$$F(M) = \int_{\delta_c}^{\infty} p(\delta_R)d\delta_R = \frac{1}{2}\mathrm{erfc}\left(\frac{\nu}{\sqrt{2}}\right) , \tag{2.3.14}$$

where erfc is the complimentary error function and $\nu \equiv \delta_c/\sigma_R$ is the height of the threshold in units of the standard deviation of the smoothed density field.

Since $F(R \to 0, \delta_c) = F(\sigma_R \to 0, \delta_c) = 1/2$, this approach seems to neglect half of the collapsed objects. In order to solve this issue, we might argue as follow. Let us consider a large value of R that is decreasing step-wise and the associated set of values for δ_R. According to Equation 2.3.13 and assuming a Fourier-space top-hat window

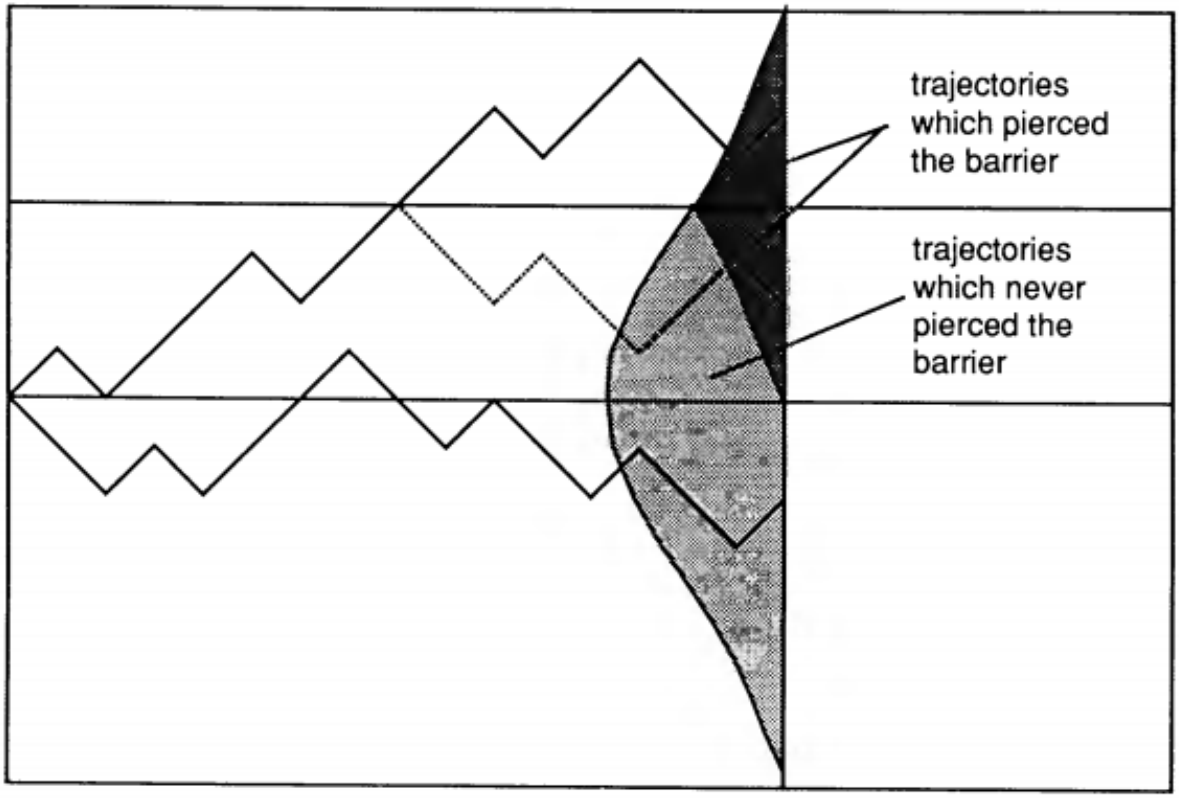

Figure 2.2: Schematic random walks performed by δ_R for decreasing values of R (i. e. increasing values of σ_R). The upper horizontal line shows the threshold barrier $\delta_R = \delta_c$ while the lower line shows the limit $\delta_R = 0$. Credit: Bond et al. [30].

function (case in which the smoothed density at scales R and R' are independent – if $R \neq R'$), δ_R performs a random walk as presented in Figure 2.2. Every walk that crosses the threshold upwards at a given R' has a mirror-symmetric "partner" that goes below the threshold once more after $\delta_{R'} = \delta_c$. Therefore, when estimating Equation 2.3.14 we have to include all walks that have already crossed the threshold and collapsed at $R' > R$, which produces a factor of two [see 30]

The random walks that up-cross the threshold multiple times (*cloud-in-cloud*) are not effecting this calculation: as they will fall into a larger collapsing region, they will be sub-summed by the latter, and should not be counted as individual objects (for void counting this will instead constitute an issue). Thus, the essential quantity to describe the number of collapsed objects of size R is given by the first crossing distribution:

$$f(\sigma_R, \delta_c) \equiv \frac{dF}{d\sigma_R^2} = \frac{\delta_c}{\sqrt{2\pi}\sigma_R^3} \exp\left(-\frac{\delta_c^2}{2\sigma_R^2}\right). \tag{2.3.15}$$

Equation 2.3.15 can be directly related to the number density of halos using $dn = \frac{\bar{\rho}}{M}|dF|$, hence:

$$\frac{dn}{dM} = \frac{\overline{\rho}}{M} f(\sigma_R, \delta_c) \left| \frac{d\sigma_R^2}{dM} \right| , \tag{2.3.16}$$

where $\frac{dn}{dM}$ is the halo mass function, expressing the expected number of density of halos in mass range between M and $M + dM$. If we formulate this in terms of $\nu = \delta_c / \sigma_R$, and note that

$$d \log \sigma_R^2 = \frac{d\sigma_R^2}{\sigma_R^2} = \frac{1}{\sigma_R^2} d \left(\frac{\delta_c^2}{\sigma_R^2} \right) = -\frac{2}{\sigma_R} \frac{\delta_c^2}{\nu^3} d\nu = -2 \frac{d\nu}{\nu} = -2 d \log \nu ,$$

we can then write:

$$\frac{dn}{dM} = \frac{\overline{\rho}}{M^2} \sigma_R^2 f(\sigma_R, \delta_c) \left| \frac{d \log \sigma_R^2}{d \log M} \right| = \frac{\overline{\rho}}{M^2} \nu f(\nu) \frac{d \log \nu}{d \log M} , \tag{2.3.17}$$

where

$$\nu f(\nu) = \sqrt{\frac{2}{\pi}} \exp \left(-\frac{\nu^2}{2} \right) . \tag{2.3.18}$$

Unlike σ_R, the functional form of this expression is independent of cosmology, so it is referred to as *universal* halo mass function.

Limitations of the Press and Schechter mass function

The Press and Schechter mass function gives us a reasonable understanding of how many collapsed halos we should find at a given mass, but it fails to predict the abundances of halos with high precision. Namely, this framework underestimates the number of low mass halos and over-predicts the abundances of high mass halos. Following the method of Bond et al. [30], Sheth, Mo, and Tormen [188] and Sheth and Tormen [189, 190], incorporated into the Press and Schecher mass function the effect of non-linear collapse approximation, together with a more sophisticated ellipsoidal collapse, achieving a better agreement with simulated data.

2.3.2 *Abundances of voids*

In order to assess the number function of voids, it should be possible to follow the formalism presented in the previous subsection albeit changing the threshold, from δ_c to the under-density δ_v. This representation is accurate initially, but eventually gravitational evolution destroys the symmetry between under- and over-densities. In fact, we may consider a random walk that up-crosses δ_c at some scale R and then down-crosses δ_v at scale $R' < R$. Such possibility correspond to a void embedded in a larger-scale over-density, a phenomenon known as *void-in-cloud* process. Analogously we can also define the

void-in-void phenomenon, which refers to the formation of sub-voids, the *cloud-in-voids* process and the *cloud-in-cloud* phenomenon, already discussed in the previous Section.

The trajectories of the random-walks are depicted in Figure 2.3 where also their corresponding regions in an N-body simulation are displayed. In the interest of selecting only the voids that survives all possible crossings, Equation 2.3.15 has to be modified, excluding all of the voids that are affected by the void-in-cloud process. The number of voids of size R is determined by the fraction of walks that cross the threshold δ_v at R, minus the fraction of those that – before reaching δ_v – had crossed δ_c at all $R' > R$. This last term is a product of the fraction of all walks that cross δ_c at R' times the fraction of walks that crossed δ_v at R (under the condition of having already crossed δ_c at R') and needs to be integrated over all R'; i. e.

$$f(\sigma_R, \delta_v, \delta_c) = f(\sigma_R, \delta_v) - \int_0^{\sigma_R^2} f(\sigma_{R'}, \delta_c) f(\sigma_R, \delta_v | \sigma_{R'}, \delta_c) d\sigma_{R'}^2 \,. \quad (2.3.19)$$

As shown by Sheth and van de Weygaert [191], the solution to Equation 2.3.19 can be found employing Laplace transforms and including in such calculation the variable D, defined as *void-and-cloud parameter*:

The void-and-cloud parameter

$$D \equiv \frac{|\delta_v|}{\delta_c + |\delta_v|} \,. \quad (2.3.20)$$

D quantifies the importance of the void-in-cloud process by means of the relative difference between the values of δ_c and δ_v. To name an example, the total mass fraction inside voids is:

$$\int f(\sigma_R, \delta_v, \delta_c) d\sigma_R^2 = 1 - D = \frac{\delta_c}{\delta_c + |\delta_v|} \,. \quad (2.3.21)$$

For $\delta_c \gg |\delta_v|$, D is very small and voids include almost all the mass in the Universe. Vice-versa, if $\delta_c \ll |\delta_v|$, nearly all mass is bounded inside halos.

Equation 2.3.19 can be manipulated into a simpler approximate form for $\delta_c/|\delta_v| \gtrsim 1/4$ [see 191]

$$\nu f(\nu) \approx \sqrt{\frac{2}{\pi}} \nu \exp\left(-\frac{\nu^2}{2}\right) \exp\left[\frac{|\delta_v|}{\delta_c}\left(\frac{D}{2\nu}\right)^2 - 2\left(\frac{D}{\nu}\right)^4\right] \,, \quad (2.3.22)$$

where, in this case, $\nu = |\delta_v|/\sigma_R$. The first term of the left hand side corresponds to Equation 2.3.15, while the second term accounts for the void-in-cloud phenomenon. The two exponential terms rapidly decay at very low and very high values of ν, therefore the void-distribution is peaked around $\nu \approx 1$, as presented in Figure 2.4 for

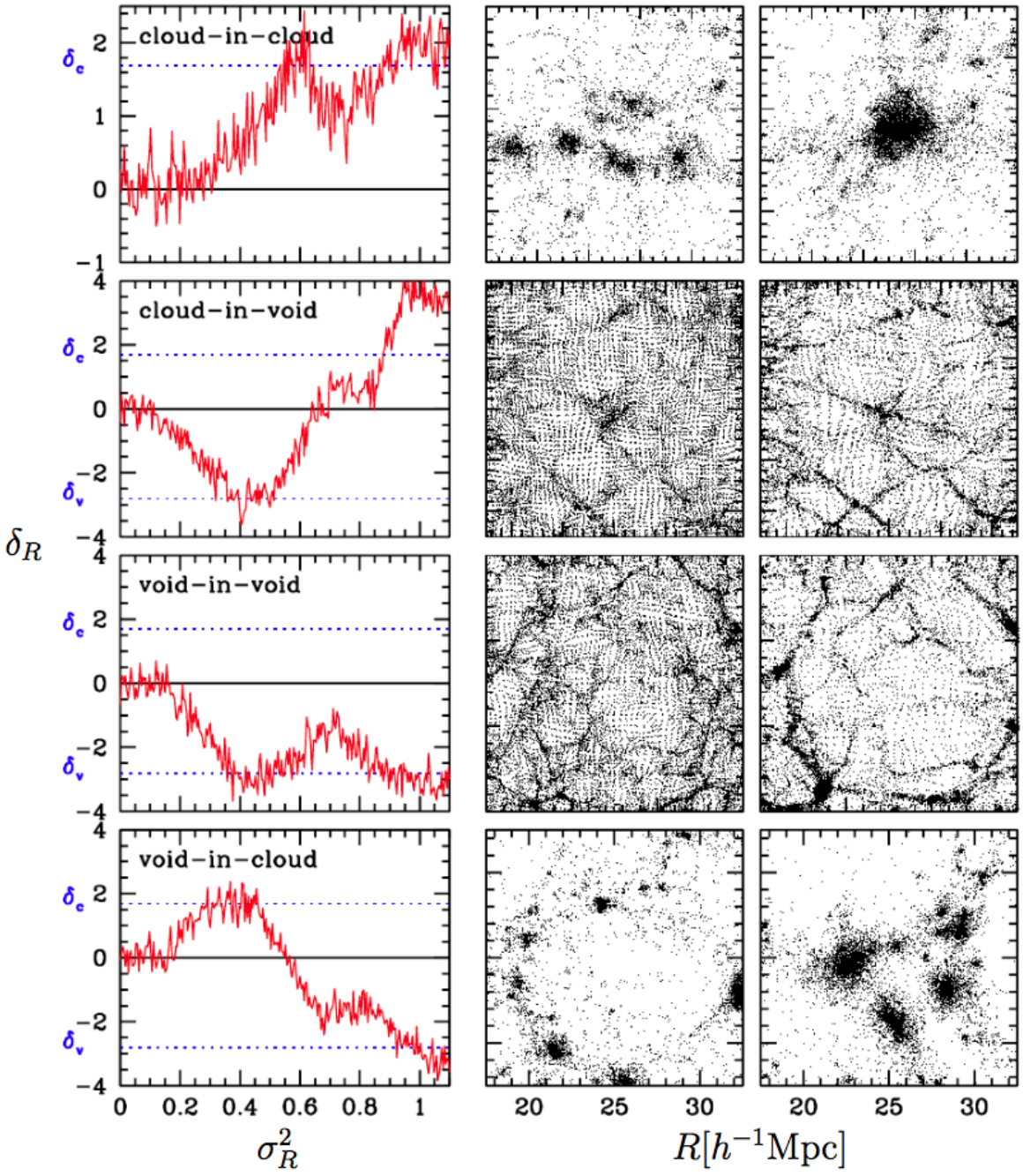

Figure 2.3: Random walks performed by δ_R in four distinct cases. The right panels show the associated evolution of the particle distribution in an N-Body simulation. Credit: Sheth and van de Weygaert [191].

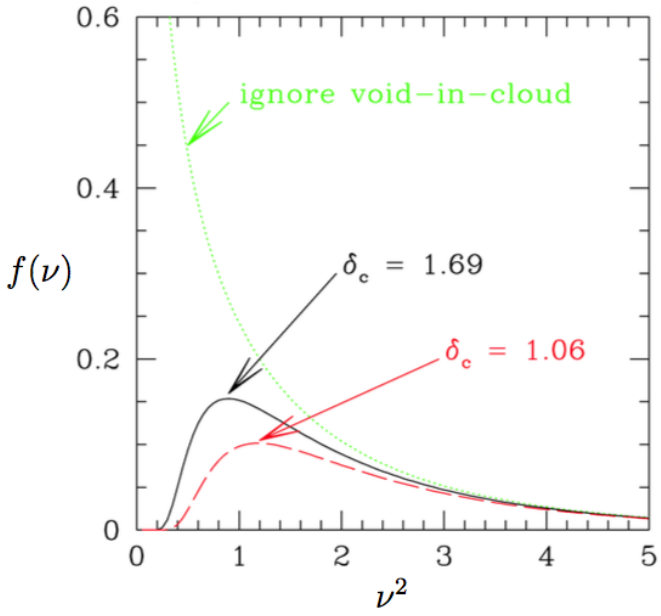

Figure 2.4: Equation 2.3.22 with $\delta_c = 1.06$ (dashed), $\delta_c = 1.69$ (solid) and $\delta_c \to \infty$ (dotted); $\delta_v = -2.81$ in each case. Credit: Sheth and van de Weygaert [191].

three different values of δ_c. The value of δ_c mostly effects small voids through the void-in-cloud process, while the abundances of large voids is determined by δ_v only.

The typical comoving size of voids can be roughly estimated using Equation 2.3.11, which states that $\sigma_R^2 \propto R^{-n-3}$. If $\nu \approx 1$ then $\sigma_R \approx |\delta_v|$ and therefore the size of the excursion set region when it crosses the threshold δ_v is:

$$R \approx 8h^{-1}\mathrm{Mpc}\left(\frac{\sigma_8}{|\delta_v|}\right)^{\frac{2}{n+3}}. \tag{2.3.23}$$

After the shell crossing the void expands non-linearly; according to spherical evolution, it stretches by a factor of 1.697. Assuming $\sigma_8 = 0.83$, $|\delta_v| = 2.717$, $n = -1.5$ we then obtain $r_v \approx 3h^{-1}$Mpc. In analogy to Equation 2.3.16, we could define a void mass function. Nevertheless, a more fitting quantity to describe voids is their volume V_v, or, simply their effective radius

$$r_v \equiv \left(\frac{3}{4\pi}V_v\right)^{1/3}. \tag{2.3.24}$$

The comoving volume of a void can be linked to its mass M and initial excursion set scale R through:

$$V_{\rm v} = \frac{M}{\rho}\left(\frac{r_{\rm v}}{R}\right)^3 \tag{2.3.25}$$

where $r_{\rm v}/R \approx 1.697$ is found following the spherical evolution. In this manner Equation 2.3.17 can be manipulated into

$$dM = \left(\frac{R}{r_{\rm v}}\right)^3 \overline{\rho} dV_{\rm v} = \left(\frac{R}{r_{\rm v}}\right)^3 \overline{\rho} 4\pi R_{\rm v}^2 dr_{\rm v} = 3M d\log r_{\rm v}\,,$$

leading to

$$M = 3\log r_{\rm v}.$$

This provide the following void size function:

$$\frac{dn}{d\log r_{\rm v}} = \frac{1}{V_{\rm v}}\left(\frac{r_{\rm v}}{R}\right)^3 \nu f(\nu)\frac{d\log\nu}{d\log r_{\rm v}}\,. \tag{2.3.26}$$

We can also predict the cumulative fraction of voids with a size greater than a fixed size $r_{\rm v}$,

$$F_{\rm v}(r_{\rm v}) = \int_0^\infty \frac{dn}{d\log R'_{\rm v}} V_{\rm v} d\log R'_{\rm v} = \left(\frac{r_{\rm v}}{R}\right)^3 \int_{\nu(r_{\rm v})}^\infty \nu f(\nu) d\log\nu\,, \tag{2.3.27}$$

which, expressed for voids of all sizes (i. e. $r_{\rm v} = 0$), turns into:

$$F_{\rm v}(0) = \left(\frac{r_{\rm v}}{R}\right)^3 (1 - D)\,. \tag{2.3.28}$$

Considering the following values $\delta_{\rm v} = -2.717$, $\delta_c = 1.686$, and $r_{\rm v}/R = 1.697$ we obtain $F_{\rm v}(0) \approx 1.871$, which, exceeding the unity, is non-physical. To prevent this, we might relax the shell-crossing condition by choosing a less negative value for $\delta_{\rm v}$ and calculating the corresponding non-linear void-stretch $r_{\rm v}/R$ with Equation 2.2.14. In this manner $F(0)$ becomes smaller, but, on the other hand, the number of large voids increases. Only for $\delta_{\rm v} \to 0 \Rightarrow D \to 0\,\text{and}r_{\rm v}/R \to 1$ we recover physicality with $F_{\rm v}(0) = 1$.

It is worth stressing that in the derivation of Equation 2.3.28 we have assumed that the number density of voids is conserved during non-linear evolution. However, due to the finite amount of available volume in the Universe, many voids will end up merging with each other. This suggests the total volume to be conserved, rather than their number density as proposed by Jennings, Li, and Hu [105]. If we request $F_{\rm v}(r_{\rm v}) = F_{\rm v}(R)$ during the non-linear evolution, we obtain

$$V_{\rm v} dn(r_{\rm v}) = V dn(R)\,, \tag{2.3.29}$$

which alters Equation 2.3.26 into

$$\frac{dn(r_{\rm v})}{d\log r_{\rm v}} = \frac{V}{V_{\rm v}}\frac{dn(R)}{d\log R}\frac{d\log R}{d\log r_{\rm v}} = \frac{1}{V_{\rm v}}\nu f(\nu)\frac{d\log \nu}{d\log r_{\rm v}}\,. \tag{2.3.30}$$

In this case though we have assumed that $d\log(r_{\rm v})/d\log r_{\rm v} = 1$, which applies in the spherical evolution model, but may not be realistic in general. Anyhow, under this assumption the total void volume fraction becomes $F_{\rm v}(0) = 1 - D$, obeying physicality for all values of $\delta_{\rm v}$ and δ_c and in particular $F_{\rm v}(0) \approx 0.383$ for $\delta_{\rm v} = -2.717$ and $\delta_c = 1.686$.

2.3.3 *The bias of tracers*

We have summarized a way to predict the number of voids and haloes in the matter distributed among the Cosmos. Since our goal is to compare our prediction with observations, we must consider a further complication: the matter we have discussed so far is not visible, as, by definition, it interacts only gravitationally. What we can indeed observe directly is the light, emitted by the stars in galaxies. Galaxies are hosted in matter halos, which, as we have explained in this Chapter, are peaks in the density field. Hence, by employing galaxies or clusters of galaxies to trace the matter in the Universe, we expect our statistical analysis to be *biased* toward the highest peaks of the density field. This was pointed out for the first time in a seminal paper by Kaiser [106], who studied the properties of the spatial correlation of Abell clusters. Perhaps the easiest manner to express the *halo bias* is provided by the comparison of the clustering properties of matter and halos. In fact, being $\xi_{\rm mm}$ the matter-matter correlation function and $\xi_{\rm hm}$ the correlation function between halos and matter-particles, we can write:

$$\xi_{\rm hm} = b_{\rm h}\xi_{\rm mm} \tag{2.3.31}$$

where $b_{\rm h}$ is the halo bias, which, for the time being, is just an unknown function of space and time.

The excursion set formalism provides a neat framework in which to understand the relative clustering of halos. The idea is to count the number of collapsed haloes within a scale S_0 with smoothed density δ_0, and then compare this number with that of all collapsed haloes. The fraction of mass embed in collapsed haloes with $M_h > M$, of

density δ_0 within a smoothing scale S_0 is given by Equation 2.3.14, and reads:

$$F(M|\delta_0, S_0) = \text{erfc}\left(\frac{\delta_c - \delta_0}{2\Delta S}\right).$$

where $\Delta S \equiv S - S_0$ (Please note that we have defined $S \equiv \sigma 2_R$). As the density of the region increases, F increases, and finally if $\delta_0 \to \delta_c$ then $F \to 1$, i. e. the whole region within the smoothing scale is then interpreted as a collapsed halo.

The fraction of mass in halos within mass range M and $M + dM$ is given by:

$$\begin{aligned} f(M|\delta_0, S_0)\left|\frac{dS}{dM}\right| dM \equiv \frac{F(M|\delta_0, S_0)}{dM} dM = \\ = \frac{1}{\sqrt{2\pi}} \frac{\delta_c - \delta_0}{\Delta S}\left|\frac{dS}{dM}\right| \exp\left[-\frac{(\delta_c - \delta_0)^2}{2\Delta S}\right] dM, \end{aligned} \tag{2.3.32}$$

and regions with smoothed density δ_0 on scale S_0 contain (on average), a number of haloes given by:

$$N(M|\delta_0, S_0)dM = \frac{M_0}{M} f(M|\delta_0, S_0)\left|\frac{dS}{dM}\right| dM\,. \tag{2.3.33}$$

With Equation 2.3.33, we can estimate our quantity of interest, i. e. the relative over-abundance of halos in denser regions compared to the mean density of all halos, which is given by:

$$\delta_{\rm h}^L = \frac{N(M|\delta_0, S_0)}{(dN(M)/dM)V_0} - 1 \tag{2.3.34}$$

where the superscript L indicates that $\delta_{\rm halo}^L$ is calculated in the initial Lagrangian space, and it is determined by the mass distribution at some early stage (ignoring the dynamical evolution). If the relative over-density is computed with respect to sufficiently large regions ($S_0 \ll S$ and $\delta_0 \ll \delta_c$) it has a rather simple expression. This can be calculated by expanding at the first order in the variables S_0/S and δ_0/δ_c and reads:

$$\delta_{\rm h}^L = \frac{\nu^2 - 1}{\delta_c}\,\delta_0 \tag{2.3.35}$$

where $\nu = \delta_c/\sqrt{S} = \delta_c/\sigma(M)$.

The final step requires a paradigm to properly map the initial Lagrangian space into the Eulerian space. Such model was provided by Mo and White [133], who, in the limit of small over-density, conclude that:

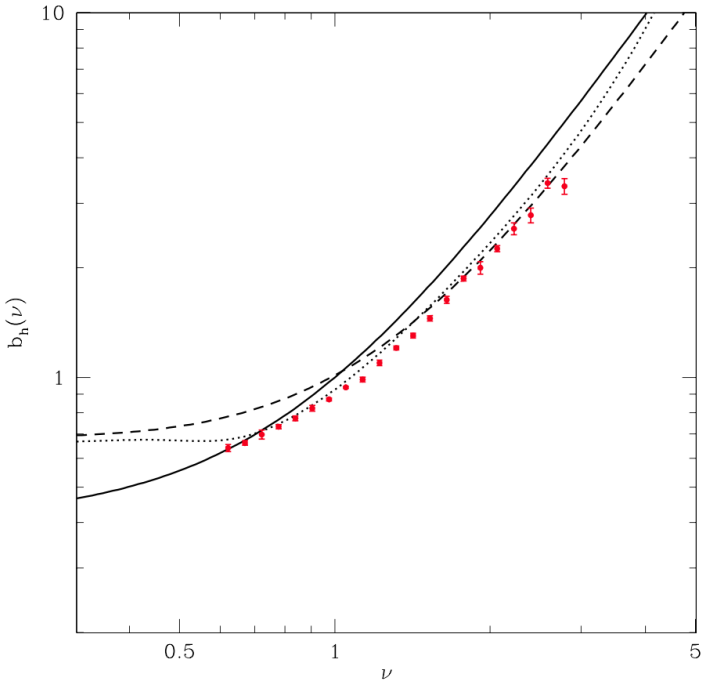

Figure 2.5: Large scale bias of dark matter halos as a function of ν. The solid line shows the excursion set result presented in Equation 2.3.37. The dashed line displays the bias calculated employing a modified form for the barrier criterion by Sheth and Tormen [189] and finally the dotted line represents an empirical fit to N-body simulation results by Seljak and Warren [187]. The points in red are numerical data provided by J. L. Tinker. Credit: Zentner [223].

$$\delta_{\rm h} = \left(1 + \frac{\nu^2 - 1}{\delta_c}\right) \delta_0 \,, \tag{2.3.36}$$

where $\delta_0 \ll 1$, $V \approx V_0(1+\delta)$, $\delta \approx \delta_0$, being V and δ the Eulerian space variables corresponding to the Lagrangian space variables V_0 and δ_0. We can thereby define the halo bias $b_{\rm h}$ as

$$b_{\rm h} \equiv 1 + \frac{\nu^2 - 1}{\delta_c} \Rightarrow \delta_{\rm h} = b_{\rm h}\delta_0 \,. \tag{2.3.37}$$

The halo over-density is proportional to the matter over-density. Larger halos will have a larger value of ν because $\sigma(M)$ decreases with mass, therefore larger halos cluster significantly more strongly than the overall clustering of mass.

In Figure 2.5 we report the bias presented in Equation 2.3.37 as a function of ν with a solid line, and we compare its prediction with the dotted red points that are computed from a suite of N-body simulations. Equation 2.3.37 provides a good understanding of the bias features, but the standard excursion set formalism fails to reproduce the halo bias in details. A possible improvement consists of modifying the shape of the barriers as a function of the smoothing scales, as presented by Sheth and Tormen [189]: we plot this result with the dashed line. Seljak and Warren [187] provide an empirical fit to simulated data, which is graphed by the dotted line.

We have finally arrived at the pivot point of this thesis: voids in the observable Universe can only be traced using the galaxies population that we can map in large surveys. But galaxies are biased tracers of the underlying matter density. Therefore, prediction on void statistics (such as those presented in Section 2.3.2) to forecast the number of voids), *have to be corrected for the impact of the bias*. The second part of this thesis is devoted to the description of this effort. Namely we research if and how the bias of tracers impacts the void definition and their statistics.

Part II

ORIGINAL WORK

In the second part of the thesis our novel results are presented and discussed.

3

COSMIC VOIDS IN COUPLED DARK ENERGY COSMOLOGIES: THE IMPACT OF HALO BIAS

This Chapter was written in collaboration with Marco Baldi, Federico Marulli and Lauro Moscardini. Its results are published in Pollina et al. [164].

A summary of this Chapter

In the analysis we are about to present, we study the properties of cosmic voids in standard and coupled dark energy cosmologies. Using large numerical simulations, we investigate the effects produced by a possible dark energy coupling on three statistics: the filling factor, the size distribution and the stacked profiles of cosmic voids. We find that the bias of the tracers of the density field used to identify the voids strongly influences the properties of the void catalogues, and, consequently, the possibility of using the identified voids as a probe to distinguish coupled dark energy models from the standard ΛCDM cosmology. In fact, on one hand coupled dark energy models are characterised by an excess of large voids in the cold dark matter distribution as compared to the reference standard cosmology, due to their higher normalisation of linear perturbations at low redshifts. Specifically, these models present an excess of large voids with $r_v > 20, 15, 12\ h^{-1}\,\mathrm{Mpc}$, at $z = 0, 0.55, 1$, respectively. On the other hand, we do not find any significant difference in the properties of the voids detected in the distribution of collapsed dark matter haloes. These results imply that the tracer bias has a significant impact on the possibility of using cosmic void catalogues to probe cosmology.

Organisation of this Chapter

We will proceed as follows. In Section 3.1 we provide an overview of the state-of-the-art related to this analysis. In Section 3.2 we briefly describe the cDE models considered in the this Chapter and we recall the main features of the CoDECS runs. In Section 3.3 we describe the void finder algorithm and our method of analysis, and in Section 3.4 we present the properties of voids in the CoDECS simulations. Our conclusions are summarised in Section 5.5.

3.1 INTRODUCTION

Despite the fact that the presently accepted standard cosmological model, the so-called ΛCDM scenario, appears to be fully consistent with most of the available observations [see e.g. 160, and Part I of this Thesis], it still presents some open issues in the detailed description of the distribution of matter at small scales.

The void phenomenon

One of such properties that still appears problematic is the observed abundance of dwarf galaxies in the underdense regions of the Universe, which is found to be significantly lower than what predicted by large N-body simulations carried out within the ΛCDM cosmology. This problem, that was pointed out for the first time by Peebles [152], goes under the name of the *void phenomenon*, and it has been discussed by several authors over the past years [see e.g. 209, 214].

Problems of ΛCDM

Besides the poor theoretical understanding of a Cosmological Constant as source of the observed accelerated expansion of the Universe [217], the void phenomenon is therefore one of the few observational tensions that motivate the investigation of alternative cosmological scenarios, together with the so-called *cusp-core problem* [224], the *satellite problem* [34], the *too big to fail problem* [32], and the recently detected tension between the CMB- and cluster-based estimations of σ_8, the r.m.s. of the mass density field within a sphere of radius 8 h^{-1} Mpc [159].

Strong coupling and fifth force

A relevant class of alternative cosmological models that has been widely investigated in recent years is given by the so-called coupled dark energy scenario [cDE hereafter, see e.g. 9, 10, 16, 76, 220]. In these models a dynamical scalar field sourcing the accelerated cosmic expansion [see e.g. 170, 219] is coupled to cold dark matter (CDM) particles resulting in a direct exchange of energy-momentum between these two cosmic components. Such interaction gives rise to a new fifth force acting on CDM particles, possibly capable to make the voids emptier [143]. Other possible ways to address the void phenomenon have been proposed, such as, for example, a modification of gravity at very large scales [49, 120, 196].

The main effects of cDE models on the large-scale matter distribution in the Universe, as well as on the structural properties of highly non-linear collapsed objects (such as galaxies and galaxy clusters), have been widely investigated in the recent past by several works mostly based on dedicated large N-body simulations [see e.g. 13, 15, 18, 41, 42, 46, 85, 122, 124, 128, 134]. However, in these rich and high-dense environments the effects produced by cDE are expected to be significantly modified by the complex and not yet fully understood baryonic processes occurring within astrophysical objects. Therefore, studying the properties of underdense regions of the universe might represent a complementary approach to investigate cDE scenarios, and might provide a direct test of such cosmological models through a direct comparison with the properties of the observed cosmic voids.

While the first models for void evolution [23, 98] have been developed soon after their earliest observations [88, 108], it is only in recent years that systematic studies about voids have become possible thanks to the increasing depth and volume of current galaxy surveys

and to the advent of large numerical simulations that allow to predict with high accuracy the topology of the cosmic web.

The recent interest for cosmic voids is mostly related to their yet unexploited potential to probe cosmological models and constrain cosmological parameters, thanks to the claimed universality of their general statistical and structural properties [see e.g. 52, 92, 174, 175]. In particular, voids might represent a population of ideal spheres with a homogeneous distribution in the Cosmos at different redshifts, so that their size evolution can be used to characterise the expansion history of the Universe by means of the Alcock & Paczynski (AP) test [6, and see Section 1.3.2], as already pointed out by recent works [204, 206].

The many intriguing aspects of voids

Furthermore, voids might have an impact on the observed properties of the CMB. It has been investigated whether the observed Cold Spot in the Cosmic Microwave Background (CMB) could be explained as Integrated Sachs-Wolfe (ISW) imprint caused by very large voids along the line of sight [e.g., 77, 111, 113, 139, 171], and a final conclusion on this topic is yet to be reached; the potential of the ISW by voids is nevertheless important and still being actively investigated [e.g. 37, 87, 112, 135]. The next generation of large galaxies surveys such as the ESA Euclid mission [8, 116] are expected to detect gravitational lensing from medium size voids with which it will be possible to directly constrain the void density profiles without resorting on luminous tracers like galaxies, which would require to model their bias [50, 104, 114, 132].

Cosmic voids are therefore one of the most appealing and promising cosmological probes: being almost empty, their growth during the cosmic history should be at most weakly non-linear and their properties could be possibly affected by the nature of DE and by the properties of the primordial density field in which they evolve [31, 57, 84, 145]. In particular, the shape of voids has been shown to be very sensitive to the equation of state of the DE component [117]. Defining the properties of voids in different cosmological models can then represent an important handle to discriminate between these models.

In this Chapter we focus on the investigation of the properties of voids in the standard ΛCDM cosmology, as well as in a series of competing cDE models. This has been done by extracting the population of voids from both the cold dark matter and the halo distributions arising in large cosmological N-body simulations of these different cosmological scenarios. To this end, we made use of the publicly available data of the CoDECS simulations [14], including three different models of DE interaction besides a ΛCDM reference run. We identified cosmic voids in the CoDECS runs with VIDE [Void IDentification and Examination toolkit, 210], a substantially modified version of the publicly-available void finder ZOBOV [ZOnes Bordering On Voidness, 141], and compared the statistical and structural properties of the re-

Goals and results

sulting void catalogues. Our results show that cDE models are characterised by an excess of large voids in the CDM distribution with respect to the reference ΛCDM cosmology, as expected from their higher normalisation of linear perturbations at low redshifts. This is consistent with the theoretical predictions on the abundance of voids presented in Pisani et al. [156], while the latter work seems to be in contrast with the recent findings of Sutter et al. [209] for the case of coupled dark energy simulations normalised to the same perturbations amplitude. In fact the simulations analysed in this Chapter are normalized at CMB time, therefore they have different values of σ_8 today: this feature, following Pisani et al. [156], leads to an excess of large voids (that we observe). On the other hand Sutter et al. [209] focus on simulations which are normalized at $z = 0$: therefore the excess of large voids detected by Sutter et al. [209] at $z = 0$ appears to be in contrast with Pisani et al. [156].

Nonetheless, we also found that the differences in the cosmic-void properties among these different models significantly change when voids are identified in the distribution of collapsed haloes rather than in the CDM distribution itself. Namely, the deviation from ΛCDM is no longer significant. A similar result has been found by Cai, Padilla, and Li [36] for $f(R)$ models and by Barreira et al. [21] for Galileon and Nonlocal gravity cosmologies: these works focus on lensing signals by empty regions but, studying the basic statistical properties of voids, they both conclude that voids in CDM show significant variations while voids in haloes do not. This is a quite remarkable agreement considering that our work, Cai, Padilla, and Li [36] and Barreira et al. [21] use different void finders: VIDE, an improved version of Padilla, Ceccarelli, and Lambas [147] and the Watershed Void Finder (WVF) algorithm [161] respectively. It is in fact well known that the "large number of quite different void-finding algorithms has so far got in the way of groups comparing their results without worrying about whether this comparison makes sense" [53]. While Barreira et al. [21] relate the drop of deviation between models for the case of voids in haloes to the poor statistic of haloes as tracers of the density, Cai, Padilla, and Li [36] have already suggested that the source of the effect might be the halo bias. In this Chapter we will demonstrate convincingly by sub-sampling the dark matter distribution to the same number density as the halo catalogue that the poor statistic of haloes is not enough to explain the different properties shown by voids in haloes and voids in CDM. Furthermore, Nadathur and Hotchkiss [137] independently drew the same conclusion using a ΛCDM N-body simulation. All of these results suggest that, contrary to what has been claimed in some other recent works [see e.g. 209], the bias of the tracers of the density field employed to identify voids might have a significant impact on the possibility of using the obtained void catalogues to probe cosmology. Therefore, in the present

Comparison with similar studies

work we will show that a random sub-sampling of a simulated CDM distribution to match the density of tracers expected for any given galaxy survey does not actually provide a faithful representation of the discriminating power of the survey with respect to different competing cosmological models.

3.2 COUPLED DARK ENERGY COSMOLOGIES

3.2.1 *The models*

We aim at studying the statistical and structural properties of voids in the context of coupled dark energy (cDE) cosmologies. In these models, dark energy is represented by a classical scalar field ϕ moving in a self-interaction potential $V(\phi)$ and directly interacting with CDM particles through an exchange of energy-momentum, quantified by a coupling function $\beta(\phi)$. We will give only a very essential summary of the main features of cDE models, and we refer the reader to Amendola [9], Baldi [13], and Baldi [16] for a more thorough discussion.

Background evolution

The background dynamics of cDE cosmologies is described by the set of equations:

$$\dot{\rho}_r + 4H\rho_r = 0\,, \tag{3.2.1}$$

$$\dot{\rho}_b + 3H\rho_b = 0\,, \tag{3.2.2}$$

$$\dot{\rho}_c + 3H\rho_c = -\sqrt{\frac{2}{3}}\beta_c(\phi)\frac{\rho_c\dot{\phi}}{M_{Pl}}\,, \tag{3.2.3}$$

$$\ddot{\phi} + 3H\dot{\phi} + V'(\phi) = \sqrt{\frac{2}{3}}\beta_c(\phi)\frac{\rho_c}{M_{Pl}}\,, \tag{3.2.4}$$

where the subscripts r, b, c and ϕ, indicate the energy densities ρ of radiation, baryons, CDM, and the dark energy field ϕ, respectively, and where the Hubble function is given as usual by

$$H^2 = \frac{8\pi G}{3}\left(\rho_\mathrm{r} + \rho_\mathrm{c} + \rho_\mathrm{b} + \rho_\phi\right)\,, \tag{3.2.5}$$

with $M_{Pl}^2 \equiv 1/8\pi G$ being the reduced Planck mass. In the above equations the field ϕ is expressed in units of M_Pl and an overdot represents a derivative with respect to cosmic time while a prime denotes a derivative with respect to the field itself. The source terms on the right-hand side of Eqs. 3.2.3 and 3.2.4 define the interaction between the dark matter and the dark energy components, with a strength given by the coupling function $\beta_c(\phi)$.

Linear evolution

At the level of linear density fluctuations, the interaction modifies the gravitational instability processes that govern the evolution of perturbations as a consequence of a long-range *fifth* force mediated by the dark energy field and acting between CDM fluid elements. In the Newtonian limit and on sub-horizon scales, these effects turn into the following set of modified linear equations [7, 17, 155]:

Table 3.1: A summary of the cosmological models investigated in the present work and their main parameters. See Baldi [13] for details.

Model	Potential	α	$\beta(\phi)$	$w_\phi(z=0)$	$\sigma_8(z=0)$
ΛCDM	$V(\phi) = A$	–	–	-1.0	0.809
EXP003	$V(\phi) = Ae^{-\alpha\phi}$	0.08	0.15	-0.992	0.967
EXP008e3	$V(\phi) = Ae^{-\alpha\phi}$	0.08	$0.4\exp[3\phi]$	-0.982	0.895
SUGRA003	$V(\phi) = A\phi^{-\alpha}e^{\phi^2/2}$	2.15	-0.15	-0.901	0.806

$$\ddot{\delta}_c = -2H\left[1-\beta_c\frac{\dot{\phi}}{\sqrt{6}H}\right]\dot{\delta}_c + 4\pi G[\bar{\rho}_b\delta_b + \bar{\rho}_c\delta_c\Gamma_c]\,, \quad (3.2.6)$$

$$\ddot{\delta}_b = -2H\dot{\delta}_b + 4\pi G[\bar{\rho}_b\delta_b + \bar{\rho}_c\delta_c]\,, \quad (3.2.7)$$

where $\bar{\rho}_i$ represents the background density of the i-th fluid and $\delta_i \equiv \delta\rho_i/\bar{\rho}_i$ its density perturbation. The factor $\Gamma_c \equiv 1 + 4\beta_c^2/3$ represents the additional fifth force appearing only in the CDM equation while the term $\beta_c\dot{\phi}$ is a velocity-dependent acceleration arising as a consequence of momentum conservation. Similar additional terms characterise the interaction among a discrete set of CDM particles in the non-linear regime [see 18].

3.2.2 *The CoDECS simulations*

For our investigation we will make use of the publicly available data of the CoDECS simulations [13]. These simulations are carried out with a suitably modified version of the TreePM N-body code GADGET [201] that self-consistently implements all the above mentioned effects characterising cDE cosmologies [18].

For the present work, we will employ the outputs of the L-CoDECS simulations, which follow the evolution of 1024^3 CDM particles and as many baryonic particles in a periodic cosmological box of 1 comoving Gpc/h a side. Both CDM and baryonic particles are treated as collisionless particles, but they experience different accelerations as a consequence of the interaction between the CDM and the dark energy fields.

The CoDECS suite includes six different cosmological models, four of them are considered in this Chapter: the reference ΛCDM cosmology, a cDE model (EXP003) characterised by a constant positive coupling $\beta_c > 0$ and an exponential self-interaction potential of the form $V(\phi) = A\exp(-\alpha\phi)$, a further model (EXP008e3) with the same potential but with an exponential coupling, $\beta_c(\phi) = \beta_0\exp(\beta_1\phi)$, and a final scenario (SUGRA003) with a constant negative coupling, $\beta_c < 0$ and a SUGRA [33] self-interaction potential $V(\phi) = A\phi^{-\alpha}\exp(-\phi^2/2)$. A summary of the models parameters is shown in Table 3.1. All the models have the same amplitude of perturbations at $z = z_{\rm CMB}$, re-

sulting in a different amplitude of linear density perturbations at the present epoch (and consequently different values of σ_8).

In the present work we will also make use of the public halo catalogues of the CoDECS simulations, that have been generated through a Friend-of-Friend (FoF) algorithm with a linking length of 0.2 times the mean inter-particle separation.

3.3 VOID FINDING

We employ the publicly available void finder VIDE [210] to identify voids in the CDM and halo distributions extracted from the snapshots of the CoDECS simulations within the different cosmological models described above. VIDE embeds the ZOBOV algorithm, which allows to identify depressions in the density distribution of a set of points. In the following, we provide a very short summary of how ZOBOV works, and we refer to the original ZOBOV paper [141] for a more detailed discussion.

The three steps of void-finding

Firstly, ZOBOV associates a cell to each tracer (a CDM particle or a halo) using a Voronoi tessellation scheme, i.e. the cell c associated to the particle (or halo) p is defined as the region of the box which is closer to p than to any other particle (or halo) in the box. Secondly, the algorithm identifies local density minima among these cells: a density minimum is defined as a Voronoi cell with a lower density (i.e. a larger volume) than all other cells around it. Thirdly, ZOBOV joins together the Voronoi cells surrounding a local density minimum until cells with larger and larger density are found, and it identifies voids as the union of these cells. Cosmic voids are joined together via the Watershed Transform [see 162], which naturally creates a hierarchy in the structures of voids. All these procedures are performed also by the ZOBOV version included in the VIDE toolkit. Additionally, VIDE provides several different void catalogues for which various types of sample selections (as e.g. different cuts on the void density contrast or on the void central overdensity) are applied on top of the original ZOBOV sample. In particular, as voids are found to define a complex hierarchy, with smaller voids being embedded in larger ones, VIDE provides for each identified void the corresponding hierarchy level, and according to this classification a sample of *main* voids (i.e. those cosmic voids that are not embedded in larger voids and that represent the top of their own void hierarchy) is produced. We employed a slightly modified version of this selection procedure to remove pathological voids from the catalogue and obtain a more statistically robust and convergent sample of main voids. More specifically, we observed that occasionally VIDE identifies as main voids (i.e. voids at the top of their own hierarchy) structures that nearly encompass the whole simulation volume. Such structures cannot obviously be real voids as their mean density must be close to the average cosmological density.

Sample selection

Nonetheless, being classified as main voids by VIDE, all the smaller (and more likely "real") voids embedded in these pathological structures would be discarded as sub voids in our void counting procedure. We have therefore applied a preliminary sanity check on all the voids that are classified as main voids by requesting that the diameter of the void must not exceed a half of the simulation box, besides the standard requirements on the void density contrast to be higher than 1.57 (see below). After removing from the sample of main voids all the objects not fulfilling these criteria, we have updated the classification of all their sub-voids, thereby obtaining a new set of main voids candidates, and repeated this procedure until no pathological voids are found[1].

Finally, since local density minima can also be found in over-dense regions, we decide to remove from the main void catalogues the voids with a density minimum larger than 20% of the mean density of the Universe (which is one of the standard cuts provided by VIDE). For each identified void, ZOBOV also calculates the probability that the void might arise in a uniform Poissonian distribution of points, which is directly related to the density contrast between the minimum density of the void and its boundary. As this density contrast is provided for each void also by the VIDE catalogue, we remove voids with a density contrast below 1.57, corresponding to a probability of arising as Poisson noise larger than 2σ [see 141].

Void-centre and void radius

VIDE defines voids as spherical regions centred in the barycenter, $\vec{x}_c$, of the underdense regions provided by ZOBOV, where:

$$\vec{x}_c = \frac{\sum_{i=1}^{N} \vec{x}_i^p \cdot V_i^p}{\sum_{i=1}^{N} V_i^p}\,, \tag{3.3.1}$$

and $\vec{x}_i^p$ and V_i are the positions of the $i-th$ tracer and the volume of its associated Voronoi cell, while N is the number of tracers included in the void. The radius of the sphere (i.e. the effective radius of the void, r_v) is then computed from the overall volume of the underdense region by assuming sphericity:

$$V_\mathrm{VOID} \equiv \sum_{i=1}^{N} V_i^p = \frac{4}{3}\pi r_\mathrm{v}^3\,. \tag{3.3.2}$$

It has been shown that different void finders based on dynamical criteria, instead of density or geometry criteria, might reduce the shot noise error [74]. Nevertheless, the void finder used here is accurate enough for the purpose of the present analysis, as we investigate

1 For the analyses presented in the next two Chapters this was no longer necessary. Either the problem was fixed in an updated of the software, or something cause this issue specifically in the data employed in this Chapter.

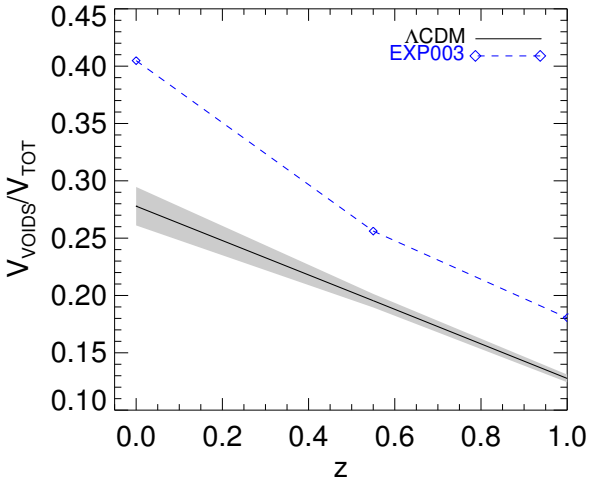

Figure 3.1: The redshift evolution of the volume fraction of voids identified in the CDM distribution for the ΛCDM (black solid line) and EXP003 (blue dashed line) models. The shaded area (shown only for ΛCDM) represents the uncertainty, computed with the jack-knife method.

the main properties of large voids extracted from dense numerical simulations.

3.4 THE STATISTICS OF VOIDS IN THE CODECS

With the catalogues of void extracted from the CoDECS simulations as described in the previous Section at hand, we perform some basic analyses of the statistical and structural properties of the voids in the different cosmologies, namely the voids filling factor (i.e. the fraction of the cosmic volume occupied by voids), their size distribution (i.e. the abundance of voids as a function of their size), and their stacked radial density profiles, and compare these observables to the reference ΛCDM case [see also 121]. We perform such comparison for voids identified both in a randomly sub-sampled CDM density field and in the distribution of collapsed haloes, to highlight how the use of tracers with different bias might result in a different relative behaviour of the models.

3.4.1 *Void statistics in the CDM distribution*

Let us start by considering the voids catalogues extracted from the CDM density field, i. e.directly from the CoDECS snapshots at different redshifts. To better handle the simulation data we have made use of the sub-sampling routine included in VIDE to randomly sub-sample the CDM particles of the simulation snapshots down to an average density of 2×10^7 particles per cubic $h^{-1}\,\mathrm{Gpc}$. For this com-

parison we will focus only on two out of the four models, namely the reference ΛCDM cosmology and the EXP003 scenario, which is the most extreme realisation (in terms of deviations at the background and linear perturbations level) of cDE models that we have at our disposal.

Filling-factor

First of all, we compare the evolution of the volume fraction occupied by voids at different cosmic times, also known as the void filling factor, to check whether the interaction between DE and CDM particles implemented in our extreme cDE model has an impact on such fraction. Fig. 3.1 displays the evolution of the voids volume fraction, $V_{\rm VOIDS}/V_{\rm TOT}$, where $V_{\rm VOIDS}$ is the sum of all the main voids volumes in a given snapshot of the simulation and $V_{\rm TOT}$ is the total volume of the box, i.e. $1\ h^{-3}\,{\rm Gpc}^3$. The statistical error, shown in Fig. 3.1 by the shaded grey region around the ΛCDM line, has been computed with a jackknife method.

As expected, the volume fraction of voids increases with time, irrespectively of the underlying cosmological model, due to gravitational instability. Moreover, as one can see from Fig. 3.1, the volume fraction occupied by voids in the cDE model EXP003 is significantly larger than in the reference ΛCDM cosmology, reflecting the higher normalisation of the amplitude of linear perturbations at low redshifts in EXP003. More quantitatively, the volume fraction in EXP003 is roughly 40% larger than the corresponding ΛCDM fraction, at all redshifts between $z = 1$ and $z = 0$. Clearly, the observed differences between the cDE model and the standard ΛCDM cosmology are statistically significant.

Void size function

As a second step, we compare the relative abundance of voids as a function of their size, by computing in the two cosmological models the differential size distribution, defined as the number of voids with an effective radius $r_{\rm v}$ falling within a set of size bins. In the upper panels of Figure 3.2 we show the differential size distribution at three different redshifts ($z = \{0, 0.55, 1\}$, from left to right) for the two cosmological models (black solid lines for ΛCDM and blue dashed lines for EXP003), while in the bottom panels we show the relative difference with respect to the reference ΛCDM cosmology (in units of its statistical error σ). As one can see in the figure, at $z = 0$ the number of voids in the cDE cosmology with $r_{\rm v} \gtrsim 20\ h^{-1}\,{\rm Mpc}$ is at least 50% larger than in ΛCDM: this difference corresponds to more than 4σ. At $z = 0.55$ the same ratio applies to cosmic voids with $r_{\rm v} \gtrsim 15\ h^{-1}\,{\rm Mpc}$, and at $z = 1$ to cosmic voids with $r_{\rm v} \gtrsim 12\ h^{-1}\,{\rm Mpc}$, with differences corresponding to 5σ and 7σ, respectively. Therefore, also in this statistic the two models are clearly distinguishable from each other.

Averaged density profiles

As a third statistic of our voids samples, we investigate the average stacked density profiles of voids having a comparable size. Many recent works [e.g. 92, 174, 175] suggested that the average profile of

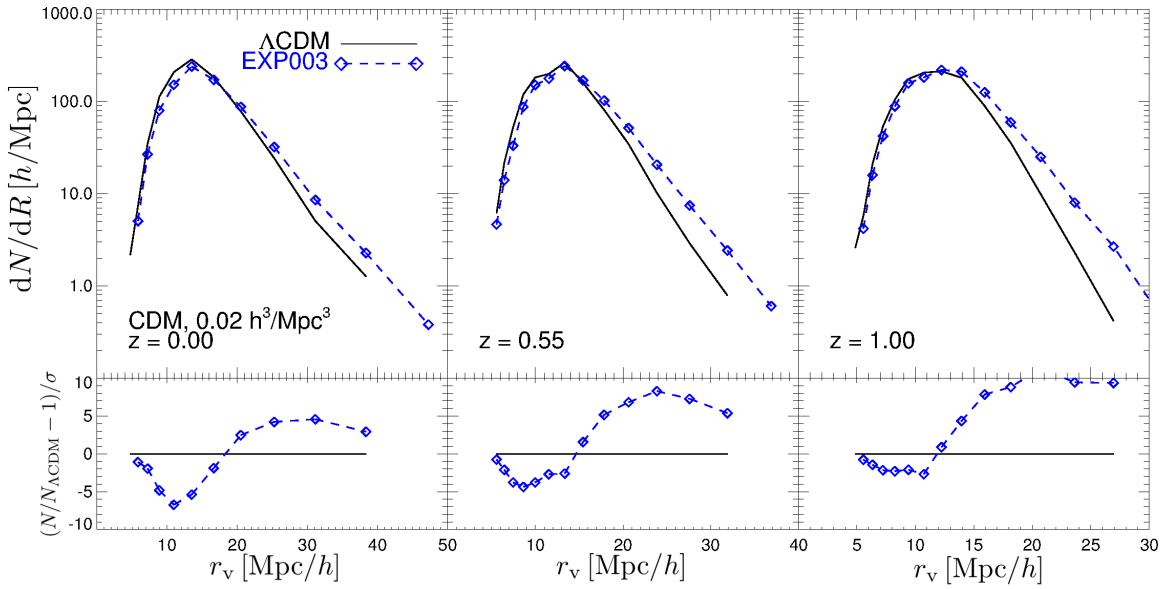

Figure 3.2: Top panels: the size distribution of voids in the CDM distribution for the ΛCDM (black solid line) and EXP003 (blue dashed lines) models. Bottom panels: the relative differences between the two models in units of the standard deviation σ, computed for the ΛCDM model.

voids is self-similar in the standard ΛCDM cosmology, which makes voids an ideal target for geometrical tests such as the AP test. Therefore, we now aim at investigating whether the interaction between DE and CDM particles might induce some additional features on the density profile of voids.

To this end, we first compute the spherically-averaged radial density profile of each individual void by estimating the CDM density within a series of logarithmically equispaced spherical shells centred in the barycentre of each void and normalised to the void effective radius r_v. The profiles are then stacked for voids with similar r_v. Since the profiles of each void is calculated in units of r_v in the first place, the stacking procedure basically consists in the calculation of the mean profile in each logarithmic radial bin. We randomly included 100 voids for each bin. The results are presented in Figure 3.3, where we show the comparison of the stacked density profiles obtained using the CDM void catalogue in the standard ΛCDM cosmology and in the EXP003 model. In the upper panels the error bars represent the corrected sample standard deviation computed on the 100 randomly selected voids. The shape of the profiles is qualitatively the same as found in previous works [92, 174, 175]: we observe a deep underdensity at $r \to 0$ and a compensative overdensity at $r \to r_v$. At $r > 1.5 \cdot r_v$ the profiles reach the mean density of the Universe. In the lower panels, we plot the relative difference between the models in units of the statistical significance σ computed as the sample standard

deviation propagated to the relative difference. The grey shaded area represents a $\pm 1\sigma$ significance.

As the figure clearly shows, the stacked profiles of EXP003 do not show significative differences from ΛCDM at the considered redshifts, with deviations always lying well within the mean square error. Nonetheless, we can observe that, at $r \to 0$, EXP003 generally shows a density $10 - 25\%$ smaller than ΛCDM, thereby showing that voids are *emptier* in cDE. Therefore, although with a low statistical significance, the central regions of the main voids appear to be more underdense in cDE models than in ΛCDM, which is expected to result in a corresponding stronger signal in void lensing surveys.

3.4.2 *Void statistics in the halo distribution*

We will now compute the same three void-statistics discussed in Section 3.4.1 for the voids catalogues obtained by running VIDE on the distribution of FoF haloes extracted from the CoDECS simulations at the same three redshifts investigated before (i.e. $z = \{0, 0.55, 1\}$). The use of the FoF haloes as tracers of the matter distribution has the appealing property to mimic real observations, where voids are identified in the distribution of luminous galaxies. In particular, we have made use of the publicly available CoDECS halo catalogues that have been obtained through a FoF algorithm with a linking length 0.2 times the mean inter-particle separation. As we will show below, the differences between the cDE model EXP003 and the standard ΛCDM cosmology in all the three statistics are much weaker than what previously found for the CDM distribution. For this reason, we will include in this comparison also other two cDE models available within the CoDECS suite, namely the EXP008e3 and the SUGRA003 models (introduced in Section 3.2.2), in order to verify whether different realisations of the cDE scenario might have a stronger impact on the voids defined by the FoF halo distribution than the EXP003 model. Our comparison will show that this is actually not the case, as expected from the fact that EXP003 is the most extreme of the CoDECS models in terms of background and linear deviations from ΛCDM.

Filling factor of voids traced in haloes

First of all, in Fig. 3.4 we compare the void filling factor for these new void catalogues, as already done in Fig. 3.1 for the voids in the CDM distribution. The void volume and the dispersion indicated by the grey shaded area are computed as outlined above. The figure shows, as expected, that the void volume fraction increases in time, and that the ΛCDM model has generally the lowest volume fraction with respect to the other cDE models that are characterised by a higher normalisation of the linear power spectrum. Nonetheless, as the figure clearly shows, these differences are now much smaller and lie within the 3σ statistical dispersion so that no significant differences in the voids filling factor appear among the various cDE

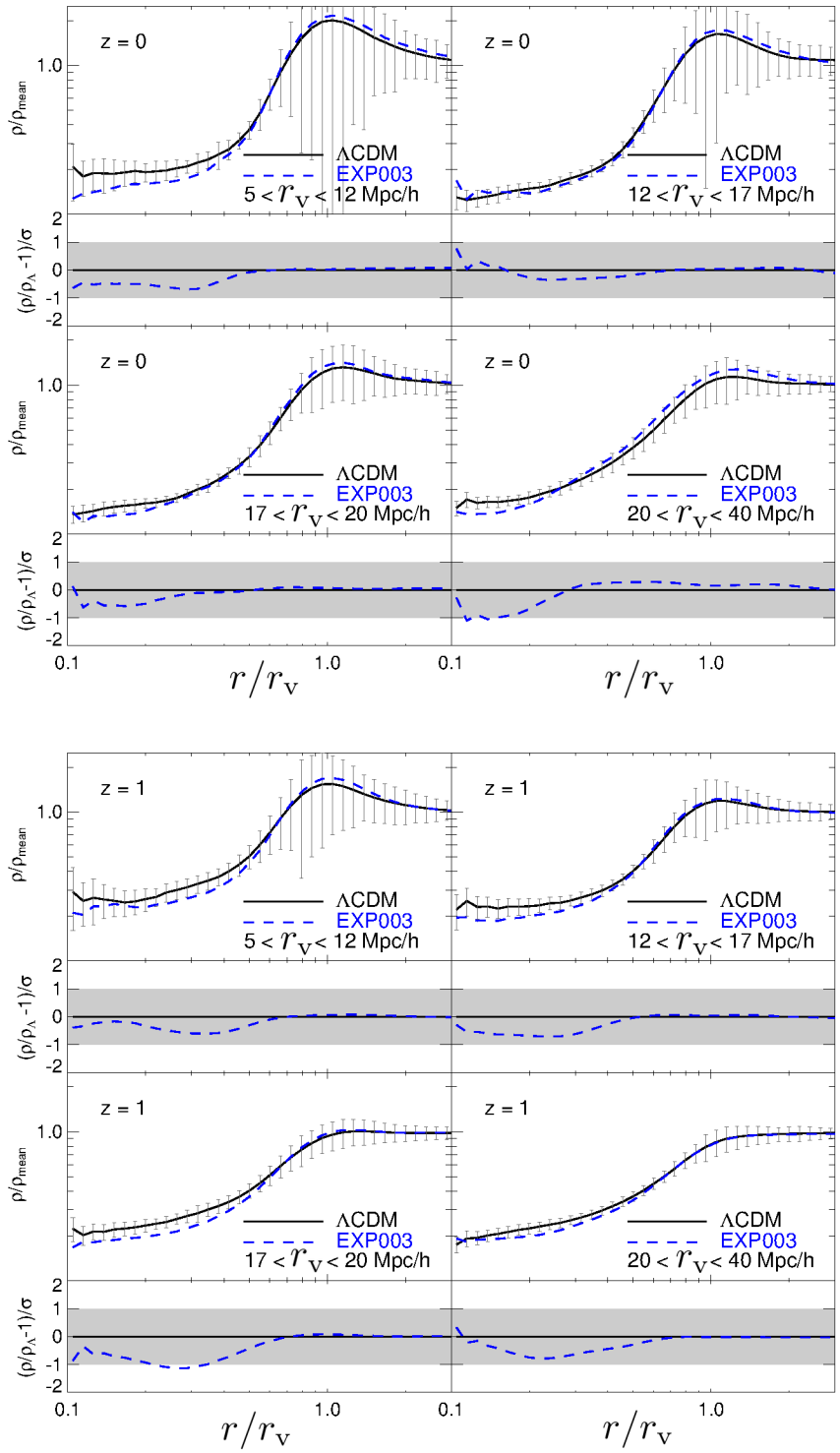

Figure 3.3: The stacked profiles of voids in the CDM distribution for the ΛCDM (black solid lines) and EXP003 (blue dashed lines) models. Results are displayed at two different redshifts, $z = 0$ and $z = 1$ (top and bottom blocks of panels, respectively) for four ranges of r_v, as labeled. The error bars indicate the corrected sample standard deviation in each radial bin computed on the 100 randomly selected voids, while the sub-panels display the relative difference between the profiles in units of the statistical significance of the averaged profile.

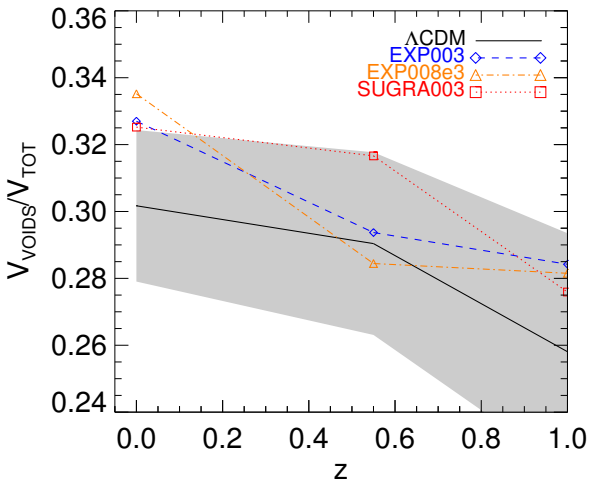

Figure 3.4: The redshift evolution of the volume fraction of voids identified in the halo distribution for different cosmological models: ΛCDM (black solid line), EXP003 (blue dashed line), EXP008e3 (dot-dashed orange line), SUGRA003 (red dotted line). The shaded area (shown only for ΛCDM) represents the uncertainty, computed with the jackknife method.

models and the standard ΛCDM cosmology at all redshifts. This result is starkly different from what found for the voids traced in the CDM distribution for the EXP003 model.

The void-size function of halo-traced voids

In Figure 3.5 we then display the differential size distribution for voids identified in the distribution of FoF haloes, analogously to what done in Figure 3.2 for the CDM distribution. The size distribution is shown for the different models (ΛCDM by black solid line, EXP003 by blue dashed line, EXP008e3 by orange dot-dashed line and SUGRA003 by red dotted line) in the upper panels, while the bottom panels report the percent deviation in units of the statistical significance σ from the reference ΛCDM case. While at $z = 0$ and $z = 0.55$ no significant differences appear among the models, one can observe an excess of small voids for the EXP003 model at $z = 1$. At this redshifts EXP003 shows $\sim 50\%$ more voids with $r_v < 30\ h^{-1}\,\mathrm{Mpc}$ than ΛCDM, although within a confidence of 1σ.

This is again a very different result with respect to what previously found for the voids identified in the CDM distribution, where the largest differences with respect to the standard cosmological model appeared at the large size tail of the distribution. It should however be noticed that due to the different density of the tracers between the sub-sampled CDM distribution adopted in the previous Section and the FoF halo distribution shown here, the mean separation between particles and hence the average size of voids is different in the two cases. Therefore, the size range that appeared as the large-size tail for the CDM voids ($20 < r_v[h^{-1}\,\mathrm{Mpc}] < 30$) is now representing

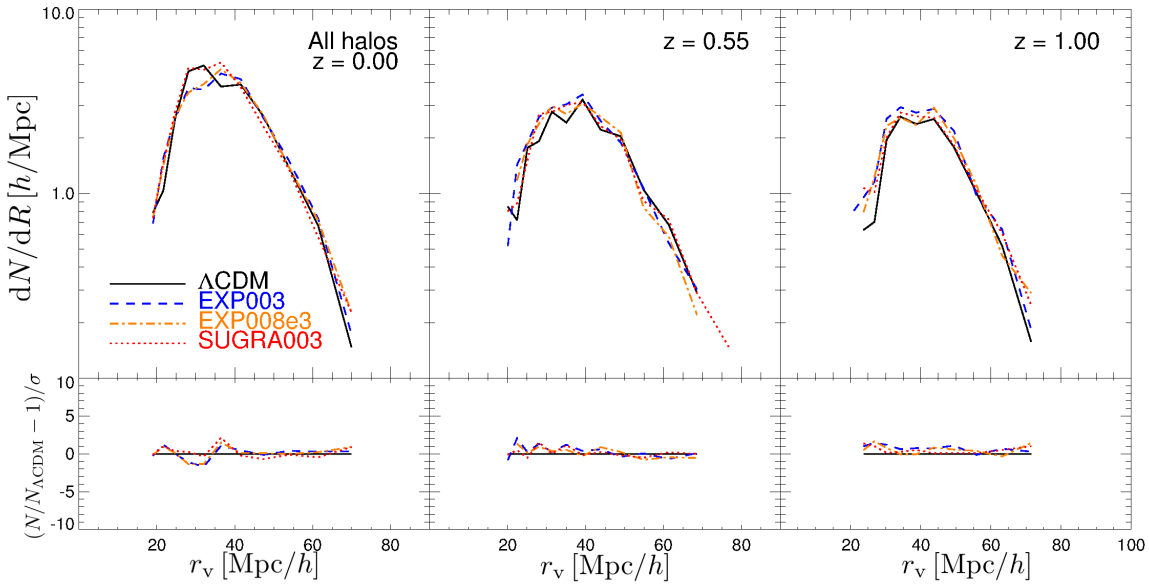

Figure 3.5: Top panels: the size distribution of voids in the halo distribution for the ΛCDM (black solid line), EXP003 (blue dashed lines), EXP008e3 (orange dot-dashed lines) and SUGRA003 (red dotted lines) models. Bottom panels: the relative differences between the cDE models and the ΛCDM one, in units of the standard deviation σ, computed for the ΛCDM model.

the small-size part of the void samples of the FoF halo distribution. For this reason, the two results might still appear consistent with each other despite their different qualitative trends. To address this issue, in Section 3.4.3 below we will compare the differential size distribution of voids identified in a different random sub-sample of the CDM particles distribution with the same density of tracers as the FoF halo catalogue. Nonetheless, the clear differences between the background evolution of ΛCDM and cDE models (see Figure 3.2) are not expected to be detected and do not appear for voids in haloes.

Before moving to this additional comparison, we conclude our analysis of the voids extracted from the FoF halo distribution by comparing the void stacked density profiles as we did in Figure 3.3 for the voids in the CDM distribution. In Figure 3.6 we show the analogous to Figure 3.3 for these new voids samples at $z = 0$ and $z = 1$.

Averaged density profile of voids traced in the halo sample

For both redshifts we do observe significative deviations from the ΛCDM profile only in the inner part of the voids, where shot noise can strongly affect the profiles. We also observe that the over-compensative region around $\sim 1 r_\mathrm{v}$ is not as prominent as in the CDM voids (see Figure 3.3), once again showing differences between tracers of density.

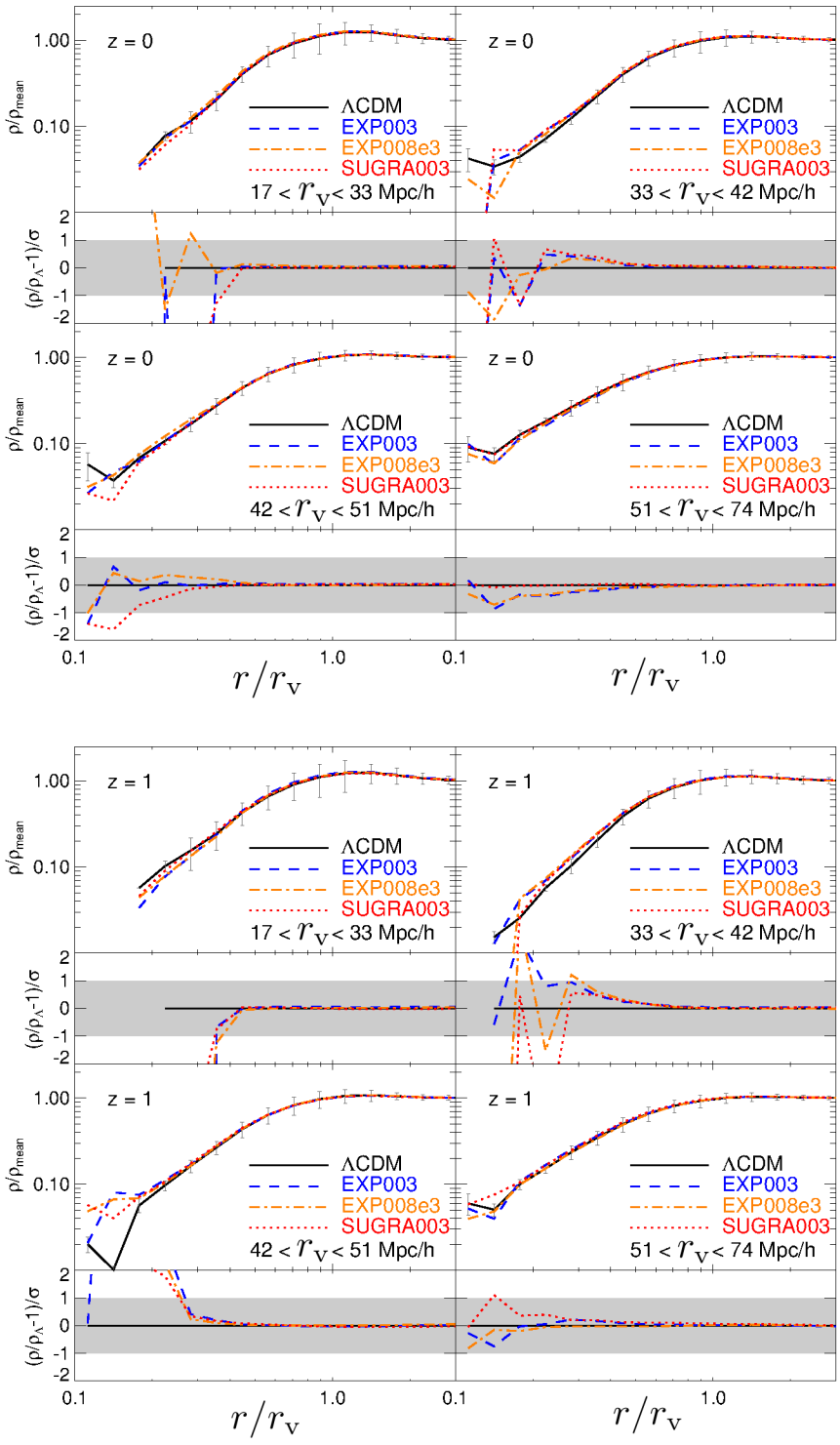

Figure 3.6: The stacked profiles of voids in the halo distribution for the ΛCDM (black solid lines), EXP003 (blue dashed lines), EXP008e3 (orange dot-dashed lines) and SUGRA003 (red dotted lines) models. Results are displayed at two different redshifts, $z = 0$ and $z = 1$ (top and bottom blocks of panels, respectively) for four ranges of r_v, as labeled. The error bars in the upper panels are computed as for Figure 3.3, and the sub-panels display again the relative difference of the profiles with respect to the ΛCDM one in units of the statistical significance of the averaged profile.

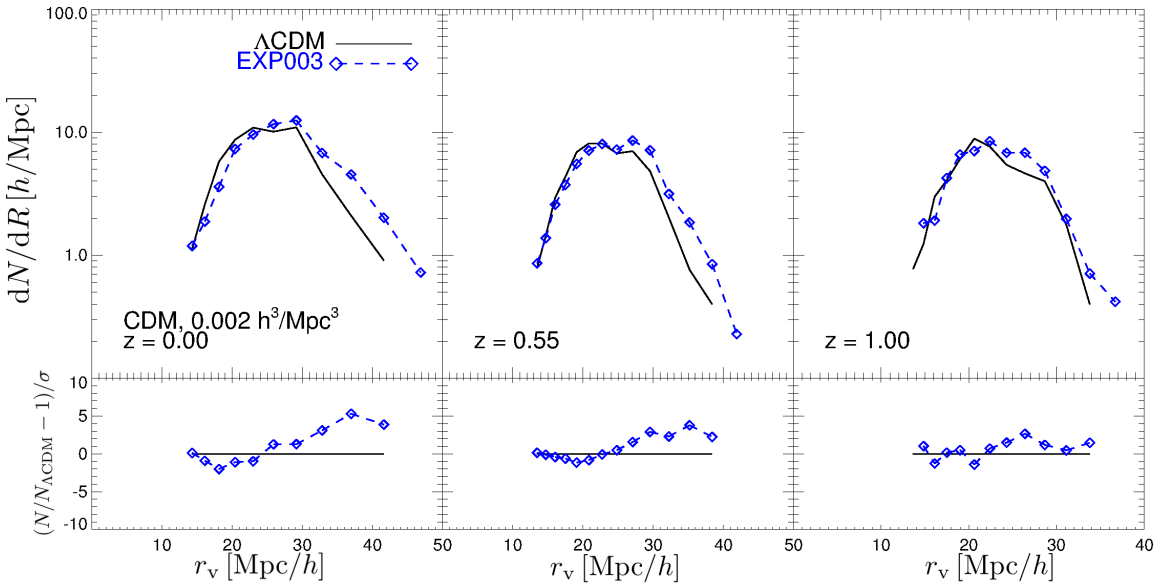

Figure 3.7: Top panels: the size distribution of voids in the CDM distribution diluted to the same density of the halo catalogue, for the ΛCDM (black solid lines) and EXP003 (blue dashed lines) models. Bottom panels: the relative differences between the two models, in units of the standard deviation, σ, computed for the ΛCDM model.

3.4.3 *The impact of halo bias*

As introduced in Section 3.4.2, it is interesting to compare the abundance of voids as a function of their effective radius, r_v, for voids samples extracted from the FoF halo catalogues and from a random sub-sampling of the CDM distribution having the same number of tracers in the simulation box as the number of FoF haloes. This will ensure that the mean inter-particle separation of the two samples of tracers is the same such that the corresponding average size of voids will be comparable in the two cases, thereby allowing for a direct comparison of the statistical properties of the two voids catalogues over a similar range of void sizes. This approach has been followed in several recent works [see e.g. 92, 156, 209], where the discriminating power of voids in future galaxy surveys has been inferred from the expected properties of voids identified in a random sub-sample of a simulated CDM distribution having the same density of the survey under investigation. To this end, we have randomly sub-sampled the CDM distribution of the CoDECS snapshots at the relevant redshifts to a total number of $1.5 \cdot 10^6$ particles, corresponding to the total number of objects in the FoF halo catalogue of the ΛCDM simulation at $z = 0$.

In Figure 3.7 we show the equivalent to Figure 3.2 for this new random sub-sampling and compare the abundance of voids in the ΛCDM and EXP003 models. We observe that, although the range of void sizes is now comparable to what was shown in Figure 3.5, the

A test to isolate the bias impact from sparse sampling

	ΛCDM			EXP003		
z	b	σ_8	$b \cdot \sigma_8$	b	σ_8	$b \cdot \sigma_8$
0.00	1.2	0.809	0.971	1.046	0.967	1.011
0.55	1.584	0.618	0.979	1.310	0.733	0.960
1.00	2.049	0.504	1.033	1.633	0.595	0.972
1.60	2.903	0.398	1.155	2.235	0.468	1.046
2.00	3.630	0.348	1.263	2.739	0.408	1.118

Table 3.2: The bias $b(z)$ and the normalisation of the linear perturbations amplitude $\sigma_8(z)$ for the ΛCDM and EXP003 cosmologies. The rightmost column for each model displays the combination $b(z) \cdot \sigma_8(z)$, showing how this combination is much similar for the two models as compared to σ_8 alone. As a consequence, the differences in the void populations extracted from the biased tracers within the two scenarios are significantly suppressed with respect to the case of the voids in the CDM distribution.

comparison between ΛCDM and EXP003 still appears starkly different in the two cases. Also in this case, as already shown for a denser sample of CDM tracers, the EXP003 scenario includes a larger number of voids of large sizes at all redshifts with respect to the standard ΛCDM cosmology, with a qualitatively different trend with respect to what shown in Figure 3.5. The comparison of Figs. 3.5 and 3.7 clearly indicates that voids in the CDM distribution and voids in the distribution of haloes are characterised by different statistical properties. As the density of the two tracers is the same, these different properties must be associated with the different bias of the two samples with respect to the underlying true density field: while a random subsampling of the CDM distribution is an unbiased tracer of the density field, haloes are biased and the bias is expected to evolve differently in cDE models than in ΛCDM [128, 134]. More quantitatively, the lower bias of the EXP003 model compensates for the higher value of the perturbations amplitude. A degeneracy between bias and σ_8In Table 3.2 we display the value of the bias [as computed in 128] and of σ_8 at various redshifts for the two models. As one can see from the last column, the combination $b(z) \cdot \sigma_8(z)$ is substantially closer between the two models compared to the value of σ_8 alone. This result suggests that the assumption (implicitly adopted in many recent works) that the properties of voids in a sub-sampled set of CDM particles extracted from a cosmological simulation can faithfully reproduce the statistics of voids identified in a galaxy survey is not valid.

In order to further validate this result, we compute the size distribution of voids identified in the distribution of FoF haloes with masses $M > 5 \cdot 10^{12} M_\odot$, thus considering tracers with larger masses and, therefore, with higher bias. This comparison is shown in the upper

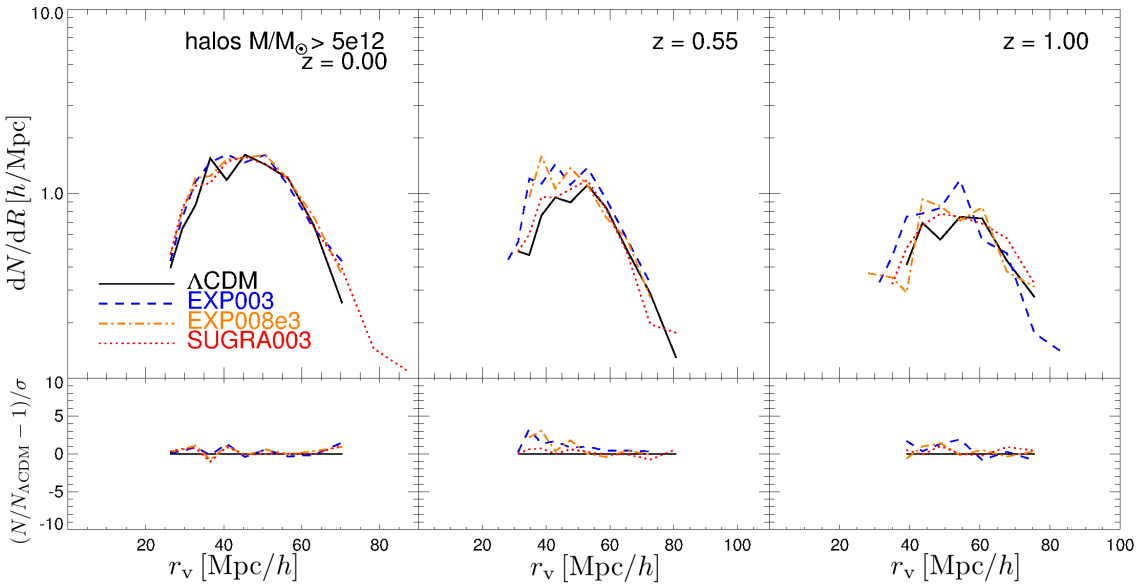

Figure 3.8: Top panels: the size distribution of voids identified in the distribution of haloes with mass $M > 5 \cdot 10^{12} M_\odot$, for the ΛCDM (black solid lines), EXP003 (blue dashed lines), EXP008e3 (orange dot-dashed lines) and SUGRA003 (red dotted lines) models. Bottom panels: the relative differences between the cDE models and the ΛCDM one, in units of the standard deviation σ, computed for the ΛCDM model.

panels of Figure 3.8, while the bottom panels display the deviation (in units of σ) between the models. At $z = 0$ we do not observe any significative difference between models (in agreement with Figure 3.5), while at larger redshifts we find that the EXP003 cDE model features a larger number of small voids ($30 < r_\mathrm{v}[h^{-1}\,\mathrm{Mpc}] < 60$) as compared to ΛCDM, though the effect is small. The comparison between Figs. 3.2 and 3.8 indicates again that voids in the CDM distribution and in the distribution of haloes are characterised by different statistical properties. This result clearly shows that the bias of the tracers from which voids are identified has a non-trivial impact on the relative statistical properties of the voids sample between two competing cosmological scenarios. Therefore, when comparing voids in ΛCDM and cDE models, voids in haloes (which are biased tracers of the underlying density field) will not provide a faithful representation of how the models might differ in the properties of voids in the CDM distribution.

3.5 SUMMARY, DISCUSSION AND CONCLUSION

In this Chapter we analysed the statistical properties of voids in ΛCDM and cDE models. In particular, we compared the properties of voids detected in the distribution of CDM and in collapsed haloes, by means of a suite of large cosmological simulations, the CoDECS. We focused

Summary of the results of this Chapter

on three void statistics: the filling factor, the size distribution and the stacked density profiles.

In Section 3.4.1 we investigate the properties of voids in the CDM distribution, considering the ΛCDM and the cDE model EXP003, which represents – among the available CoDECS models – the most extreme case showing the largest discrepancies with respect to ΛCDM in several other observables [see e.g. the results of 13, 25, 40, 56, 85, 86, 118, 128, 134, 146]. Our main results can be summarised as follows.

1. The filling factor of voids detected in the CDM distribution in the EXP003 model is significantly larger than in the ΛCDM case, as expected due to the higher normalization of the amplitude of linear perturbations at low redshift (Fig. 3.1). More quantitatively, the volume fraction in EXP003 is $\sim 40\%$ larger than the corresponding ΛCDM fraction: based on a jackknife approach, this is detectable with a very high statistical significance.

2. For what concerns the differential size distribution (Figure 3.2), we found an excess of large voids in the EXP003 model with respect to the reference ΛCDM cosmology, consistently with the general findings of Pisani et al. [156]. Quantitatively, the excess is around 50% with a difference larger than 4σ. The radius at which this excess starts to be significant decreases with redshift, being $r \sim 20, 15, 12\ h^{-1}\,\mathrm{Mpc}$ at $z = 0, 0.55, 1$, respectively.

3. The shape of the stacked density profile (Figure 3.3) is qualitatively similar to what previously found in the literature (i.e density minima around the centres of the voids and over-dense compensation regions at $r \sim r_\mathrm{v}$). The void profiles in cDE models are not significantly different from what observed in the standard cosmology. Nonetheless, we can observe that close to the voids centres, the EXP003 model generally displays a density $10 - 25\%$ smaller than ΛCDM, thus showing that voids tend to be *emptier* in cDE models. On the other hand, the compensative over-density at $r \sim r_\mathrm{v}$ in the EXP003 case looks more prominent than in ΛCDM. All of these features are expected considering that the evolution of the background perturbations in cDE scenarios is faster than ΛCDM due to the *fifth force* associated with the coupling.

In Section 3.4.2 we then focused on voids identified in the halo distribution, finding that the comparison between cDE models and the reference cosmology is very different from what found for CDM. More specifically, we find the following results:

1. The filling factor of voids in haloes is not strongly dependent on the considered cDE model (Fig. 3.4). Only minor, not significant differences are found in the volume fractions at all redshifts considered in this analyses. This last result is starkly different from

what observed in void samples detected in the CDM distribution.

2. The comparison of differential size distribution (Figure 3.5) in the halo distribution does not reveal sensible differences between cDE models and the reference one. This result is again substantially different from what found in Section 3.4.1. We connect this discrepancy with the impact of the halo bias on void properties. To test such effect, we compare size distribution of voids in a random sub-sample of the CDM distribution with the same density of tracers as the FoF halo catalogue. Again, in this last case voids in CDM do not show the same relative trend in the differential size distribution as for the voids in the halo distribution (Figure 3.7). The impact of the halo bias can be observed also by increasing the minimum mass of haloes used as tracers: in Figure 3.8 we show that including only haloes with large masses ($> 5 \cdot 10^{12} \cdot M_{\odot}$) the cDE models show an excess of voids with $30 < r_{\rm v}[h^{-1}\,{\rm Mpc}] < 60$ at $z = 0.55, 1$, which is not seen in Figure 3.5.

3. The density profile of voids in haloes does not look like an effective probe to discriminate among cDE models. Indeed, as shown in Figure 3.6, the stacked profiles of voids in cDE models are only marginally distinguishable from the ΛCDM case, and only in the very innermost parts.

To conclude, the main result of this Chapter is that the properties of voids in different cosmological models are strongly affected by the choice of the tracers of the underlying density field used to detect them (haloes or CDM particles). This is caused by the impact of the halo bias on the structural properties of voids: as the bias evolves differently for different cDE models, this is reflected in a non-trivial way on the properties of the associated void sample.

Our results indirectly challenge the assumption made in several recent works that a sub-sampled distribution of simulated CDM particles with the same density of the expected tracers of a real galaxy survey might provide reliable predictions about the effective discriminating power of voids in that survey.

In the next Chapter we will try to address this issue more closely in the ΛCDM scenario.

4

ON THE LINEARITY OF TRACER BIAS AROUND VOIDS

The analysis presented in this Chapter has been developed in collaboration with Nico Hamaus, Klaus Dolag, Jochen Weller, Marco Baldi and Lauro Moscardini. Its results are published in an article [165].

A summary of this Chapter

The large-scale structure of the universe can only be observed via luminous tracers of the dark matter. However, the clustering statistics of tracers are biased and depend on various properties, such as their host-halo mass and assembly history. On very large scales this tracer bias results in a constant offset in the clustering amplitude, known as *linear bias*. Towards smaller non-linear scales, this is no longer the case and tracer bias becomes a complicated function of scale and time. We focus on tracer bias centred on cosmic voids, depressions of the density field that spatially dominate the universe. We consider three types of tracers: galaxies, galaxy clusters and AGN, extracted from the hydrodynamical simulation MAGNETICUM *Pathfinder*. In contrast to common clustering statistics that focus on auto-correlations of tracers, we find that void-tracer cross-correlations are successfully described by a linear-bias relation. The tracer-density profile of voids can thus be related to their matter-density profile by a single number. We show that it coincides with the linear tracer bias extracted from the large-scale auto-correlation function and expectations from theory, if sufficiently large voids are considered. For smaller voids we observe a shift towards higher values. This has important consequences on cosmological parameter inference, as the problem of unknown tracer bias is alleviated up to a constant number. The smallest scales in existing datasets become accessible to simpler models, providing numerous modes of the density field that have been disregarded so far, but may help to further reduce statistical errors in constraining cosmology.

Chapter's organization

This Chapter is organized as follows: in Section 4.1 we provide a short introduction to the specific analysis presented, in Section 4.1.1 we describe the simulations employed in this analyses, in Section 4.2 we present the commonly used bias estimators in observations and theory and discuss the void-finder we employ, in Section 4.3 we explain how we conducted our analysis and in Section 5.5 we recap all of our result and draw our conclusions.

4.1 SUMMARY OF THE RELEVANT STATE-OF-THE-ART

As revised in Chapter 2, in the present standard cosmological model the large-scale structure of the Universe forms in a hierarchical process that begins with the gravitational collapse of over-dense fluctuations of the matter density field into virialised and gravitationally bound objects, known as dark matter haloes. Such objects provide the potential wells in which baryons can cool and condense to create galaxies that are now observed in the sky [151]. The understanding of modern cosmology and structure formation is thereby deeply connected to the statistical properties of dark matter haloes and their hosted galaxies, which represent the final stage of the evolution of primordial fluctuations and can be directly observed and used to constrain theory. Studying the clustering properties of galaxies, it was discovered that they do not precisely mirror the clustering of the bulk of the dark matter distribution: such evidence brought Kaiser [106] to introduce the concept of galaxy bias to indicate that galaxies are biased tracers of the underlying matter density field, as reviewed in Section 2.3.3. Bias is now a known property of luminous tracers on very large scales, where density fluctuations are within the linear regime: in this case tracer bias is a simple constant offset in the clustering amplitude, known as *linear bias*. Towards small scales, this elementary relation does not stand and bias becomes an unestablished function of scale and time.

In this Chapter we focus on the bias of tracers inside and around cosmic voids, large under-dense regions in the large-scale structure of the Universe that together with clusters, filaments and walls define the topology of the cosmic web as predicted in a cold dark matter cosmology [29, 163]. Voids are another peculiarity of the large scale structure of the Universe, representing the result of the evolution of under-densities in the primordial density field.

The growing interest for cosmic voids in the literature is partly due to their not yet fully explored potential to constrain cosmology, while the known properties of voids suggest they are very promising cosmological probes (see discussion in Section 3.1 and reference therein).

How to relate void in theory, simulations and observations?

Despite that, a lack of understanding in how to link void properties to theory, simulations and observations persists. For what concerns the theoretical comprehension of voids, one of the pioneering works in the field is presented in Sheth and van de Weygaert [191], where the authors provide a theory to model the void-size distribution and its evolution assuming spherical initial conditions, as commonly done in void evolution models [27, 151, and see Sections 2.2.2 and 2.3.2 for a summary of these topics]. However, assuming voids to start evolving from spherical under-densities might not be representative of objects developing from Gaussian underdense fluctuations of arbitrary shape. The number function of voids identified in cosmological simulations

is in fact not well represented by the model proposed by Sheth and van de Weygaert [191], as recently argued (see e.g [75, 105, 136]; but see [157] for how to take this into account). Many studies have been conducted to better understand the evolution of voids over cosmic time [3, 61, 221] and their number function [169].

Similarly, another gap that still has to be bridged concerns the relation between the properties of voids in simulations with potentially observable voids. Numerous catalogues of voids identified in spectroscopic data are now available [see e.g. 45, 127, 140, 149, 205] and recently the largest galaxy survey to date, the Dark Energy Survey (DES), has detected a trough and void lensing signal in a photometric survey of galaxies [89, 185], opening up new possibilities to exploiting the potential of voids in observations. In the future the next generation of large galaxy surveys, such as the ESA Euclid mission [8, 116], are expected to provide a tremendous amount of new information concerning the large-scale structure of the Universe. The detection of gravitational lensing from medium-size voids in these surveys will possibly constrain the void density profiles without having to rely on luminous tracers like galaxies, which would require to model their bias [50, 104, 114, 132]. Nevertheless, the vast majority of available void-finders [see e.g. 141, 147, 161, 210] rely on the position of dark matter particles in simulations, which cannot be directly compared to observables. The same finders can be adapted to use galaxies as tracers but one will eventually need to model the tracer bias to compare observational results with predictions from simulations and to fully understand properties of voids in the dark matter. For example, several recent works study how redshift-space distortions around void-centres provide constraints on cosmological parameters [4, 38, 48, 95, 96, 99]: all of these analyses are based on the assumption that bias is linear in void environments. Nonetheless, a detailed study to investigate and validate this assumption is still missing.

With the analyses presented in this Chapter, we aim to directly determine the relation between luminous tracers of the large-scale structure (such as galaxies, clusters and AGN) and their underlying matter distribution in voids to directly test the linear bias assumption. Thanks to state-of-the-art simulations that feature a full hydrodynamical treatment, the so-called MAGNETICUM *Pathfinder* simulations [Dolag et al. in prep; see also 63, 100, 172, 186, 212], we are able to perform this test with very high accuracy. The general idea is to run a void finder on samples of luminous objects and to extract both the distribution of luminous tracers and matter around void-centres, in order to compare them against each other.

4.1.1 *Simulations*

The hydrodynamical simulation suite MAGNETICUM *pathfinder*[1] (Dolag et al, in prep.) has already been employed successfully in a wide number of numerical studies. MAGNETICUM showed so far a remarkably good agreement with observations for various probes, such as for the pressure profiles of the intra-cluster medium [130, 158], the expected Sunyaev Zeldovich signal [63], the imprint of the intergalactic medium onto the dispersion signal of Fast Radio Bursts [66], various characteristics of AGN populations [100, 202, 203], the dynamical features of massive spheroidal galaxies [172, 173], and the angular momentum signatures of galaxies [212].

Cosmology, box size, number particles

In this Chapter we employ the largest cosmological volume simulated within that project, it covers a box of side length $2688h^{-1}$ Mpc, simulated using 2×4536^3 particles [for details, see 28]. We adopted a WMAP7 [110] ΛCDM cosmology with $\sigma_8 = 0.809$, $h = 0.704$, $\Omega_\Lambda = 0.728$, $\Omega_m = 0.272$, $\Omega_b = 0.0456$, and an initial slope for the power spectrum of $n_s = 0.963$. The simulation is based on P-GADGET3 [197], a parallel cosmological tree Particle-Mesh (PM) Smoothed-Particle Hydrodynamics (SPH) code. It uses an entropy-conserving formulation of SPH [198] and follows the gas using a low-viscosity SPH scheme to properly track turbulence [64].

Halo definition

Halos and sub-haloes are identified using the SUBFIND algorithm [65, 199]. SUBFIND identifies sub-structures as locally overdense, gravitationally bound groups of particles, starting from a main halo which is identified through the Friends-of-Friends (FoF) algorithm with a linking length of 0.16 times the mean inter-particle separation. After this first step a local density is estimated for each particle via adaptive kernel estimation, making use of a prescribed number of smoothing neighbours. After isolated density peaks are identified, additional particles of decreasing density are added. When a saddle point that connects two disjoint overdense regions in the global density field is reached, the smaller structure between the two is treated as a sub-structure candidate, and the two overdensities are then merged. An iterative unbinding procedure with a tree-based calculation of the potential is then run on all sub-structure candidates. These structures are finally associated with galaxies, and their integrated properties (such as stellar mass, M_*) are computed. Galaxies in MAGNETICUM can have stellar masses as low as $4 \times 10^8 h^{-1} M_\odot$, but in this study we will consider as main sample only galaxies with $M_* \geq 10^{11} h^{-1} M_\odot$, which are more realistically observable.

The virial radius of the main haloes identified by the FoF algorithm is calculated using a density contrast built on the top-hat model [72]. To allow a better comparison with observations, we additionally use an overdensity with respect to 500 times the critical density to define

1 http://www.magneticum.org

Table 4.1: Properties of the galaxy, cluster and AGN populations extracted from the MAGNETICUM simulations. We report the minimum mass of the object included, $M_{\rm min}$, in terms of stellar masses M_* for the galaxies, M_{500c} for clusters and $M_{\rm BH}$ for AGNs, as well as the number of tracers N_t and of identified voids $N_{\rm v}$

Tracers	$M_{\rm min}[M_\odot/h]$	N_t	$N_{\rm v}$
Galaxies	$M_* = 4 \times 10^8$	9.5×10^6	36430
Clusters	$M_{500c} = 1 \times 10^{13}$	2.6×10^6	16970
	$M_{500c} = 5 \times 10^{13}$	3.5×10^5	3125
	$M_{500c} = 1 \times 10^{14}$	1.0×10^5	1053
AGNs	$M_{\rm BH} = 4 \times 10^6$	5.3×10^6	26265

M_{500c}, which is the mass we will refer to as cluster mass in this and in the next Chapter. Clusters are identified as main haloes with $M_{500c} > 10^{13} h^{-1} M_\odot$. For our analysis we make use of the galaxy and cluster samples extracted from the simulation at redshift $z = 0.14$ with the criteria explained above. In Table 4.1 we summarise some properties of the tracers relevant for this analysis.

4.2 METHODOLOGY

In this Section we will briefly recap how the tracer bias is defined in observations and theory. We will also present some properties of void profiles that are relevant for this analysis. This section is mostly written for the benefit of the reader interested only in the present Chapter, as most of the topic are presented with more details in Section 2.3.

4.2.1 *Correlation functions and bias estimation*

The tracer correlation function is a measure of the degree of clustering of the tracer itself. Being d^2P the probability that a tracer A in the volume $\mathrm{d}V_A$ and another tracer B in the volume $\mathrm{d}V_B$ are separated by a distance r, the spatial two-point correlation function, $\xi_{AB}(r)$, is defined as the deviation of such probability from that expected from a random marginparThe correlation function: a brief recapdistribution of tracers:

$$\mathrm{d}^2P = \langle n_A \rangle \langle n_B \rangle [1 + \xi_{AB}(r)] \mathrm{d}V_A \mathrm{d}V_B \tag{4.2.1}$$

where $\langle n_A \rangle$ and $\langle n_A \rangle$ are the mean densities of the tracers [151]. When we compare tracers of the same population we refer to ξ as the auto-correlation function while, if we compare two kind of tracers, we refer to ξ as cross-correlation function.

In general there is no reason to assume that the distribution of baryons in the Universe traces exactly the distribution of mass. In fact, on small scales, galaxy formation involves many dissipative processes such as the radiative cooling of hot gas, so the efficiency of galaxy formation is related to how deep the potential wells created by haloes were; hence, on small scales, bias between matter and tracers is a complicated function of space and time. By looking the distribution of tracers on very large scales, we can only observe the most luminous galaxies which are hosted by the most massive haloes [106] i.e. by the highest peaks in the density-field. Thereby, in the latter regime, tracers still do not perfectly mirror the same distribution as matter, but, since the density fluctuations are small, the relation between matter and luminous tracers result in a constant offset in the clustering amplitude, the *linear bias*, which, in terms of spatial correlations, can be written as:

Linear bias

$$b = \xi_{tm}/\xi_{mm}\,, \tag{4.2.2}$$

or

$$b = \sqrt{\xi_{tt}/\xi_{mm}} \tag{4.2.3}$$

where ξ_{tm} is the tracer-matter cross-correlation function, ξ_{mm} is the matter auto-correlation function and ξ_{tt} is the tracer auto-correlation function (the tracers being galaxies, clusters and AGNs for our purposes). We make use of these two definitions to calculate the value of the linear bias of tracers in the MAGNETICUM simulation.

4.2.2 *Theoretical bias*

The excursion set formalism, introduced by Press and Schechter [167] to predict the number of virialized dark matter haloes in the Universe and fully developed by Bond et al. [30], provides a solid foundation to build a simple theoretical model to calculate the clustering of dark matter haloes and how their spatial distribution is biased with respect to that of the mass. As revisited in Section 2.3.3 with this approach, Mo and White [133] estimated the bias to be given by Equation 2.3.37), which, for convinience we report here. Mo and White [133] bias, $b_{\rm MW}$, is given by

$$b_{\rm MW} = 1 + \frac{\nu^2 - 1}{\delta_{\rm crit}}\,, \tag{4.2.4}$$

where $\delta_{\rm crit}$ is the critical density exceeding which the collapse occurs and $\nu \equiv \delta_{\rm crit}/\sigma(M)$ is the height of the threshold in units of the

variance of the smoothed density distribution, $\sigma(M)$, at a given halo mass, M:

$$\sigma^2(M) = \frac{1}{2\pi}\int_0^\infty dk k^2 P_m(k,z)\tilde{W}_R^2(k)\,, \tag{4.2.5}$$

$P_m(k,z)$ being the matter power spectrum at redshift z and $\tilde{W}_R(k)$ the Fourier transform of the top hat filter function [for a review of these topics we refer to 223].

However, the bias as expressed by Equation 4.2.4 fails to predict with high accuracy the value of the bias measured in numerical simulations. For this reason various corrections to Equation 4.2.4 have been proposed in order to improve the consistency with simulation results [see e.g. 187–190, 215]. In particular, Tinker et al. [215] shows how, by calibration with a large set of simulations, it is possible to estimate bias to great accuracy. Following the results of Tinker et al. [215], the linear bias $b_{\rm Tinker}$ reads as:

$$b_{\rm Tinker} = 1 - A\frac{\nu^a}{\nu^a + \delta_{\rm crit}^a} + B\nu^b + C\nu^c\,. \tag{4.2.6}$$

where a, A, b, B, c, C are the calibrated parameters.

We will compute the theoreatical value of the linear bias in the MAGNETICUM simulations using both the formula by Mo&White and its correction by Tinker. In order to calculate the theoretical mean value of the bias associated to our cluster sample we will average its value using the number of objects as function of their mass (the cluster mass function) $\frac{{\rm d}n}{{\rm d}M}$, i.e.:

$$\langle b\rangle = \frac{1}{\langle n_t\rangle}\int_{M_{\rm min}}^{M_{\rm max}}\frac{{\rm d}n}{{\rm d}M}b(M){\rm d}M\,, \tag{4.2.7}$$

where $M_{\rm min}$ and $M_{\rm max}$ are the lowest and largest masses in the sample, respectively.

4.2.3 *On void definition and void-finding*

Bias effects are independent of void-definition

The biggest criticism concerning void studies is generally related to the ambiguity of the void definition: there are in fact many different available finders and, in some circumstances, the usage of such a variety of recipes to identify voids can lead to results almost impossible to compare [53]. Although the void definition can be a serious obstacle on the way to establish a coherent picture on void properties, previous works proved that some statistical properties of voids (such as their number function or profile) are strongly affected by galaxy bias independently of the finder in use. In particular, recent papers exploiting the differences between voids in a ΛCDM cosmology and modifications of gravity [36], Galileon or non-local gravity

[21], or possible couplings between cold dark matter and dark energy [164] conclude that, while voids identified by matter particles exhibit a clear deviation from the ΛCDM case, it is impossible to discriminate between models looking at the statistics of voids identified by haloes. While Barreira et al. [21] connect the latter result with the poor statistic of the halo-sample, Cai, Padilla, and Li [36] suggest that this feature is related to the halo bias in agreement with Pollina et al. [164], where the authors verified that the poor statistic of haloes is not sufficient to justify the dissimilar properties displayed by voids in haloes and voids in matter. A similar conclusion has been drawn independently by Nadathur and Hotchkiss [137] using a ΛCDM simulation. It is a quite remarkable fact that all of these works reach the same conclusion using different void-finders, namely: an improved version of the finder presented in [147] (employed by [36]), the Watershed Void Finder algorithm ([162], used by [21]), VIDE ([210], utilised by [164]) and a modified version of ZOBOV ([141], employed by [137]). So, although it has been pointed out that a dynamical approach in void-finding (in which there is no reliance on particle positions) can reduce the impact of shot noise in void-identification [see e.g. 74], this is not relevant for the present study where we look directly at bias effects, which, as clarified above, are visible independently of the finder in use. That said, it is crucial to be as clear as possible in the description of the void finder and of a possible selection applied on top of the void catalogue to ensure that conclusions and results attained are plausible and can be reproduced by other parties.

We make use of the publicly available void finder VIDE [210, Void IDentification and Examination toolkit] to identify voids. VIDE is a wrapper for ZOBOV [ZOne 141, ZOnes Bordering On Voidness], an algorithm that identifies depressions in the density distribution of a set of points and merges them in voids with a watershed transform. Details on the functioning of the void finder are reported in Section 3.3.

Void selection

VIDE provides many catalogues in which various types of sample selections (as e.g. cuts on the void hierarchy or on the void central density) are applied on top of the original ZOBOV sample. Since for observations it is often undesirable to perform a selection on the void sample due to poor statistics, *we will apply no selection regarding void hierarchy or central density*, thereby allowing also voids-in-clouds (voids in overdense environment) in our analysis.

The ZOBOV code was originally intended for void-finding in simulations, but VIDE also provides a flag for void-identification in light cones from observations including the survey mask into the analysis [see the VIDE paper 210, for further information] and, in fact, several catalogues of voids in spectroscopic samples are already available [45, 127, 140, 149, 205]. Computationally we therefore have no problem in handling void-finding in observations. The issue left to address is

how to incorporate the bias into our framework, since we will need to relate properties of voids identified in the distribution of luminous tracers of the dark matter with voids in the dark matter distribution itself, that are usually under study in simulations. We will elucidate this relation in the following Sections of this Chapter.

4.2.4 *Density profile of cosmic voids*

The void density profile is one of the basic void statistics. From previous studies it is known that the spherically averaged profile of voids exhibits a very simple structure [see e.g. 92, 174, 175]: voids are deeply under-dense in the vicinity of their center and feature an over-dense compensation wall at $r \approx r_{\rm v}$, where r is the radial distance from the void center. Such a density profile can be described with a simple fitting formula [92]:

Self-similar void density profile and void-tracer correlation

$$\frac{n_{\rm vt}}{\langle n_t \rangle} - 1 = \delta_c \frac{1 - (r/r_s)^\alpha}{1 + (r/r_{\rm v})^\beta}\,, \tag{4.2.8}$$

where δ_c is the central density contrast, r_s is a scale radius at which the profile density, $n_{\rm vt}$, is equal to the average density of tracer $\langle n_t \rangle$; α and β describe the inner and outer slopes of the void profile.

It is possible to show that the density profile of voids encodes the same information as the void-tracer cross correlation function. In fact the radial profile of voids is nothing but a procedure by means of which we count tracers at a given distance from the void center per units of volume, i.e. the cross-correlation between centers and tracers by definition [see, e.g., 95]. N_t being the number of tracers, $N_{\rm v}$ the number of voids, δ^D Dirac's delta function, V the total volume, $\vec{x}_i^c$ the coordinates of the center of the $i-$th void, and $\vec{x}_j^t$ the coordinates of the $j-$th tracer we can show explicitly that the radial spherically averaged void tracer-density profile compared to the mean tracer density of the Universe, is:

$$\begin{aligned}
\frac{n_{\rm vt}(r)}{\langle n_t \rangle} =& \frac{1}{N_{\rm v}} \sum_i \frac{n^i_{\rm vt}(r)}{\langle n_t \rangle} = \\
& \frac{1}{N_{\rm v}} \sum_i \frac{1}{N_t} V \sum_j \delta^D(\vec{x}_i^c - \vec{x}_j^t + \vec{r}) = \\
& V \sum_{i,j} \int \frac{1}{N_{\rm v}} \delta^D(\vec{x}_i^c - \vec{x}) \frac{1}{N_t} \delta^D(\vec{x} - \vec{x}_j^t + \vec{r}) d^3x = \\
& \frac{1}{V} \int \frac{n_{\rm v}(\vec{x})}{\langle n_{\rm v} \rangle} \cdot \frac{n_t(\vec{x} + \vec{r})}{\langle n_t \rangle} d^3x = 1 + \xi_{\rm vt}(r)
\end{aligned}$$

thereby proving that:

$$\frac{n_{\rm vt}(r)}{\langle n_t \rangle} - 1 = \xi_{\rm vt}(r). \tag{4.2.9}$$

as we wanted to show.

4.3 THE STATISTICS OF VOIDS IN THE MAGNETICUM *pathfinder* SIMULATIONS

The aim of the analysis presented in this Chapter is to study the distribution of matter around potentially observable voids, i.e. voids identified in the distribution of luminous tracers, such as galaxies, clusters, or AGNs. The basic idea is to run our void-finder (described in Section 5.3.1) on the galaxy, cluster and AGN catalogues extracted from a large fully-hydro simulation (the MAGNETICUM see Section 4.1.1) and calculate both the density-profile of dark matter and of its tracers around voids. A similar study has been conducted by Sutter et al. [208], although the main purpose there was to show that voids in galaxies coincide with underdense regions of the dark matter distribution, which is indeed a crucial study to investigate potentially observable properties of voids. The authors also perform a void-to-void comparison for voids identified by galaxies and by matter particles. They conclude that it is always possible to identify a matter void in the vicinity of a galaxy void, although an offset between their centers is usually present. At that stage it has been concluded that potentially observable voids are indicative of the presence of an under-density of matter in our Universe. As we have now evidence that the tracer bias is playing a fundamental role in void-analysis (see the discussion at the beginning of Section 5.3.1), we need to further investigate the relation between tracers and the matter distribution around voids, which is the goal of the present analysis.

Comparison with a similar study

In the following, we will refer to galaxy-voids, cluster-voids or AGN-voids to indicate voids which are defined by applying the finder on the galaxy-sample, the cluster-sample or the AGN-sample. More generally we will refer to tracer-voids to indicate the three of them at the same time.

4.3.1 *Dark matter distribution around void centers*

To have a first overview of the void catalogues we are about to use, we look at the size distribution of voids which is displayed in This figure shows the number of voids as a function of r_v. Voids in MAGNETICUM have sizes between $15\,\mathrm{Mpc}/h$ and $150\,\mathrm{Mpc}/h$ (we refer to the largest volume simulated, where the box-size is $2688\,\mathrm{Mpc}/h$). As we could have expected due to the number of tracers available in each sample (see Table 4.1) and its effect on void-finding [see 207] we resolve the smallest voids in the galaxy sample, where we see twice as many voids of size within $15 - 60\,\mathrm{Mpc}/h$ as in the AGN-sample and four times as many as in the cluster sample.

Void-size functions of Magneticum

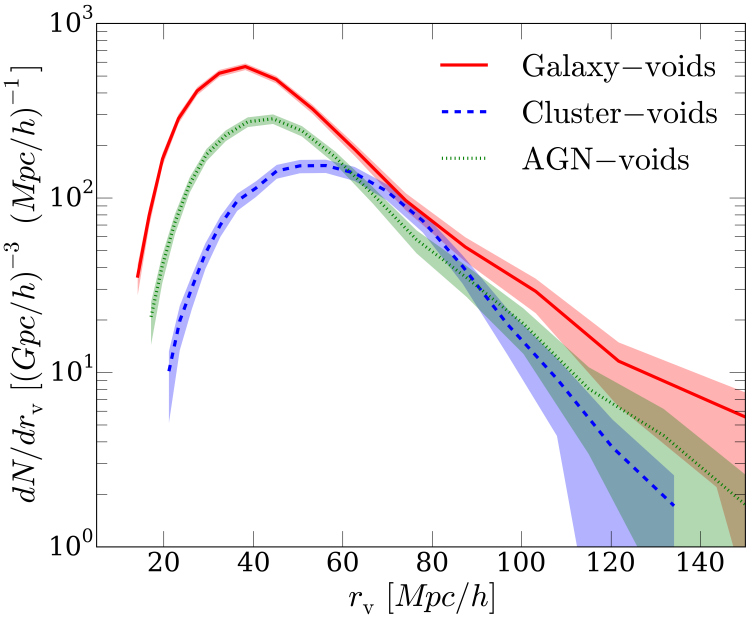

Figure 4.1: Abundances of voids in the MAGNETICUM simulation. Voids are identified in the distribution of galaxies (solid red line), clusters (dashed blue line) and AGN (dotted green line). The shaded area represents the error, calculated as Poisson uncertainty on the number counts. Using galaxies as tracers of the underlying density field of the Universe we are able to resolve and to find a sample of voids with a typical size between $15 - 60\,\mathrm{Mpc}/h$, twice as many as the sample of AGN-voids and 4 times as many as cluster-voids in the same range of size. We expect such a result due to the effect of the tracer sparsity on void finding [see 207]: with a low number of tracers (see Table 4.1) we are not able to resolve voids of small size.

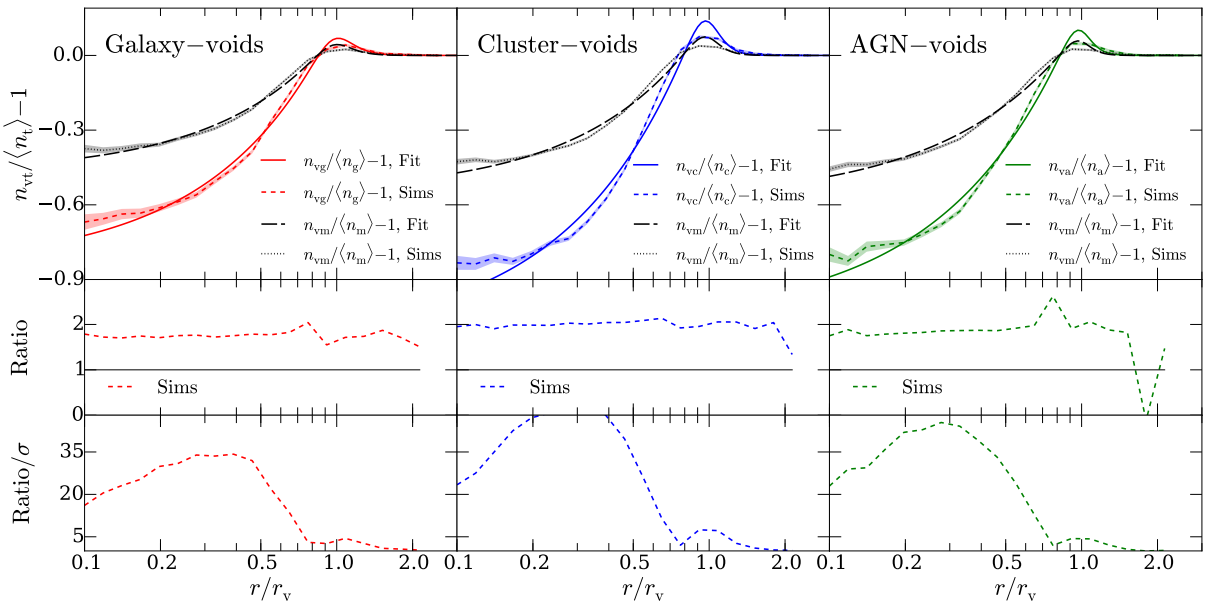

Figure 4.2: Top panels: measured over-density of tracers (short dashed line) and of matter (dotted line) around tracer-void centres (tracers being galaxies, clusters and AGNs from the left to the right). The solid lines show the fit of the tracer-profile using Equation 4.2.8. The same formula can be used to fit the matter-profiles (long dashed lines). The shaded areas are the uncertainty computed as the standard deviation from the mean profiles. In the mid panels we plot the ratios between tracer-profiles and matter-profiles around tracer-void centres, which look fairly constant. In the bottom panels we display the signal-to-noise ratios of the mid-panels. As the values of the measured profiles encounter zero, the signal-to-noise drops dramatically. These profiles are obtained by stacking voids with $80\,\mathrm{Mpc}/h < r_v < 90\,\mathrm{Mpc}/h$.

Matter over-density inside galaxy-traced voids

After this preliminary check, we can look at the distribution of matter around void-centres identified by the tracers. In the top panel of Figure 4.2 we show the stacked density profiles (i.e. the average density profile of voids of similar size) for tracer-voids with $80\,\mathrm{Mpc}/h < r_v < 90\,\mathrm{Mpc}/h$ (the tracers being galaxies, clusters and AGNs from the left to the right). Each profile is calculated by counting objects (tracers or dark matter particles) in the volume of spherical shells; the distances from void-centers are expressed in units of r_v and the profile density, n_{vt}, is expressed in terms of the mean density of tracers in the Universe $\langle n_t\rangle$. The errors are calculated as the standard deviation from the average density profile. We use full catalogues (for matter and tracers) without applying any sub-sampling in order to reduce as much as possible the impact of noise caused by sparsity.

In the top panels of Figure 4.2, the short dashed lines show the measured tracer-density profiles of tracer-voids in MAGNETICUM simulations and the solid lines are their fits computed with the formula given in Equation 4.2.8: as expected the fitting formula describes correctly the tracers' distribution around tracer-voids [207]. The dotted lines represent the matter distribution around tracer-void centers, and the long-dashed lines are their fits again with Equation 4.2.8. The formula by Hamaus, Sutter, and Wandelt [92] describes correctly the matter distribution around voids defined in tracers, too. The discrepancy in the inner regions is due to some residual sparsity ef-

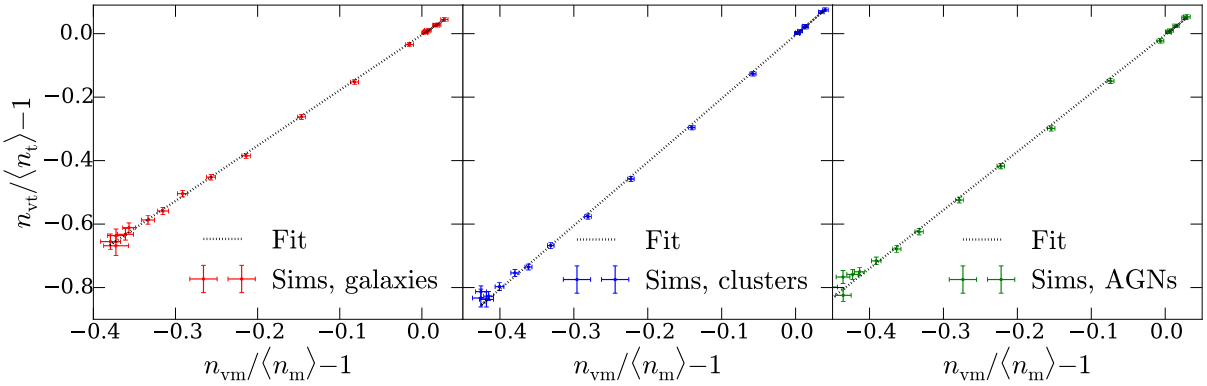

Figure 4.3: Over-density of luminous tracers around voids as a function of the matter over-density around tracer-void centres (both taken from Figure 4.2). The measured points are fitted with the linear function (dotted line) from Equation 4.3.1, in which the offset is consistent to zero within 5% (see Table 4.2). The error bars show the standard deviation from the mean profiles. From left to right the tracers are galaxies, clusters and AGNs.

fect, which becomes more important in the vicinity of void-centres. The fact that Equation 4.2.8 describes correctly also the dark matter under-densities around tracer-voids is a first interesting result; in fact, although Equation 4.2.8 has been already successfully tested both on matter voids and galaxy voids separately, in this particular case we are not defining voids in the matter itself: the void-finder is run only on top of observable tracers and we then look at the matter distribution around these potentially observable voids. So the profiles of voids are always self-similar and describable by Equation 4.2.8 although the finder is not directly run on the particles with which the profile is computed. Furthermore, in principle, once a relation between the tracer-density profile and the matter-density profile is established, we can link the latter to a potentially observable void-profile, therefore opening up the possibility of testing this finding with observations of voids where we can use the relative bias between tracers to calibrate this feature. Going back to the top panels of Figure 4.2, we observe that, as expected from theory and previous works [208], the tracer distributions around tracer-voids show a steeper profile when compared to the matter: in the vicinity of the void-centres we measure a larger matter density than tracer density, while on the edge of voids (i.e around $r \approx r_{\rm v}$) the tracer density is higher than the matter density.

In the middle panels of Figure 4.2, we display the ratio between the measured matter-profiles and tracer-profiles (dashed line). Although all ratios look fairly constant, there is a large signal-to-noise drop at $r \approx 0.75 r_{\rm v}$, i.e. where profiles have over-densities close to zero. This is shown clearly in the bottom panels of Fig. 4.2, in which the signal-to-noise ratio (where the noise is computed using error propagation, starting with the error on the density profiles) for the mid-panels is displayed. The fact that the ratios between tracer profiles and matter profiles look fairly constant is very promising, but it can be too naive to trust the values given by the profile-ratios as indicators of the matter-tracer relation considering the large signal-to-noise drop just discussed.

Table 4.2: Values of fit-parameters in Equation 4.3.1 for each tracer and void-size. We do not resolve enough cluster-voids with $20\,\mathrm{Mpc}/h < r_\mathrm{v} < 30\,\mathrm{Mpc}/h$ to perform our analysis, hence we can not report the values of the parameters in that case.

Voids	Galaxies		Clusters ($M_{500c} \geq 10^{13} M_\odot/h$)		AGNs	
r_v in Mpc/h	b_slope	c_offset	b_slope	c_offset	b_slope	c_offset
$20-30$	2.164 ± 0.061	-0.098 ± 0.012	–	–	2.395 ± 0.107	-0.086 ± 0.020
$30-40$	2.046 ± 0.026	-0.057 ± 0.004	2.415 ± 0.046	-0.041 ± 0.005	2.305 ± 0.052	-0.070 ± 0.007
$40-50$	1.890 ± 0.014	-0.023 ± 0.003	2.259 ± 0.027	-0.020 ± 0.003	2.125 ± 0.026	-0.030 ± 0.004
$50-60$	1.800 ± 0.012	-0.011 ± 0.003	2.144 ± 0.016	-0.011 ± 0.002	2.006 ± 0.021	-0.021 ± 0.003
$60-70$	1.751 ± 0.011	-0.007 ± 0.002	2.089 ± 0.011	-0.007 ± 0.001	1.925 ± 0.014	-0.007 ± 0.002
$70-80$	1.738 ± 0.008	-0.005 ± 0.002	2.030 ± 0.010	-0.005 ± 0.001	1.875 ± 0.012	-0.006 ± 0.002
$80-90$	1.746 ± 0.006	-0.004 ± 0.001	2.001 ± 0.010	-0.004 ± 0.001	1.840 ± 0.011	-0.005 ± 0.001
$90-100$	1.725 ± 0.008	-0.003 ± 0.001	1.972 ± 0.015	-0.003 ± 0.002	1.841 ± 0.010	-0.004 ± 0.001
$100-110$	1.767 ± 0.010	-0.002 ± 0.001	1.953 ± 0.014	-0.001 ± 0.002	1.852 ± 0.014	-0.002 ± 0.001
$110-120$	1.751 ± 0.007	-0.002 ± 0.001	1.908 ± 0.017	-0.003 ± 0.002	1.862 ± 0.022	-0.001 ± 0.002
$120-130$	1.735 ± 0.021	-0.002 ± 0.001	1.958 ± 0.019	-0.003 ± 0.002	1.892 ± 0.020	-0.001 ± 0.001
$130-150$	1.764 ± 0.012	-0.004 ± 0.001	1.951 ± 0.065	-0.007 ± 0.008	1.869 ± 0.021	-0.004 ± 0.002

A linear relation between matter- and tracer- overdensity

Another way to look at the dependence between matter and tracer distributions around voids is to plot one as function of the other. In Figure 4.3 we show the matter distribution around tracer-voids as a function of tracer distributions where the measured points are displayed as points with error-bars in both directions. We can fit these points with a simple linear function (dotted line):

$$\frac{n_\mathrm{vt}}{\langle n_t \rangle} - 1 = b_\mathrm{slope} \cdot \left(\frac{n_{vm}}{\langle n_m \rangle} - 1 \right) + c_\mathrm{offset}\,, \tag{4.3.1}$$

where n_vt is the measured tracer-density profile around tracer-voids, $\langle n_t \rangle$ is the mean tracer density, n_{vm} is the measured matter-density profile around tracer-voids, $\langle n_m \rangle$ is the mean matter density of the Universe, and b_slope and c_offset are the two free parameters of the linear fit, i.e. the slope and the offset, respectively. We find that the value of c_offset is always consistent with zero within 5% (except, due to sparsity, for small voids with $20\mathrm{Mpc}/h < r_\mathrm{v} < 30\mathrm{Mpc}/h$, in which $c_\mathrm{offset} \approx 0$ only within the 10%, see Table 4.2). Therefore, b_slope provides a single value which fully describes the relation between matter and tracer distributions: hence, we expect b_slope to be related to the linear bias. In the following we will show that b_slope in fact coincides with the linear bias, if sufficiently large voids are considered. This result suggests two main consequences: not only can we link the tracer-profiles and matter-profile of voids using the linear bias, but also we can think of b_slope as a novel way to measure the bias. We will discuss this latter possibility in Section 4.3.2.

What we have shown so far refers to voids with an effective radius r_v within $80\,\mathrm{Mpc}/h$ and $90\,\mathrm{Mpc}/h$ as a guiding example, but we did

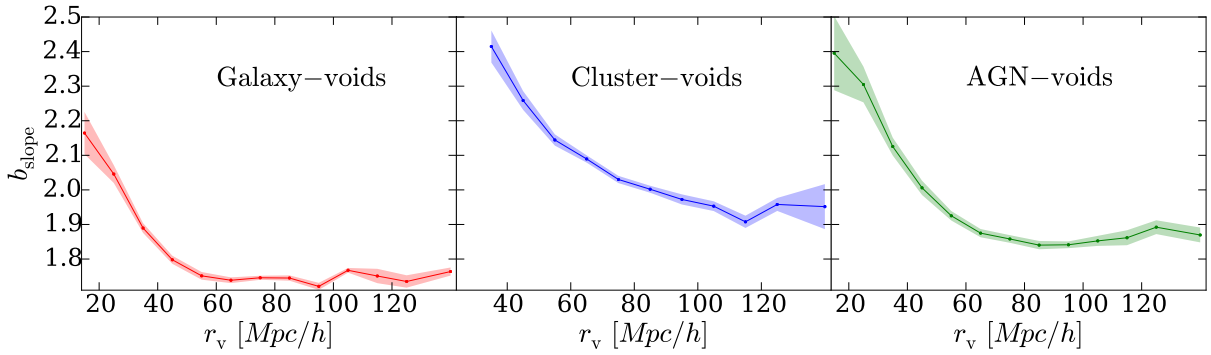

Figure 4.4: Value of $b_{\rm slope}$ from Figure 4.3 for galaxies (left-panel), clusters (mid-panel) and AGNs (right-panel) around galaxy-voids, cluster-voids and AGN-voids respectively, in various void-radius bins (i.e. as a function of void-size). The shaded area represents the uncertainty, obtained from the error on the fit. We see an impact of void-size on the measurement of $b_{\rm slope}$, which becomes larger for small voids.

perform our analysis using voids of various sizes. We report the bins in which the analysis is repeated in the first column of table 4.2. The bins are selected such that:

1. a sufficient number of voids is included in each bin so that the averaged profile is accurate enough to make the profile-fit and the linear-fit converge (i.e. at least ≈ 50 voids per bin);

2. the physical dimension of each single bin is not too extendend, in order to work under the hypothesis of considering voids of similar sizes, which is required by Equation 4.2.8;

3. all void-sizes are covered.

Dependence of $b_{\rm slope}$ on the void-size

We verified that in each bin we can always fit the relation between matter and tracers around voids with a simple linear relation. In Figure 4.4, we show the values for $b_{\rm slope}$ (see Equation 4.3.1) as a function of void-size (the tracers being, from the left, galaxies, clusters and AGNs). We see a trend: the value of $b_{\rm slope}$ decreases with the increase of void-size, showing that small voids yield a larger bias. As the size of voids surpasses a critical size, the value of $b_{\rm slope}$ stabilises asymptotically to a constant value. The critical void-size at which $b_{\rm slope}$ becomes stable seems to be dependent on the tracer properties (clusters, mid-panel, seem stable only starting at $r_{\rm v} \approx 80\,{\rm Mpc}/h$, while galaxies and AGNs show a stable value of $b_{\rm slope}$ for roughly $r_{\rm v} > 50{\rm Mpc}/h$) and on the number of tracers (i.e. on the sparsity of the sample). The shaded areas in Figure 4.4 represent the uncertainty obtained from the linear fits.

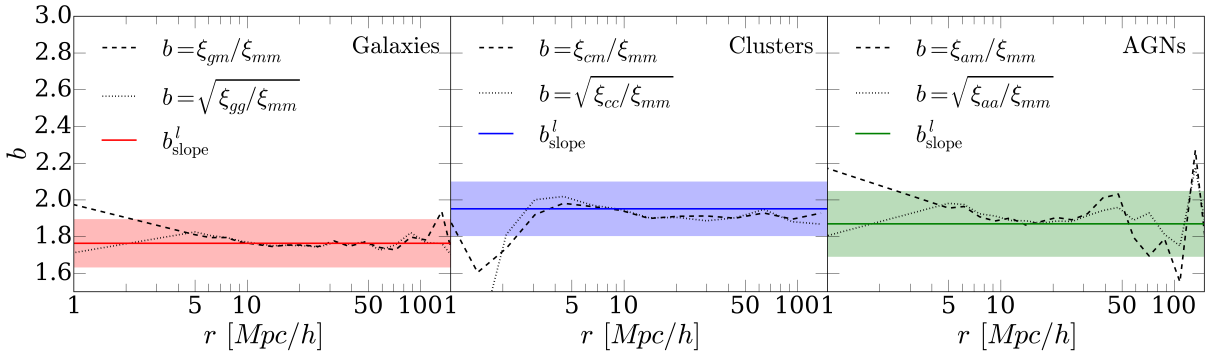

Figure 4.5: Comparison between different bias estimators: starting from the left panel, we plot the bias of galaxies calculated as the saturated value of the slopes from Figure 4.4, and the usual galaxy bias estimators presented in Equation 4.2.2 (dashed line) and Equation 4.2.3 (dotted line). The central and right panel show the cases of clusters and AGNs in blue and green respectively. We find a good consistency between $b^l_{\rm slope}$ and other bias estimators in the large-scale limit. The shaded area is the error, computed as the standard deviation from the mean value of $b_{\rm slope}$ from all void sizes.

4.3.2 *Linear bias*

To demonstrate convincingly that $b_{\rm slope}$ from our fit with Equation 4.3.1 is an indicator of the tracer bias, we compare its values with the most commonly used bias estimators (discussed in Section 4.2.2). In Figure 4.5 we show the bias computed with eqs. 4.2.2 (dashed lines) and 4.2.3 (dotted lines) and $b^l_{\rm slope}$ (solid lines), defined as the value of $b_{\rm slope}$ calculated in the bin that includes the largest voids of each sample (i.e. $130\,{\rm Mpc}/h < r_{\rm v} < 150\,{\rm Mpc}/h$): the aim is to confront the asymptotic measured value of $b_{\rm slope}$ (see Figure 4.4) with the linear bias. The shaded areas show the error on the mean value of $b_{\rm slope}$ from all void sizes.

A comparison of $b_{\rm slope}$ and linear bias values

As we can see in Figure 4.5, for all tracers (from the left to the right: galaxies, clusters and AGNs) $b^l_{\rm slope}$ agrees well with the bias calculated by eqs. 4.2.2 and 4.2.3 in the large-scale limit, but deviates on small scales. This result confirms that the linear bias gives a good description of the relation between luminous tracers and matter around voids, as long as sufficiently large voids are under study. Hence, computing the slope in Equation 4.3.1 with a simple linear fit, as described in Section 4.3.1, provides another technique to estimate the linear bias in simulations, if sufficiently large voids are analysed. Such a technique, in principle, allows to extend the measurement of linear bias to smaller scales inside voids. A caveat is the large uncertainty: close to void-centers Poisson noise increases and we should carefully consider how to further test this extension.

To additionally examine the consistency of our procedure to calculate the bias, we verify how $b_{\rm slope}$ changes after imposing various mass-cuts on the cluster sample. Namely, we demand the cluster

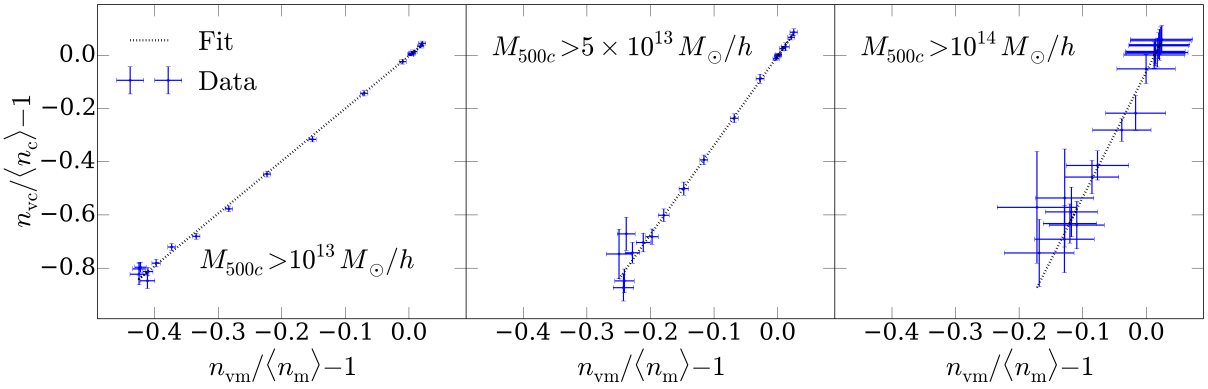

Figure 4.6: Distribution of clusters around cluster-void centers as a function of the matter-distribution around cluster-voids measured after applying various mass cuts: from the left to the right $M_{500c} > 10^{13}\,M_\odot/h$ (full sample), $M_{500c} > 5\times10^{13}\,M_\odot/h$ and $M_{500c} > 10^{14}\,M_\odot/h$. The measured points (blue) are fitted with a linear function (dotted line) presented in Equation 4.3.1. The slope increases from the left to the right panel as expected due to the increasing mass of the objects included in the analysis. We are showing the plot for the largest voids included in each sample, i.e. from left to right for voids with size $130-140\,\mathrm{Mpc}/h$, $170-200\,\mathrm{Mpc}/h$ and $220-290\,\mathrm{Mpc}/h$

A consistency check

mass to be $M_{500c} \geq 5\times10^{13}\,M_\odot/h$ and $M_{500c} \geq 10^{14}\,M_\odot/h$. To be conservative we rerun the void finding algorithm after applying each selection cut on top of the cluster-sample and we repeat the stacking procedure. By imposing these cuts we include a smaller number of clusters in the analysis (see Table 4.1), which implies that we are not able to resolve the smallest voids due to the sparsity of the tracers [see e.g. 207]. In order to include a sufficient number of voids we need to modify the binning employed in the stacking procedure. In fact, since we are not able to resolve the smallest voids, it is necessary to remove, shift, or enlarge some of the bins. Being able to resolve only very large voids in the sample of clusters with $M_{500c} \geq 10^{14}\,M_\odot/h$, we do not expect to find a high accuracy result; however we aim to find at least a qualitative indication that the bias that we measure using $b^l_{\rm slope}$ increases as expected in this case.

In Figure 4.6 we show the distribution of clusters around cluster-void centers as a function of their matter distribution (in analogy to Figure 4.3); we are displaying the relation for the largest voids in each sample, i.e. for voids with a $r_{\rm v}$ in the bin-size range (from the left to the right), of $130-140\,\mathrm{Mpc}/h$, $170-200\,\mathrm{Mpc}/h$ and $220-290\,\mathrm{Mpc}/h$. After applying the mass-cuts we are still able to fit the matter-tracer relation with a simple linear dependency (i.e. using Equation 4.3.1) where the offset value is consistent with zero. The exclusion of low-mass clusters from our main samples increases the noise on our measurement, which is now not as well determined as in Figure 4.3: the error bars are larger than in the full cluster-sample case and the simulation points are sometime further away from the fit (dotted line). However, we can clearly see that $b_{\rm slope}$ increases from

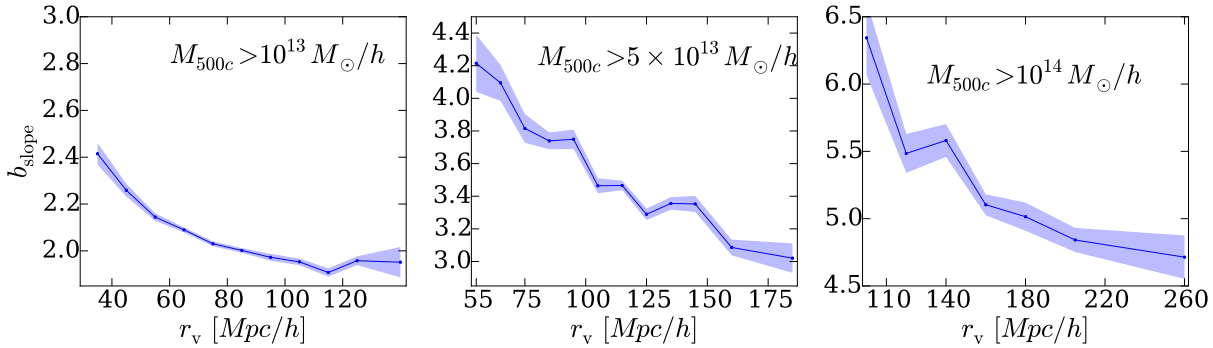

Figure 4.7: Values of $b_{\rm slope}$ after applying different mass cuts on the cluster sample as a function of void-size. The shaded area represents the uncertainty, obtained from the error on the fit. In agreement with previous findings we see an impact of void-size on the measurement of $b_{\rm slope}$, which becomes largest for small voids. In the cases in which a mass cut is applied (central and right panel, $M_{500c} \geq 5 \times 10^{13}\, M_\odot/h$ and $M_{500c} \geq 10^{14}\, M_\odot/h$) we observe that $b_{\rm slope}$ decreases as the void-size increases, although in a noisy manner. It is also not clear whether the convergence to the value of the linear bias is reached as in the full cluster sample (left panel).

the left to the right panels of Figure 4.6, following an expected trend, since we are imposing a larger and larger threshold on the mass-cut (therefore including only objects with higher and higher bias).

As previously done with the other tracers under study, we performed our analysis on voids of various size. We show how the value of $b_{\rm slope}$ changes as a function of void-size in Figure 4.7: going from the left to the right we display the curve for clusters with $M_{500c} \geq 10^{13}\, M_\odot/h$ (same as Figure 4.5, central panel, reported here for comparison), $M_{500c} \geq 5 \times 10^{13}\, M_\odot/h$ and $M_{500c} \geq 10^{14}\, M_\odot/h$. For what concerns the cases in which a mass cut is applied (central and right panels) we see, in agreement with our previous findings, that small voids yield a higher value of $b_{\rm slope}$, although the trend is not as clearly saturating as in the full-cluster sample (left panel). For the samples in which clusters have a mass $M_{500c} \geq 5 \times 10^{13}\, M_\odot/h$ and $M_{500c} \geq 10^{14}\, M_\odot/h$ we were also expecting an increasing critical void-size at which $b_{\rm slope}$ converges to a constant value, due both to the inclusion of highly biased tracers and due to their increased sparsity. However, in this cases $b_{\rm slope}$ does not converge to a constant value. It is therefore not clear whether we resolve voids large enough to reach the convergence value in the central and right panels.

We can now compare $b^l_{\rm slope}$ with the bias calculated using eqs. 4.2.2, 4.2.3. Since we are only considering clusters we can now include theory predictions to our plot, using the Mo&White formula (Equation 4.2.4) and its extension by Tinker (Equation 4.2.6). To estimate the mean value of $b_{\rm MW}$ and $b_{\rm Tinker}$ we use as weight the theoretical mass function calculated with Press and Schechter [167] and the Tinker et al. [215] respectively.

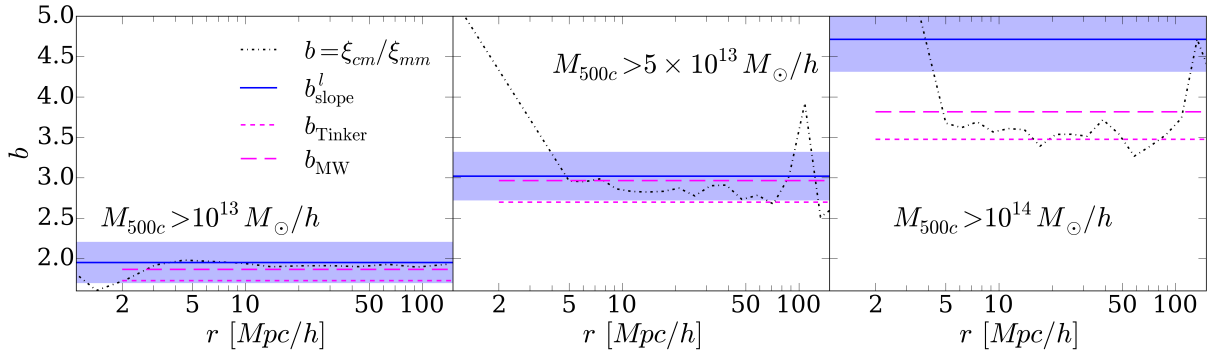

Figure 4.8: Comparison between different bias estimators and theory after applying various mass-cuts: we plot the bias of clusters calculated as $b^l_{\rm slope}$ (solid line), and the classical bias estimator (Equation 4.2.2, dashed-dotted line). The value predicted by Equation 4.2.6 and Equation 4.2.4 is shown by the dashed line and the long dashed line respectively. The shaded areas represent the standard deviation from the mean values of $b_{\rm slope}$.

In Figure 4.8 we plot the values of linear bias calculated with all of these methods. Namely:

- $b^l_{\rm slope}$ (solid line, the shaded area represents the error on the mean value of $b_{\rm slope}$ for voids of various sizes);
- b from Equation 4.2.2 (dashed-dotted line);
- $b_{\rm MW}$ from Equation 4.2.4 (long dashed line);
- $b_{\rm Tinker}$ from Equation 4.2.6 (dashed line).

Issues with a very sparse sample

For the most numerous cluster sample under study ($M_{500c} \geq 10^{13} M_\odot/h$, left panel), we are showing the same plot as Figure 4.5 (central panel) for the comparison. In this case and for $M_{500c} \geq 5 \times 10^{13}\, M_\odot/h$ (central panel) we find a good agreement of $b^l_{\rm slope}$, both with theory and with theoretical bias computed with eqs. 4.2.2 and 4.2.3. Values predicted by other bias estimators are within the uncertainty. As we commented before, the agreement is remarkable on large scales while on small scales the traditional bias estimators deviate from $b^l_{\rm slope}$. For what concerns the analysis in the sample which includes only clusters with $M_{500c} > 10^{14} M_\odot/h$ (right panel), we see a significant deviation of $b^l_{\rm slope}$ from other bias predictions. We expected the latter case to be the most problematic, given the large noise due to the extreme mass cut applied (see Table 4.1). Beside this, there is a practical motivation for such a discrepancy: as we suspected, we did not resolve enough large voids to determine the convergence of $b_{\rm slope}$. We are, in fact, forced to include voids of a wide range of sizes in the bin that contains the largest voids in this sample ($220 - 290\,{\rm Mpc}/h$) in order to obtain sufficiently smooth profiles and reach the convergence in the linear fit between matter-void profile and cluster-void density profile. This is absolutely necessary: if we would include only voids with

sizes between e.g. $225 - 290\,\mathrm{Mpc}/h$ the linear fit would not converge. Apparently, for this particular case, voids with $r_\mathrm{v} \approx 220\,\mathrm{Mpc}/h$ are too small to attain the convergence of b_slope to the value of the linear bias. Ideally, if we had resolved a sufficient number of very large voids ($r_\mathrm{v} > 250\,\mathrm{Mpc}/h$) we would recover the value of the linear bias also in this case, but the simulation box is too small to get a sufficiently large number of voids of that size. This is indeed a critical point as, the only way to tell if the b_slope converged to a saturated value is by looking at Figure 4.4 and Figure 4.7. Moreover, for practical purposes we can use the relative bias between different tracers for that matter, which is accessible in observations.

As we commented before, it is not clear by Figure 4.7 whether b_slope converges to a constant value for the cluster samples with $M_{500c} \geq 5 \times 10^{13}\,M_\odot/h$ and $M_{500c} \geq 10^{14}\,M_\odot/h$: looking at Figure 4.8 we can conclude that the convergence is reached for $M_{500c} \geq 5 \times 10^{13}\,M_\odot/h$ but not for the most extreme mass cut. It is remarkable that, in the latter case, we understand why the convergence of b^l_slope can not occur. However, we have demonstrated that our method of calculating the bias with b^l_slope is quite consistent when applied on samples with various masses which was the aim of this test.

To summarize this Section, we have shown that the relation between matter and matter-tracers in voids is always linear and determined by a single number b_slope. This result was established by directly measuring the distribution of matter and tracers around voids and incidentally validates recent work that simply assumed the bias of tracers to be linear in the vicinity of voids. Furthermore we showed that, by measuring the matter profile and the matter-tracer profiles around large voids in simulations, we can estimate the value of the linear bias via the slope of a simple linear fit between the two distributions, if sufficiently large voids are considered.

4.4 SUMMARY, DISCUSSION AND CONCLUSIONS

Summary of the results

With the help of a suite of state-of-the art hydro-simulations we have investigated the stacked tracer-density profile of cosmic voids and linked it to their underlying matter-density profile. Before discussing the implications of our findigs, we recap all major results presented in this Chapter:

- **The underlying matter-density profile of tracer-voids is well described by the fitting formula presented in Hamaus, Sutter, and Wandelt [92].** Such a formula was known to describe the profile of tracer-voids and matter-voids separately, but in this Chapter we have successfully tested it on depressions of the matter-density field around tracer-voids, i.e. without running the void finder on dark matter particles. This result points out once again the degree of self-similarity of underdense regions

in our Universe, as they can always be described by the same fitting function.

- **The relation between the density of tracers and matter around voids is always linear and determined by a multiplicative constant ($b_{\rm slope}$).** This remarkably simple relation was tested using galaxy, cluster and AGN samples extracted from MAGNETICUM *Pathfinder*, including voids of various sizes and applying different mass cuts on top of the cluster sample. The linear relation between matter and tracers always stands, regardless of tracer type and host-halo mass range.
- **The value of the multiplicative constant decreases with the increase of the size of voids and asymptotes to the linear bias.** For sufficiently large voids, $b_{\rm slope}$ is shown to match the linear bias extracted from the usual tracer auto-correlation, the tracer cross-correlation with dark matter, and the expectations from theory, such as the bias functions proposed by Mo&White and Tinker. The critical void-size at which $b_{\rm slope}$ converges to the linear bias is dependent on the clustering properties of the tracers under study (and on their sparsity). In fact, we find that for the full cluster sample the critical void-size is around $80\,{\rm Mpc}/h$ while for AGNs it is around $60\,{\rm Mpc}/h$ and for galaxies about $50\,{\rm Mpc}/h$. In order to eliminate the effect of sparsity, we subsampled all tracers to the density of our full cluster sample. This test reveals that the critical void size at which $b_{\rm slope}$ reaches a saturated value also depends on tracer properties other than density, such as their bias. If a highly biased and very sparse population is used as tracer of the density field, it can be possible that not enough large voids are available and hence we can not establish the constant value to which $b_{\rm slope}$ converges. The large values of $b_{\rm slope}$ obtained by small voids show that they yield a biased result. We leave further investigations on the origin of this effect to future studies.

The correspondence between $b_{\rm slope}$ and linear bias is expected at linear order in the density fluctuations, because we can consider the stacked tracer-density profile of voids as a void-tracer cross-correlation function $\xi_{\rm vt}(r)$ (see Equation 4.2.9), and express it in terms of the void-matter cross-correlation function,

$$\xi_{\rm vt}(r) = b\xi_{\rm vm}(r)\,, \tag{4.4.1}$$

via the linear tracer bias b. We find that Equation 4.4.1 is in principle valid for arbitrarily small values of r, as long as large enough voids are considered, in stark contrast to the common two-point statistics of tracers appearing in eqs. 4.2.2 and 4.2.3. For the latter, the linear bias model can break down below scales on the order of $\sim 50{\rm Mpc}/h$

at low redshift and is therefore not applicable for a dominant fraction of available Fourier modes of the density field.

Discussion

Furthermore, this technique can yield important advantages for the analysis of survey data. In order to maximize the amount of cosmological information contained within the common two-point statistics of large-scale structure one has to make use of sophisticated perturbation theory frameworks to consistently include all higher-order bias parameters [e.g. 24, 82, 131, 184]. Alternatively, one can marginalize over the unknown free parameters of an empirical function that models non-linear bias in a phenomenological way. However, both approaches are very limited, they quickly break down towards smaller scales and the total information gain does not scale with the additional number of modes included.

As long as tracer bias remains scale-independent, as shown to be the case in void-tracer cross-correlations, these limitations do not apply. An example for such a cosmological analysis is the study of redshift-space distortions around voids [4, 38, 48, 95, 96, 99], but the interpretation of many other observables, such as void abundance, void lensing, void clustering and the void ISW effect may benefit from a linear bias treatment as well. An exciting perspective is to look out for additional physical effects that induce a non-linear scale-dependent tracer bias around voids, and are typically neglected in standard ΛCDM. One such example is the effect of massive neutrinos [19, 39, 43, 123]. Similar signatures can be expected in scenarios of modified gravity [5, 36] or coupled dark energy [164]. While we leave further research along these lines for future work, we describe a first attempt at testing Equation 4.4.1 with observational data in the next Chapter.

5

ON THE RELATIVE BIAS OF VOID TRACERS IN THE DARK ENERGY SURVEY

This Chapter was written in collaboration with Nico Hamaus, Kerstin Peach, Klaus Dolag, Jochen Weller and the Dark Energy Survey (DES) collaboration. Its results are included in a paper currently submitted to MNRAS [166]

A summary of this Chapter

As widely summarised in this thesis, luminous tracers of large-scale structure are not entirely representative of the distribution of mass in our Universe. As they arise from the highest peaks in the matter density field, the spatial distribution of luminous objects is biased towards those peaks (see Section 2.3.3). On large scales, where density fluctuations are mild, this bias simply amounts to a constant offset in the clustering amplitude of the tracer, known as linear bias (see Section 4.1). In this Chapter we focus on the *relative* bias between galaxies and galaxy clusters that are located inside and in the vicinity of cosmic voids, extended regions of relatively low density in the large-scale structure of the Universe. Firstly - employing hydrodynamical simulations - we verify that the relation between galaxy and cluster over-density around voids remains linear. Hence, the void-centric density profiles of different tracers can be linked by a single multiplicative constant. This amounts to the same value as the relative linear bias between tracers for the largest voids in the sample. For voids of small sizes, which typically arise in higher density regions, this constant has a higher value, possibly showing an environmental dependence similar to that observed for the linear bias itself. We confirm our findings by analysing mocks and data obtained during the first year of observations by the Dark Energy Survey. As a side product, we present the first catalogue of three-dimensional voids extracted from a photometric survey with a controlled photo-z uncertainty. Our results will be relevant in forthcoming analyses that attempt to use voids as cosmological probes.

Structure

This Chapter is organized as follows: in Section 5.1 we recall some introductory knowledge (to the benefit of the reader who might be interested in this chapter only) in Section 5.2 we present all the data employed in our study (hydro-sims, DES mocks and DES data); in Section 5.3 we describe the void finding algorithm, as well as all the methods employed to estimate the relative bias of tracers; in Section 5.4 we present the results of our analysis; finally we discuss our conclusions in Section 5.5.

5.1 INTRODUCTORY MATTERS

Summary of the hypothesis we want to test

The bias of tracers has been typically studied via the correlation function or the power spectrum of all tracers as a whole, regardless of their cosmic-web environment [see, e.g., 35, 68, 193, 194, 200, and references therein]. Recently, however, the properties of bias were investigated focusing on tracers located in the vicinity of cosmic voids, as reviewed in Chapter 4.

To summarise the results presented in the previous Chapter we may simply write that the void-tracer cross-correlation function $\xi_{\rm vt}(r)$ exhibits a linear relation with the corresponding void-matter cross-correlation function $\xi_{\rm vm}(r)$, with a proportionality constant $b_{\rm slope}$,

$$\xi_{\rm vt}(r) = b_{\rm slope}\, \xi_{\rm vm}(r). \tag{5.1.1}$$

Furthermore, the best-fit value for $b_{\rm slope}$ decreases monotonically towards larger voids, and saturates to a constant number for the largest voids. This number was shown to coincide with the linear tracer bias $b_{\rm t}$, which can be either calculated from theory, or determined using the common bias estimators. Hence, $b_{\rm slope}$ in Equation 5.1.1 can be expressed as follows:

$$b_{\rm slope}(r_{\rm v}) \begin{cases} > b_{\rm t}\ , \text{for } r_{\rm v} < r_{\rm v}^{+} \\ = b_{\rm t}\ , \text{for } r_{\rm v} \geq r_{\rm v}^{+}\ , \end{cases} \tag{5.1.2}$$

where $r_{\rm v}$ is the average, and $r_{\rm v}^{+}$ the critical effective void radius of the sample. In other words, Equation 5.1.1 linearly relates tracer and matter densities around voids in all cases, but $b_{\rm slope}$ coincides with the linear bias $b_{\rm t}$ only when voids of size $r_{\rm v} > r_{\rm v}^{+}$ are considered in the measurement [for visualization please refer to Figure 4.4 in Chapter 4 or Figure 4 of 165]. The precise value of $r_{\rm v}^{+}$ depends on various properties of the tracer distribution itself, such as its sparsity and bias. Nevertheless, Equation 5.1.1 provides a very simple guideline of how to infer the distribution of mass around voids in the tracer distribution[1]. The aim of this Chapter is to show that the same applies when relating different types of tracers around voids, both in simulations, and for the first time in observational data as well.

The results of Pollina et al. [165] provide a first step to connect theory with practice, as Equation 5.1.1 allows us to bridge the gap between the matter- and tracer density profiles around observationally defined voids. In fact, these results have already been employed to this end by Ronconi and Marulli [178], who extended their theoretical void size function to voids traced in haloes thanks to Equation (

1 Note that Nadathur and Percival [138] find a residual from the linearity of Equation 5.1.1 when $b_{\rm slope}$ is fixed to the linear bias $b_{\rm t}$, while Pollina et al. [165] and this analysis treats it as a free parameter.

Despite the fact that Equation 5.1.1 has a number of interesting consequences and applications, it is challenging to test experimentally, as the dark matter density cannot be observed directly in all three dimensions. However, voids can also be used as weak gravitational (anti-)lenses to infer their projected surface mass density [50, 114, 132, 185]. Either a deprojection of the void lensing profiles to 3D, or a projection of tracer density profiles to 2D then allows us to constrain the bias relation in voids (Fang et al., in prep). Another possibility is to apply Equation 5.1.1 to different tracers of the matter distribution. As long as every individual tracer obeys a linear clustering bias with respect to the dark matter, the relative clustering bias between the tracers should remain linear as well.

In this analysis we will make use of galaxies and galaxy clusters as two distinct tracer types. These are the most commonly available and abundant tracers in current surveys, and at the same time exhibit very different clustering properties. We will use the distribution of galaxy *clusters* to define our void sample, thanks to their higher fidelity in providing photometric redshifts and thus accurate distance estimates. The relative bias relation between galaxies and galaxy clusters will be thoroughly investigated in the vicinity of those voids. In order to provide a controlled setup, we first develop our analysis techniques based on state-of-the-art hydrodynamical simulations (MAGNETICUM). Our methods are then applied to the REDMAGIC galaxy– and REDMAPPER galaxy cluster catalogues originating from the first year of observations by the DES collaboration. Realistic mock catalogues provided by the MICE 2 project that have been constructed to specifically mimic the observations which will be used to validate our conclusions.

5.2 SIMULATIONS, DATA AND MOCKS

5.2.1 *Simulations*

The hydrodynamical simulation suite MAGNETICUM *pathfinder*[2] (Dolag et al, in prep.) has already been presented in Section 4.1.1, to which we refer the reader for a thorough understanding. In this Chapter we only consider MAGNETICUM clusters above $10^{14}h^{-1}M_{\odot}$ for purposes of void finding. For our analysis we make use of the galaxy and cluster samples extracted from the simulation at redshift $z = 0.14$ with the criteria explained in Section 4.1.1. In Table 5.1 we summarise some properties of the tracers relevant in this work.

2 http://www.magneticum.org

Table 5.1: Properties of the galaxy and cluster samples in the MAGNETICUM simulations. The minimum mass $M_{\rm min}$ is given in terms of stellar mass M_* for galaxies, and in terms of $M_{\rm 500c}$ for clusters. $N_{\rm t}$ is the total number of tracers and $N_{\rm v}$ the corresponding number of identified voids.

Tracers	$M_{\rm min}[M_\odot/h]$	$N_{\rm t}$	$N_{\rm v}$
Galaxies	$M_* = 1 \times 10^{11}$	6.5×10^6	-
	$M_* = 5 \times 10^{11}$	2.6×10^6	-
	$M_* = 1 \times 10^{12}$	3.5×10^5	-
Clusters	$M_{\rm 500c} = 1 \times 10^{14}$	1.0×10^5	1053

5.2.2 *Data*

The Dark Energy Survey

The Dark Energy Survey [DES, see 213] is an on-going 5 year observational campaign supported by an international collaborative effort. It employs the 570 megapixel Dark Energy Camera [DECam, see 78, 101] mounted on the Blanco telescope at the Cerro Tololo Inter-American Observatory (CTIO). At the end of its operations, DES will have mapped approximately 300 million galaxies and tens of thousands of clusters over a 5000 square degree footprint in the southern hemisphere. DES provides photometric data using five filters (*grizY*) to the limiting magnitude of 24th *i*-band [107], although the relevant limiting magnitude for this study is 22.5 in *i*-band, as it constrains the observations of galaxies [67]. In this work we employ data obtained during the first year of observation (Y1) taken between Aug. 31 2013 and Feb. 9 2014, that have already shown their potential in constraining cosmology [58]. DES Y1 wide-field observations scanned a large region extending approximately between $-60° < \delta < -40°$ overlapping the South Pole Telescope (SPT) survey footprint, screening an area of 1321 deg^2 (A1). A much smaller area overlapping the "Stripe 82" of the Sloan Digital Sky Survey (SDSS) was also mapped by DES, but this region will not be included in our analysis. From the Gold catalogues [67], 26 million galaxies were selected for the weak lensing sample. Recently the first three years of the observational campaign were made public with the first DES data release [2].

5.2.2.1 *Galaxy clusters*

Redmapper clusters

We make use of *red-sequence Matched-filter Probabilistic Percolation* (REDMAPPER) Y1A1 clusters [129], both to use them as tracers of the large-scale structure, and to identify cosmic voids in the latter. The photometric red-sequence cluster finder REDMAPPER is specifically developed for large photometric surveys. It identifies galaxy clusters by searching for a bulk of its population to be made up of old, red galaxies with a prominent 4000Å-break. Focusing on this spe-

cific galaxy population the algorithm increases the contrast between cluster and background galaxies in colour space, and it enables accurate and precise photometric redshift estimates, with a scatter of $\sigma_z/(1+z) = 0.01$ level for $z < 0.7$ [183], which includes the redshift window employed for this data analysis. The associated cluster richness estimator, λ, is the sum of the membership probability of every galaxy in the cluster field, and has been optimized to reduce the scatter in the richness-mass relation [179, 180, 182]. For a more detailed description of the algorithm we refer to [183]. In this work we will employ cluster samples with $\lambda > 5$, which corresponds to a minimum mean mass of about $\sim 10^{13} h^{-1} M_\odot$ following the mass-richness relation of McClintock et al. [129]. This low richness cut that does not guarantee the purest cluster selection. In the analyses presented in this Chapter, however, we are not interested in the detailed properties of individual clusters. Rather, we desire the selected sample to be used as a tracer of large-scale structure, regardless of whether some of its objects are true clusters or not. The resulting full catalogue contains 103423 clusters and has proven to be optimal for the task of void identification, owing to its relatively high cluster density of about $10^{-4} h^3 \mathrm{Mpc}^{-3}$.

5.2.2.2 *Galaxies*

Redmagic galaxies

We also employ *red-sequence Matched-filter Galaxy Catalog* (REDMAGIC) Y1A1 galaxies [73] as tracers of large-scale structure. The REDMAGIC algorithm [181] is automated for selecting Luminous Red Galaxies (LRGs) and was specifically designed to minimize photometric redshift uncertainties in photometric large-scale structure studies, resulting in a photo-z bias $z_{\mathrm{spec}} - z_{\mathrm{photo}}$ better than 0.005 and in a scatter $\sigma_z/(1+z)$ of 0.017. REDMAGIC achieves this goal by self-training the colour cuts necessary to produce a luminosity-thresholded LRG sample of constant comoving density. In this work we will distinguish among three different REDMAGIC samples, denoted as *high density* (brighter than $0.5\,L_*$ and density $10^{-3} h^3 \mathrm{Mpc}^{-3}$), *high luminosity* (brighter than $1\,L_*$ and density $4 \times 10^{-4} h^3 \mathrm{Mpc}^{-3}$), and *higher luminosity* (brighter than $1.5\,L_*$ and density $10^{-4} h^3 \mathrm{Mpc}^{-3}$).

5.2.3 *DES Mocks*

In order to validate our results, we make use of mock catalogues extracted from the MICE 2 project. MICE 2, based on the original MICE (MareNostrum - Instituto de Ciencias del Espacio) project [55, 79], is a suite of large high-resolution N-body simulations that have been run with the GADGET 2 code [197]. Including 4096^3 particles in a box size of $3.072 h^{-1}$Gpc, MICE 2 resolves haloes with even lower mass resolution ($2.93 \times 10^{10}\, h^{-1} M_\odot$) than MICE, making this particular simulation a perfect tool in providing mocks for deep and sensitive surveys such

Mocks of the 5-year DES observations

as DES. FoF halo catalogues extracted from the simulations are populated by galaxies using a Halo Occupation Distribution (HOD), which assigns luminosities to the central and satellite galaxies so that their observed luminosity function is preserved. The MICE 2 galaxy catalogue is forced to match luminosity, colours and clustering properties of DES at redshift $z = 0.1$, from where a light cone is then extrapolated by replicating and translating the simulation box, allowing one to build an output with negligible repetition up to redshift $z = 1.4$. In this work we are going to employ the largest available light cone, which reproduces a full octant of the sky with the same properties as the DES Y1 observations, such as photometry. More specifically, we will employ the REDMAGIC galaxy and REDMAPPER cluster catalogues extracted from MICE 2 to asses the impact of photometric redshift uncertainty on our results.

5.3 METHODS

5.3.1 *Void finder*

We employ the Void IDentification and Examination toolkit VIDE [210] to construct our void catalogues. VIDE implements an enhanced version of ZOBOV [ZOnes Bordering On Voidness, 141], an algorithm that identifies density depressions in a 3-dimensional set of points. The void finding procedure has been summarised in Section 3.3. In this Chapter we will employ the most general void catalogue produced by VIDE, without applying any further selection cuts on density or hierarchy levels of voids. We recall that we define the void centre as the volume-weighted barycentre $\vec{X}$ of the N Voronoi cells that define each void,

Void-selection, centre and radius

$$\vec{X} = \sum_{i=1}^{N} \vec{x}_i \cdot V_i \Big/ \sum_{i=1}^{N} V_i \,, \tag{5.3.1}$$

where $\vec{x}_i$ are the coordinates of the i-th tracer of that void, and V_i the volumes of their associated Voronoi cells. The *effective* void radius r_v is calculated from the total volume of the void V_v. It is defined as the radius of a sphere with the same volume,

$$V_\mathrm{v} \equiv \sum_{i=1}^{N} V_i = \frac{4\pi}{3} r_\mathrm{v}^3 \,. \tag{5.3.2}$$

5.3.2 *Correlation functions*

In order to explore the clustering statistics around voids we will employ correlation functions. For the analyses based on the hydro-

simulations, that admit periodic boundary conditions, we will employ the same method as presented in Section 4.2.1 to compute the correlation function.

However, in real observations we are detecting tracers inside irregular boundaries of a survey mask on the past light cone. In that situation it is helpful to employ a catalogue of randoms to isolate true from fake correlations in the data. To this end the *Landy-Szalay* estimator [115] provides a way to calculate the void-tracer cross-correlation function from data catalogues D and random catalogues R for each tracer and void sample,

Landy-Szalay estimator

$$\xi_{\mathrm{vt}}(r) = \frac{\langle D_{\mathrm{v}} D_{\mathrm{t}} \rangle - \langle D_{\mathrm{v}} R_{\mathrm{t}} \rangle - \langle D_{\mathrm{t}} R_{\mathrm{v}} \rangle + \langle R_{\mathrm{v}} R_{\mathrm{t}} \rangle}{\langle R_{\mathrm{v}} R_{\mathrm{t}} \rangle} \,, \tag{5.3.3}$$

where angled brackets symbolize normalized pair counts at separation r in units of r_{v}. They can be calculated as histograms in analogy to Equation 4.2.9.

We recall that void density profiles exhibit a few very characteristic features (see Section 4.2.4): a deep under-dense core in the very centre, and an over-dense ridge (compensation wall) close to the effective radius r_{v}. The empirical function presented in Equation 4.2.8 was shown to capture these features accurately [92]. We report it here for convenience,

$$\frac{n_{\mathrm{vt}}(r)}{\langle n_{\mathrm{t}} \rangle} - 1 = \delta_c \frac{1 - (r/r_s)^{\alpha}}{1 + (r/r_{\mathrm{v}})^{\beta}} \,, \tag{5.3.4}$$

where δ_c is the central density contrast at $r = 0$, r_s a scale radius at which the density equals the average density of tracers $\langle n_{\mathrm{t}} \rangle$, and α, β describe the inner and outer slopes of the profile.

5.3.3 *Bias estimation*

In simulations the clustering bias of any tracer can directly be calculated, because the dark matter particle locations are available. Therefore, it is simply given by the ratio of tracer and matter correlation functions (see Section 4.2.1). Therefore, it is simply given by the ratio of tracer and matter correlation functions,

$$b_{\mathrm{t}} = \sqrt{\frac{\xi_{\mathrm{tt}}(r)}{\xi_{\mathrm{mm}}(r)}} \simeq \frac{\xi_{\mathrm{tm}}(r)}{\xi_{\mathrm{mm}}(r)} \,. \tag{5.3.5}$$

The second equality only holds on large scales in the linear regime, where b_{t} is a constant number. In a similar manner we can define the relative bias between a tracer t_1 and a tracer t_2 as

$$b_{\rm rel} \equiv \frac{b_{\rm t_1}}{b_{\rm t_2}} = \sqrt{\frac{\xi_{\rm t_1 t_1}(r)}{\xi_{\rm t_2 t_2}(r)}} \simeq \frac{\xi_{\rm t_1 t_2}(r)}{\xi_{\rm t_2 t_2}(r)} \,, \tag{5.3.6}$$

where, without loss of generality, we may choose tracer $\rm t_1$ to be the more highly biased one, such that $b_{\rm rel} > 1$. In this analysis we will associate the highly biased tracer with galaxy clusters, and the less biased tracer with galaxies.

A technique to estimate the relative bias in observational data

In observational data, where we do not have direct access to the mass distribution, the absolute clustering bias of tracers can only be determined indirectly. We follow the approach of Paech et al. [148] and calculate the angular power spectra between tracer $\rm t_1$ and tracer $\rm t_2$ using the public code CLASS[3] [26] and its extension CLASSgal [62],

$$C_\ell^{\rm t_1 t_2} = 4\pi \int \frac{{\rm d}k}{k} P_{\rm ini}(k) \Delta_\ell^{\rm t_1}(k) \Delta_\ell^{\rm t_2}(k) \,. \tag{5.3.7}$$

Here, $P_{\rm ini}(k)$ is the dimensionless primordial power spectrum at wavenumber k and

$$\Delta_\ell^{\rm t}(k) = \int {\rm d}z \, b_{\rm t} \frac{{\rm d}N_{\rm t}(z)}{{\rm d}z} j_\ell \left[k\, r(z)\right] D(z) T(k) \,, \tag{5.3.8}$$

where ${\rm d}N_{\rm t}(z)/{\rm d}z$ is the redshift distribution and $r(z)$ the comoving distance of tracer t, j_ℓ the spherical Bessel function, $D(z)$ the growth factor, and $T(k)$ the transfer function. Assuming a fiducial flat ΛCDM cosmology with the parameters $h = 0.678$, $\Omega_{\rm b} = 0.048$, $\Omega_{\rm m} = 0.308$, $\sigma_8 = 0.826$, $z_{\rm re} = 11.3$ and $n_{\rm s} = 0.96$ [159], we can then infer the effective values of $b_{\rm t_1}$, $b_{\rm t_2}$ and their ratio (averaged within the considered redshift range) from the angular auto-power spectra of the two tracers. The angular power spectra are determined using the public code POLSPICE[4] [47, 211] from a pixellated map of the projected tracer-density contrast on the sky. As in Paech et al. [148], we treat the shot noise contribution to the angular power spectra as a free parameter, and consider a multipole range of $20 < \ell < 500$. The covariance of the C_ℓ's is estimated via applying a jack-knife sampling of the map, splitting up the map area into 100 contiguous regions of equal size.

5.4 ANALYSIS

In this section we present the results of our analysis pipeline, applied to MAGNETICUM simulations, MICE 2 mocks, and finally DES data. We emphasize that all void catalogues employed in this Chapter are identified in the cluster samples at hand, regardless of the nature of the

3 http://class-code.net

4 http://www2.iap.fr/users/hivon/software/PolSpice

data set analysed. If needed, we refer to those voids as *cluster-voids*, to distinguish them from voids identified in a different tracer population[5].

5.4.1 *Hydro-simulations*

With the help of the fully hydro-dynamical simulations MAGNETICUM we investigate whether it is possible to use a similar approach to that presented by Pollina et al. [165], albeit only considering clusters and galaxies as tracers. In this manner the relative bias is expected to obey similar properties as the linear bias, in analogy to Equation 5.1.1. The idea is to only use void catalogues that are defined in the most highly biased population available and then compute the average tracer-density profiles around voids of similar size using clusters and galaxies separately. The latter are hence exclusively used to compute galaxy-density profiles around cluster-voids.

Step I: validation with hydro-sims

We apply a conservatively high mass cut of $M_{\rm min} = 10^{14} h^{-1} M_\odot$ to our MAGNETICUM clusters, firstly to make sure that we do not include objects that are of too low detection significance in the observed data, and secondly to achieve a relative bias between our cluster and galaxy sample that is significantly larger than unity. Since the lower limit for the bias of the galaxy sample is set by the mass resolution of the simulation, we can only boost the relative bias by increasing $M_{\rm min}$ for the cluster sample. This implies a lower resolution for smaller voids due to tracer sparsity [for further details on sparse sampling and void finding, see 207], so the resulting void catalogue contains rather large objects. However, as we are only interested in the relation between tracer-density profiles around a fixed void population, the absolute distribution of void sizes does not matter for our purposes.

In the top panel of Figure 5.1 we show the stacked density profile of such cluster-voids computed twice: once using the same cluster population they were identified in (dashed black line), and once using the full galaxy sample extracted from MAGNETICUM (red dotted line). The shaded areas represent the uncertainty on the mean density profile, computed as the standard deviation of all individual void profiles from their mean. The void density profiles are calculated following the procedure explained in the beginning of Section 5.3.2, including voids of effective radii in the range $190 h^{-1}\text{Mpc} < r_{\rm v} < 220 h^{-1}\text{Mpc}$. The function from Equation 5.3.4 is used to fit the density profiles (solid black for clusters and long-dashed red for galaxies), yielding a good match in both cases. This corroborates the universal character of Equation 5.3.4 with respect to tracer type. The very characteris-

5 The procedure can also be inverted, i.e. it is possible define voids in the galaxy sample and then use those voids to measure the density of galaxies and clusters around them. For consistency with the approach in Pollina et al. [165] presented in the previous Chapter, and for the advantage that will be presented in section 5.4.2.1, we use the more highly biased tracer to identify voids.

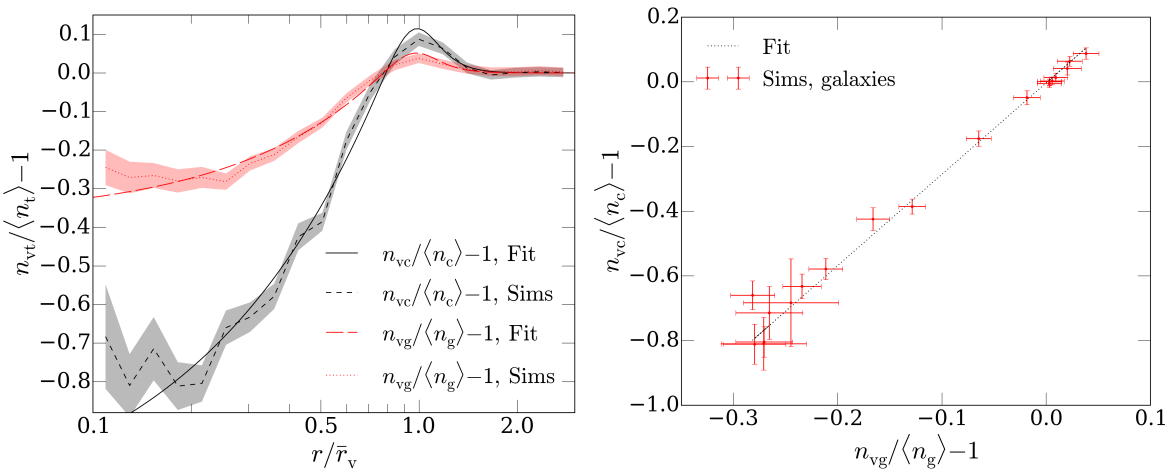

Figure 5.1: Top: Tracer-density profiles (dashed black for clusters, dotted red for galaxies) around cluster-defined voids of radius $190h^{-1}\text{Mpc} < r_v < 220h^{-1}\text{Mpc}$ in the MAGNETICUM simulation. Solid black and long-dashed red lines show the best fits obtained via Equation 5.3.4. Bottom: Cluster- and galaxy-density profiles from the left panel plotted against each other (black points with error bars). The dotted black line shows the best fit using Equation 5.4.1.

tic features are a clear under-dense core close in the void centre and a compensation wall around $r \simeq r_v$, which are most pronounced in the cluster-density profile. When the density profile of galaxies around the same cluster-voids is computed, those features are less pronounced, but still clearly visible. Because clusters have a higher clustering bias than galaxies, this behaviour is expected.

Our aim is to constrain the detailed relation between the two void density profiles. In particular, we want to check whether it is linear, similar to the relation between tracers and mass found in [165]. To this end we plot the cluster-density profile $\xi_{vc}(r)$ as a function of the corresponding galaxy-density profile $\xi_{vg}(r)$ of the same cluster-voids. The results are depicted as red dots in the bottom panel of Figure 5.1, where the error bars show the uncertainty on the mean density profiles from the left panel. The following simple linear function is used to fit those data points (black dotted line):

$$\xi_{vc}(r) = b_{slope}\xi_{vg}(r) + c_{offset}\,, \tag{5.4.1}$$

where b_{slope} and c_{offset} are the only two free parameters of the fit. The linear relation between $\xi_{vc}(r)$ and $\xi_{vg}(r)$ is evident, and in concordance with the linearity between $\xi_{vc}(r)$ and the matter-density profile $\xi_{vm}(r)$ from earlier work [165]. The best-fit values for b_{slope} and c_{offset}, including their 1σ uncertainties can be found in Table 5.2. c_{offset} is compatible with zero within the error, while b_{slope} attains a value of about 2.7. We expect b_{slope} to be related to the relative bias between clusters and galaxies, in analogy to Equation 5.3.6.

A preliminary confirmation coming from hydro-sims

We repeated the previous analysis for voids of different size, and confirmed the linear relation in Equation 5.4.1 to provide a good fit

Table 5.2: Best-fit values and 1σ uncertainties on the parameters of Equation 5.4.1 for cluster-defined voids of various size and for different stellar-mass cuts in the galaxy sample from the MAGNETICUM simulation.

Voids	Gal. ($M_* > 1 \times 10^{11} h^{-1} M_\odot$)		Gal. ($M_* > 5 \times 10^{11} h^{-1} M_\odot$)		Gal. ($M_* > 1 \times 10^{12} h^{-1} M_\odot$)	
Bins in r_v [h^{-1}Mpc]	b_{slope}	c_{offset}	b_{slope}	c_{offset}	b_{slope}	c_{offset}
$90 < r_v < 110$	3.43 ± 0.39	-0.033 ± 0.089	2.02 ± 0.33	-0.013 ± 0.095	1.20 ± 0.21	-0.005 ± 0.022
$110 < r_v < 130$	3.01 ± 0.10	-0.009 ± 0.070	1.80 ± 0.21	-0.003 ± 0.064	1.12 ± 0.14	-0.001 ± 0.020
$130 < r_v < 150$	3.11 ± 0.26	-0.009 ± 0.063	1.76 ± 0.20	-0.005 ± 0.063	1.12 ± 0.14	-0.000 ± 0.055
$150 < r_v < 170$	2.83 ± 0.22	-0.007 ± 0.045	1.77 ± 0.22	-0.003 ± 0.063	1.11 ± 0.14	-0.001 ± 0.045
$170 < r_v < 190$	2.82 ± 0.26	-0.003 ± 0.063	1.77 ± 0.20	-0.001 ± 0.061	1.15 ± 0.14	-0.002 ± 0.045
$190 < r_v < 220$	2.71 ± 0.22	-0.009 ± 0.045	1.72 ± 0.17	-0.004 ± 0.060	1.10 ± 0.14	-0.002 ± 0.055
$220 < r_v < 250$	2.59 ± 0.33	-0.035 ± 0.105	1.68 ± 0.28	-0.017 ± 0.101	1.15 ± 0.22	-0.000 ± 0.095

in all cases. The best-fit values of b_{slope} and c_{offset} are summarized in Table 5.2. Furthermore, we explored the impact of various mass cuts in our galaxy sample. The overall clustering amplitude of galaxies is expected to depend on their stellar mass, which should be reflected in our best fit for b_{slope} as well. While our original sample contained all galaxies with stellar mass above $1 \times 10^{11} h^{-1} M_\odot$, we impose two more restrictive cuts with $M_* > 5 \times 10^{11} h^{-1} M_\odot$ and $M_* > 1 \times 10^{12} h^{-1} M_\odot$. Also for these cases we can confirm the linear relation of Equation 5.4.1 to perform a good fit. The corresponding parameter constraints are reported in Table 5.2. In Figure 5.2 the best-fit values of b_{slope} are shown as a function of the mean effective radius of the selected void sample. The three panels correspond to the different stellar-mass cuts applied to the galaxy catalogue. We observe a clear trend of b_{slope} decreasing with void size, a similar behaviour of what has been presented in Pollina et al. [165], albeit the different setup. In that study b_{slope} converges to a constant value for voids larger than a critical size, and this value is shown to coincide with the linear bias of the tracer with respect to the matter distribution.

In this Chapter, however, we are comparing the density profiles of two different tracers against each other, consequently we expect b_{slope} to converge towards the ratio of the linear bias parameters of both tracers, the linear relative bias b_{rel}. We can estimate b_{rel} via Equation 5.3.6 in two ways, both of which are plotted in Figure 5.3 as solid and dashed black lines with shaded error bars, respectively. On large scales both estimators agree with each other, and yield the linear relative bias between the two tracers. We compare this value with the best fit for b_{slope} obtained from the largest effective radius bin of our void sample (red solid line with shaded error bar), which is the most likely one to have converged towards b_{rel}. In the different panels of Figure 5.3 only the stellar-mass cut for the galaxy sample is varied, with the same values as used in Figure 5.2.

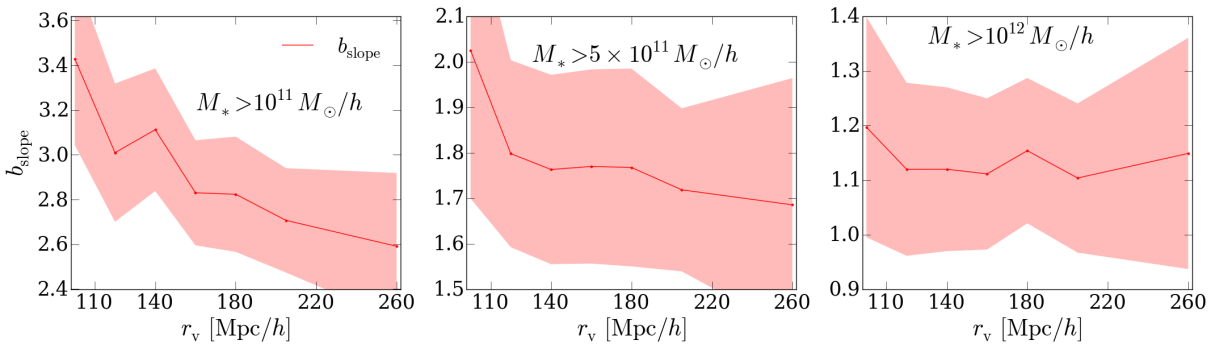

Figure 5.2: Best-fit values for $b_{\rm slope}$ as a function of effective void radius in the MAGNETICUM simulation. The stellar-mass cut for the galaxy sample is varied from left to right, as indicated in each panel. The cluster sample has a fixed mass cut of $M_{500c} > 10^{14}h^{-1}M_\odot$, it is also used for the void identification.

As evident from Figure 5.3, the convergence of $b_{\rm slope}$ towards $b_{\rm rel}$ is not complete in all cases. Only for the highest stellar-mass cut of $M_* > 10^{12}h^{-1}M_\odot$ in the galaxy sample are the two values consistent with each other within the errors. At the same time, the relative bias attains the lowest value in this case, owing to the higher bias of the galaxy sample. The lower the stellar-mass cut for the galaxies, the lower becomes their bias. Therefore the relative bias between clusters and galaxies increases, which also increases the discrepancy between $b_{\rm slope}$ and $b_{\rm rel}$. Hence, the higher the relative bias between two tracers, the larger becomes the critical void radius $r_{\rm v}^+$ at which $b_{\rm slope}$ and $b_{\rm rel}$ converge. When voids are defined in sparse tracer distributions, such as the galaxy clusters considered here, the size of $r_{\rm v}^+$ may fall well beyond the range of effective void radii that can be found in the entire void sample. A similar conclusion has already been drawn in Pollina et al. [165], where the value of $r_{\rm v}^+$ was investigated for voids identified in denser tracer samples.

Nevertheless, this first test shows that the findings of Pollina et al. [165], summarised in Chapter **??**, can be indeed reproduced by measuring the relative bias with the analysis proposed in this section, which can be fully implemented with observational data.

5.4.2 *DES Mocks*

Step II: validation with mocks – how to handle light-cone and photometric uncertainty

Having confirmed a linear relationship between the densities of luminous tracers in void environments using the MAGNETICUM simulation, we now want to move to more realistic data. The next step is to test our pipeline on DES mocks (MICE 2, see Section 5.2.3, to evaluate the impact of the light cone and photometric redshift uncertainty. The latter has so far been considered as an insurmountable obstacle for the identification of three-dimensional voids, as the typical photo-z scatter of a single galaxy corresponds to line-of-sight distance errors that

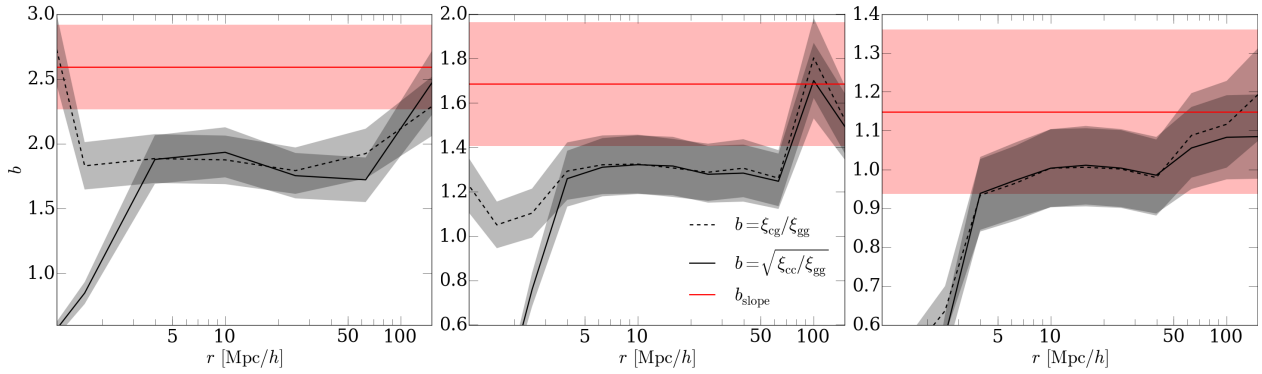

Figure 5.3: Comparison of the best-fit b_{slope} obtained from our largest void sample (solid red line) to the relative bias b_{rel} between clusters and galaxies in the MAGNETICUM simulation, calculated using the estimators as indicated (black dashed and dotted lines). The stellar-mass cut for the galaxy sample is varied from left to right, with the same values as in Figure 5.2.

are comparable to the extent of most voids. This limitation lead to other innovative ideas on how to investigate the potential of voids for cosmology, which explored under-dense regions of large-scale structure in two-dimensional projections on the sky [89, 185]. It has been demonstrated how this approach opens up complementary ways to constrain cosmology [21, 44, 81, 90]. Nevertheless, as the properties of three-dimensional voids have already been extensively studied in simulations and spectroscopic surveys (see references in the introduction), it is worth testing a similar method with photometric data.

5.4.2.1 *Redshift uncertainty and void finding*

To evaluate the impact of photometric redshift uncertainty on void finding we run VIDE on the REDMAGIC and REDMAPPER samples of the MICE 2 mocks twice: once using the spectroscopic redshift (spec-z), and once the photometric (photo-z) redshift estimate of each object. The photo-z scatter inherent in the latter effects the distance estimation and causes the distribution of objects to be smeared out along the line of sight.

In Figure 5.4 we present the void size function (i.e., the spatial number density of voids as a function of their effective radius) in the MICE 2 mocks, extracted using VIDE on both spectroscopic and photometric samples of galaxies and clusters. While the abundance of galaxy-voids (solid and dashed red) is heavily skewed by photo-z scatter, cluster-voids (dotted and dash-dotted blue) remain surprisingly unaffected by the choice of redshift estimate. In particular, the number of galaxy-voids with $\bar{r}_v < 35h^{-1}$ Mpc is clearly overestimated when using photo-z, while the opposite is the case for larger galaxy-voids. This finding is different to what has previously been seen in Sánchez et al. [185], where the largest galaxy-voids in the REDMAGIC sample were least affected by photo-z uncertainty. The disagreement

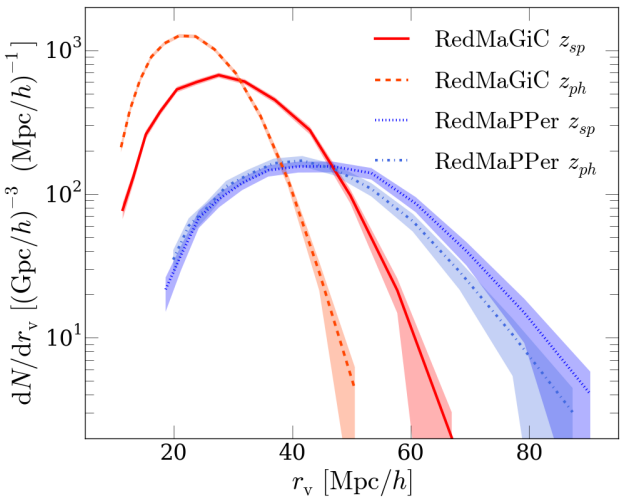

Figure 5.4: The abundance of voids identified in the galaxy and cluster samples of the MICE 2 mocks, as a function of their effective radius. Both photometric and spectroscopic redshifts have been used in each case, as indicated in the figure legend. The cluster-void size function is not significantly affected by photo-z uncertainty. In fact, clusters provide the most accurate photometric redshift measurements and cluster-voids are the largest voids, further reducing the relative impact of photo-z scatter on void finding.

is most likely a consequence of the different void finding techniques. The fact that [185] utilized a two-dimensional void finder on projected slices, with a line-of-sight width above the typical photo-z scatter, largely mitigates the effects of the latter. In contrast, VIDE directly operates on three-dimensional particle distributions, and the photo-z scatter results in an unphysical line-of-sight smearing of structures that can be detected as spurious watershed ridges in the algorithm. The result is that larger voids are more likely to be segmented into multiple smaller voids.

Clusters are the best tracer of under-densities in photometric data

However, this effect on void abundance is hardly detected in the cluster-void sample, thanks to the relatively accurate photometric redshift estimates in REDMAPPER clusters. The higher accuracy can be attributed to the fact that multiple member galaxies can contribute to a single cluster redshift estimate. Moreover, the sparser and more biased distribution of clusters results in larger voids overall [207], so the extent of the photo-z scatter in redshift space matters less in comparison to the void size. In order to quantify the impact of photometric redshifts on void identification in more detail, a comparison on individual voids would be needed. However, this goes beyond the scope of this analysis, as we are only concerned about summary statistics here.

The robustness of the void size function from cluster-voids in the presence of photo-z scatter has promising consequences for void science with photometric surveys. For example, void number counts can

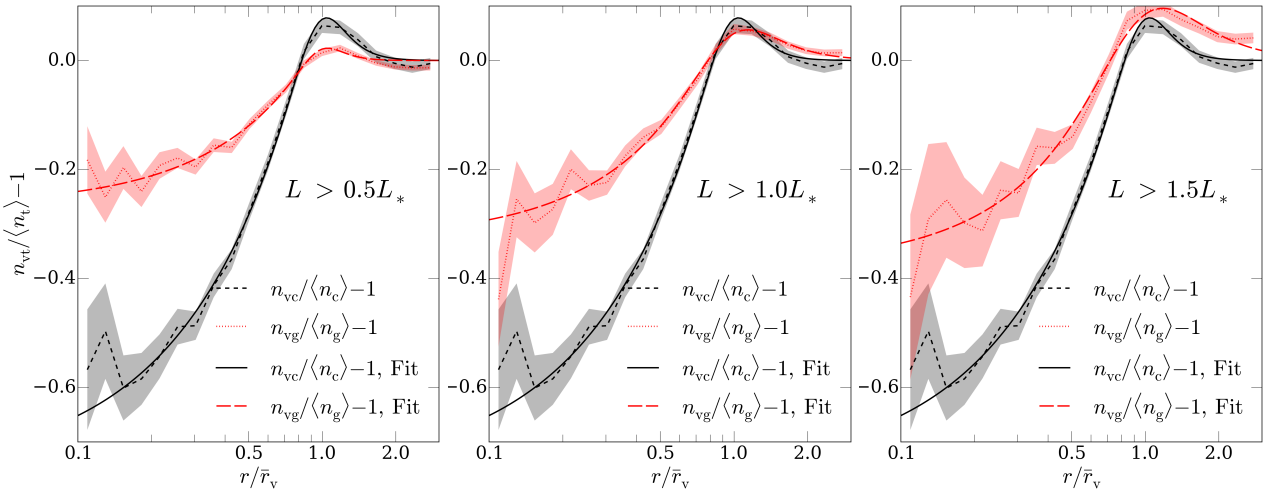

Figure 5.5: Tracer-density profiles (solid black for REDMAPPER clusters, dashed red for REDMAGIC galaxies) around cluster-defined voids of size $50h^{-1}\text{Mpc} < r_v < 60h^{-1}\text{Mpc}$ in the MICE 2 mocks. The luminosity cut for the galaxy sample is varied from left to right, as indicated in each panel.

be used to constrain cosmology [157], even when identified in various tracer distributions. In particular, Ronconi and Marulli [178] suggest a simple way to extend the prediction of void abundances to potentially observable voids: making use of Equation 5.1.1 they claim to be able to accurately forecast the void size function obtained from haloes based on results from the excursion-set theory for dark matter voids. According to Figure 5.4, this method may straight-forwardly be extended to cluster-voids extracted from photometric samples, opening up to the possible exploitation of the void size function as a cosmological probe in a large variety of forthcoming surveys [e.g., LSST, EUCLID, DESI, see 59, 103, 116]

5.4.2.2 *Density profiles and tracer bias*

We now repeat the analysis of Section 5.4.1 with the MICE 2 mocks, using photometric redshifts for both REDMAGIC and REDMAPPER samples. The density profiles are estimated with the help of random catalogues, to account for the mask and light-cone effects. To this end, we approximate the Landy-Szalay estimator of Equation 5.3.3 as

$$\xi_{vt}(r) \simeq \langle D_v D_t\rangle - \langle D_v R_t\rangle \,, \tag{5.4.2}$$

which was shown to yield accurate results on void scales [97]. We have also compared our measurements with the more common Davis-Peebles estimator [60], which features a ratio instead of a subtraction in Equation 5.4.2, and found consistent results.

Figure 5.5 presents the corresponding tracer-density profiles for REDMAPPER-defined voids of size $50h^{-1}\text{Mpc} < r_v < 60h^{-1}\text{Mpc}$. Overall we obtain smaller void sizes from this sample, as the number

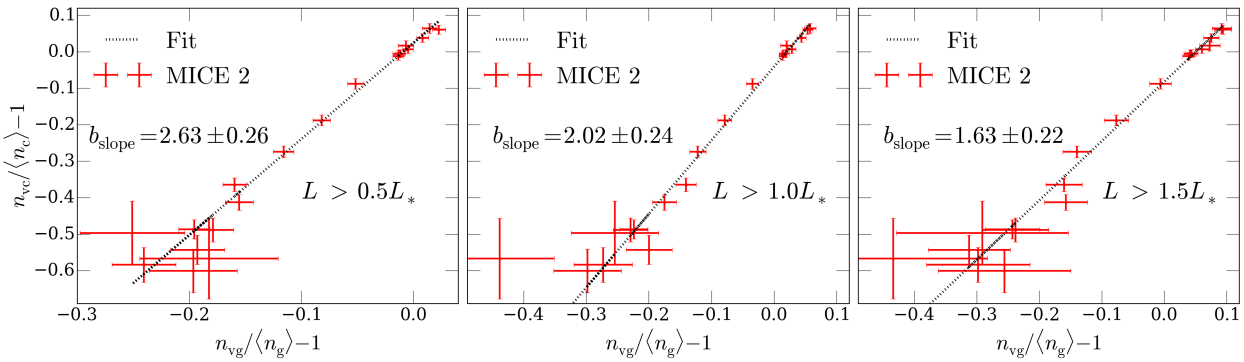

Figure 5.6: Cluster- and galaxy-density profiles from Figure 5.5 plotted against each other. The dotted black line shows the best fit obtained with Equation 5.4.1.

density of clusters here exceeds the one analysed in MAGNETICUM. However, as MICE 2 resolves galaxies of lower mass, this results in a similar relative bias between the tracers considered. As tracers, we utilize REDMAPPER clusters of richness $\lambda > 5$, and three REDMAGIC samples with varying luminosity cuts. The correspondence with our earlier simulation results in the left panel of Figure 5.1 is striking: we observe a more pronounced cluster-density profile with a deeper core and a higher ridge (dashed black line) than each of the galaxy-density profiles (dotted red line). Yet, the shapes of all these profiles seem to match quite nicely, which means that galaxies trace voids just as the clusters do, albeit with a lower clustering amplitude. This is further confirmed by the successful interpolation of all profiles by means of the fitting function presented in Equation 5.3.4 (solid black and long-dashed red lines). Note that in some cases the normalization of the profiles at large distances r can be slightly offset from zero. This can have various reasons, which may be related to imperfect corrections for the survey geometry, or the spread in void sizes in a given bin of $r_{\rm v}$. However, we have checked that the magnitude of this effect is small enough not to impact our conclusions (i.e., $c_{\rm offset}$ is always consistent with zero).

The correspondence between the different tracers can be seen more clearly in Figure 5.6, where their void-centric density profiles are plotted against each other. A linear trend in the data is apparent, so we fit Equation 5.4.1 and constrain its slope and offset again. We further repeat this for voids of all available sizes from our catalogue and summarize the results in Table 5.3. The best-fit value for $b_{\rm slope}$ decreases when galaxies with higher luminosity cut are used. This is consistent with expectation, as they acquire a higher clustering bias, making the relative bias between clusters and galaxies decrease. In contrast, the parameter $c_{\rm offset}$ remains consistent with zero in all cases.

The dependence of $b_{\rm slope}$ on void effective radius is visualized in Figure 5.7. We observe a decreasing trend again, as before in the MAGNETICUM simulation. Towards the largest voids, $b_{\rm slope}$ converges

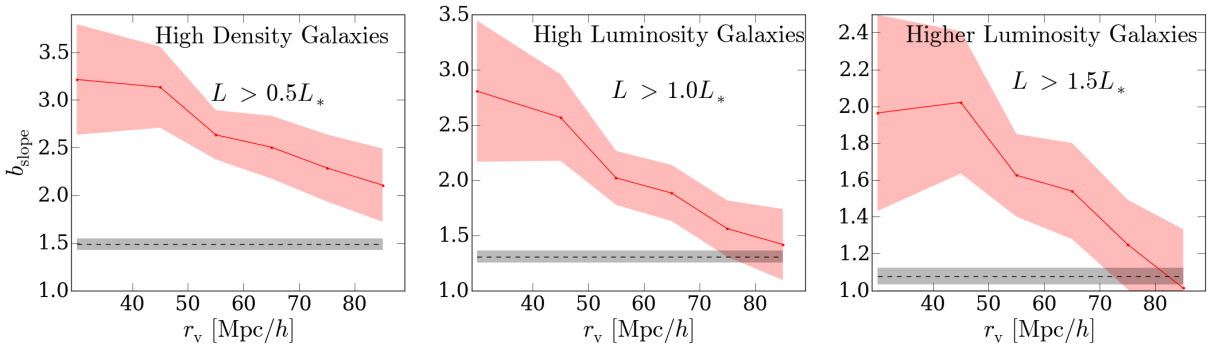

Figure 5.7: Best-fit values for $b_{\rm slope}$ (solid red) as a function of effective void radius in the MICE 2 mocks. The luminosity cut for the galaxy sample is varied from left to right, as indicated in each panel. Dashed black lines show the linear relative bias between clusters and galaxies, estimated via their angular power spectra on large scales.

Table 5.3: Best-fit values and 1σ uncertainties on the parameters of Equation 5.4.1 for cluster-defined voids of various size and for different luminosity cuts in the galaxy sample from the MICE 2 mocks.

Voids	REDMAGIC ($L > 0.5L_*$)		REDMAGIC ($L > 1.0L_*$)		REDMAGIC ($L > 1.5L_*$)	
Bins in $r_{\rm v}$ [h^{-1}Mpc]	$b_{\rm slope}$	$c_{\rm offset}$	$b_{\rm slope}$	$c_{\rm offset}$	$b_{\rm slope}$	$c_{\rm offset}$
$20 < r_{\rm v} < 40$	3.21 ± 0.57	-0.071 ± 0.130	2.80 ± 0.64	-0.119 ± 0.173	1.96 ± 0.53	-0.084 ± 0.158
$40 < r_{\rm v} < 50$	3.13 ± 0.42	-0.006 ± 0.084	2.56 ± 0.39	-0.066 ± 0.089	2.02 ± 0.39	-0.090 ± 0.10
$50 < r_{\rm v} < 60$	2.63 ± 0.27	0.023 ± 0.063	2.02 ± 0.23	-0.041 ± 0.063	1.62 ± 0.22	-0.082 ± 0.091
$60 < r_{\rm v} < 70$	2.50 ± 0.33	0.070 ± 0.105	1.88 ± 0.24	-0.043 ± 0.077	1.54 ± 0.26	-0.111 ± 0.183
$70 < r_{\rm v} < 80$	2.28 ± 0.35	0.101 ± 0.126	1.56 ± 0.25	-0.067 ± 0.084	1.25 ± 0.24	-0.174 ± 0.190
$80 < r_{\rm v} < 90$	2.10 ± 0.39	0.162 ± 0.161	1.41 ± 0.32	-0.127 ± 0.128	1.01 ± 0.31	-0.262 ± 0.354

to the linear relative bias between the cluster and the galaxy samples (dashed black line), which is estimated via the method described in Section 5.3.3. However, the critical void radius $r_{\rm v}^+$, where the two relative bias measurements agree, cannot be determined from the galaxy sample with the lowest luminosity cut. This confirms our earlier conclusion that the convergence of $b_{\rm slope}$ to $b_{\rm rel}$ happens at larger void radii when $b_{\rm rel}$ is higher. However, we have a clear indication that it is possible to measure the relative linear bias of tracers with this method when applied to the final DES dataset after 5 years of observations. We further conclude that the uncertainty inherent in photometric redshift estimates is not affecting our results from before: the linear relation of Equation 5.1.1 is still satisfied to the same degree of accuracy as in simulations, with similar constraints on its parameters.

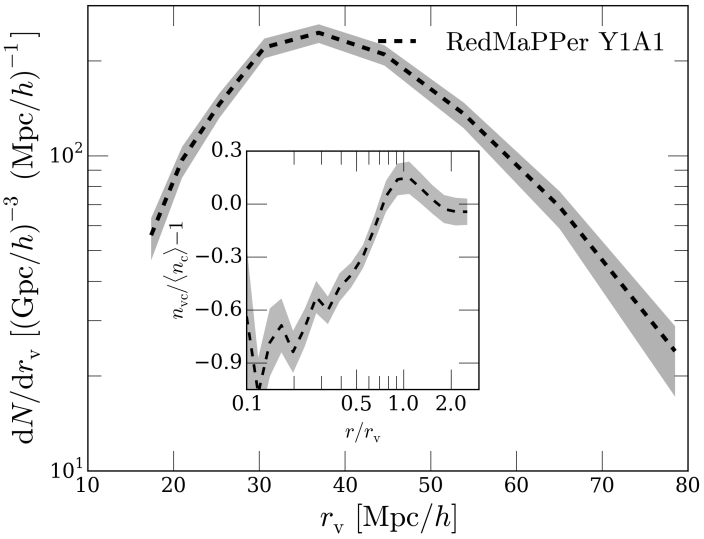

Figure 5.8: Abundance of voids as a function of their effective radius, identified in the distribution of redMaPPer clusters from DES data (Y1A1). The average cluster-density profile of all voids is shown as inset.

5.4.3 *Data*

The finale: is linearity in the sky?

Having assessed the feasibility of our analysis using mocks, we are finally ready to test it on DES Y1 data and to determine whether the linear relation given by Equation 5.1.1 (applied to visible tracers) is in the sky. In this section we describe the void catalogue obtained from the data and present all related results.

5.4.3.1 *DES void catalogue*

Three-dimensional DES voids

This section presents the first catalogue of three-dimensional watershed voids built with DES data. We follow our previous approach, using redMaPPer clusters with $\lambda > 5$ for void identification with vide. Since the area observed during the first year of DES (Y1A1) operations is significantly smaller (1321deg^2) than the full octant of the mice 2 mocks, the number statistics of the data are expected to be lower. In total we find 475 voids in the redshift range $0.2 < z < 0.65$ (which is the range where all redMaGiC samples are fairly volume limited), with effective radii between $15h^{-1}$Mpc and $80h^{-1}$Mpc. Voids intersecting with the survey mask have been pruned from the final sample. The void size function is shown in Figure 5.8, with an inset displaying the average cluster-density profile of all voids in the sample. It is remarkably similar to that of cluster-voids in mocks shown in Figure 5.4. The small difference can be caused by the assumed mass-richness relation in the cluster mocks, which may not reproduce the real data exactly. The footprint of our void catalogue on the sky can be perceived in Figure 5.9, which was made using the public code

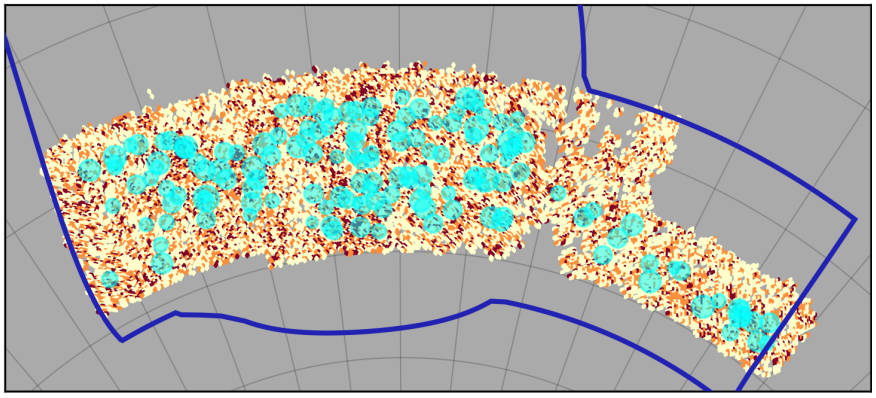

Figure 5.9: Density plot of redMaPPer clusters and their associated void centres (cyan circles) in a redshift slice of $0.2 < z < 0.45$. The blue line displays the 5-year-DES footprint, voids intersecting with the survey mask are discarded.

skymapper[6]. We show the positions of void centres (cyan circles) on the density plot of clusters for a redshift slice of $0.2 < z < 0.45$. This range was chosen to allow direct comparison with Figure 1 of Gruen et al. [90], where a similar map for the location of line-of-sight underdensities in the galaxy spatial distribution was presented. The blue line displays the full DES footprint at the end of its operations. Figure 5.10 is a three-dimensional plot of the DES light cone, where 5% of all redMaPPer clusters are shown in magenta, 5% of those clusters located inside voids are highlighted in green, and black spheres of radius r_v indicate the locations of void centres with a size that reflects the spherical equivalent of the watershed volume. The number of clusters was diluted for visualization purposes.

5.4.3.2 *Density profiles and tracer bias*

With the observational void catalogue at hand, we are now in the position to apply our earlier analysis to real data. Figure 5.11 features the average tracer density profiles for cluster-voids of size $40h^{-1}\text{Mpc} < r_v < 80h^{-1}\text{Mpc}$. As tracers, we use redMaPPer clusters (dashed black lines) and redMaGiC galaxies of high density, high luminosity, and higher luminosity samples (dashed red lines, from left to right). As apparent from each panel, the densities of different tracers are highly correlated in these void environments, all featuring a clear depression around the void centre, and a compensating ridge at the void edge. In particular, the similarity with the mocks in Figure 5.5 is striking, as is the ability of Equation 5.3.4 to accurately fit the data (solid black and long-dashed red lines). However, due to the smaller area it can be noted that the uncertainties in the real data are higher, especially close to the void centres, where the statistics are most affected by the sparsity of tracers.

This can also be observed in Figure 5.12, where we focus on the relation between cluster- and galaxy-density profiles plotted against each other. The linear trend in the data is apparent, although some of

6 https://github.com/pmelchior/skymapper

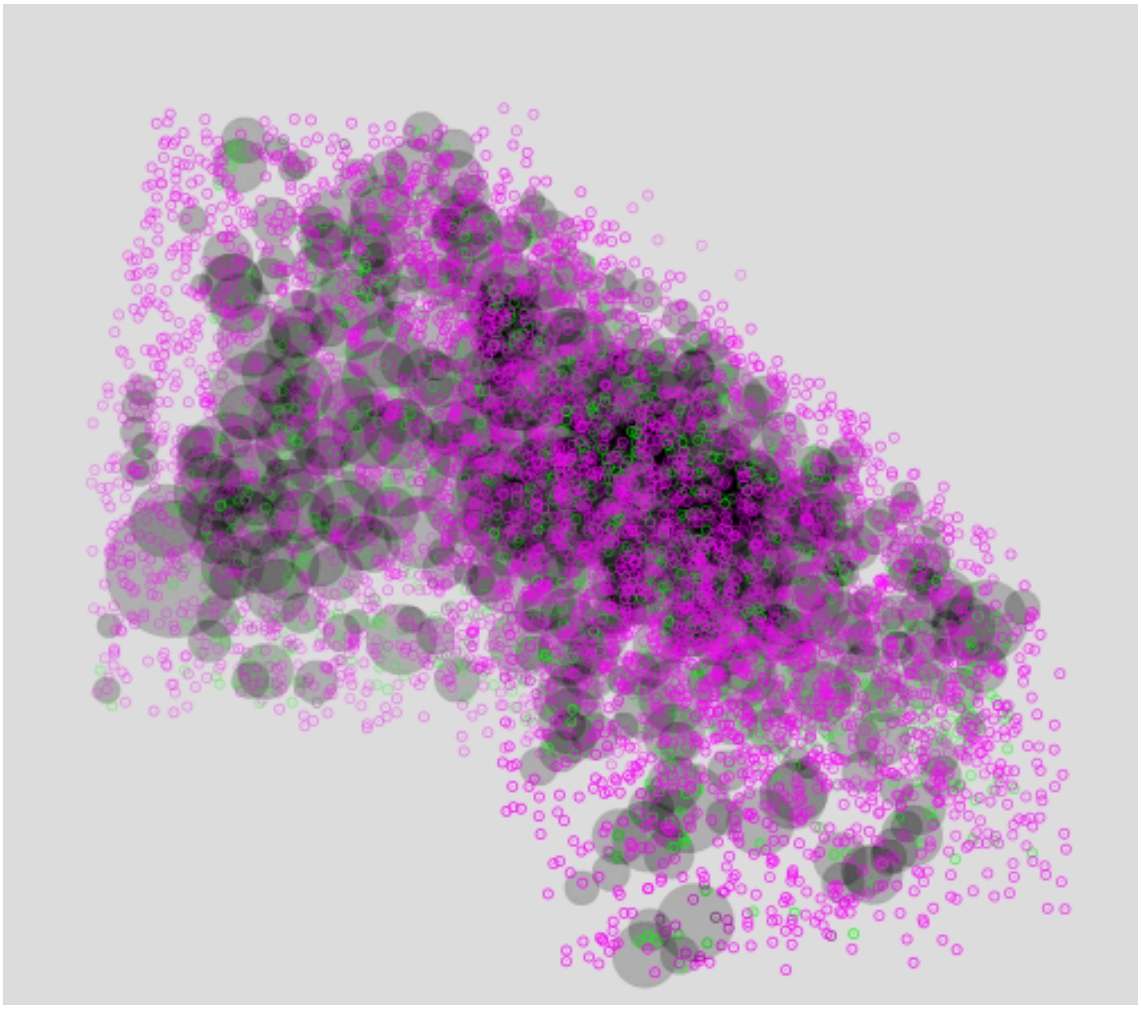

Figure 5.10: Three-dimensional map of the DES light cone; magenta dots show 5% of all redMaPPer clusters, green dots display 5% of redMaPPer clusters inside watershed voids and black spheres of radius r_v represent the spherical volume of each void.

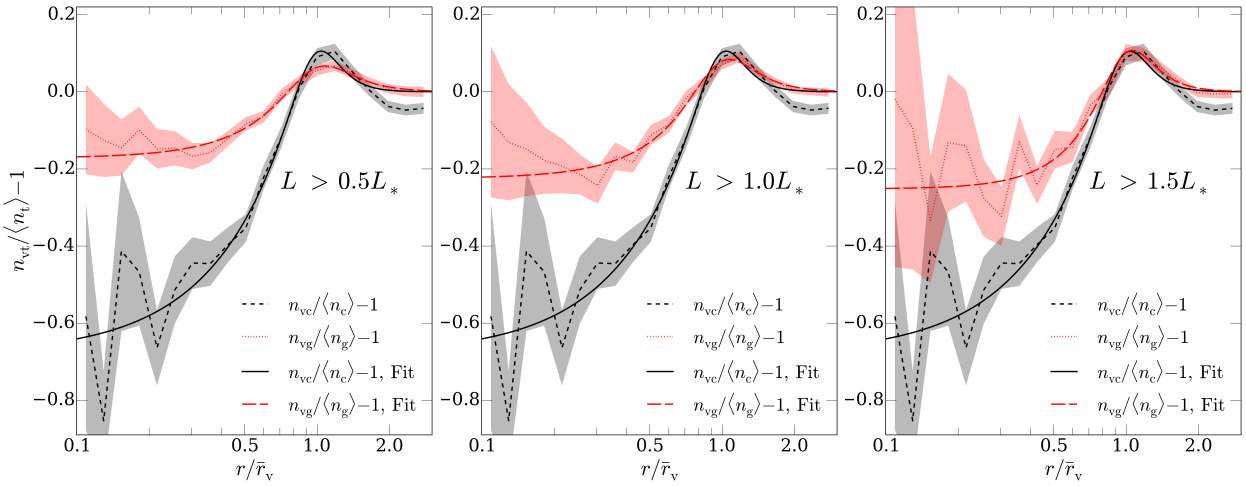

Figure 5.11: Tracer-density profiles (solid black for REDMAPPER clusters, dashed red for REDMAGIC galaxies) around cluster-defined voids of size $40h^{-1}\text{Mpc} < r_v < 80h^{-1}\text{Mpc}$ in the DES data. The luminosity cut for the galaxy sample is varied from left to right, as indicated in each panel.

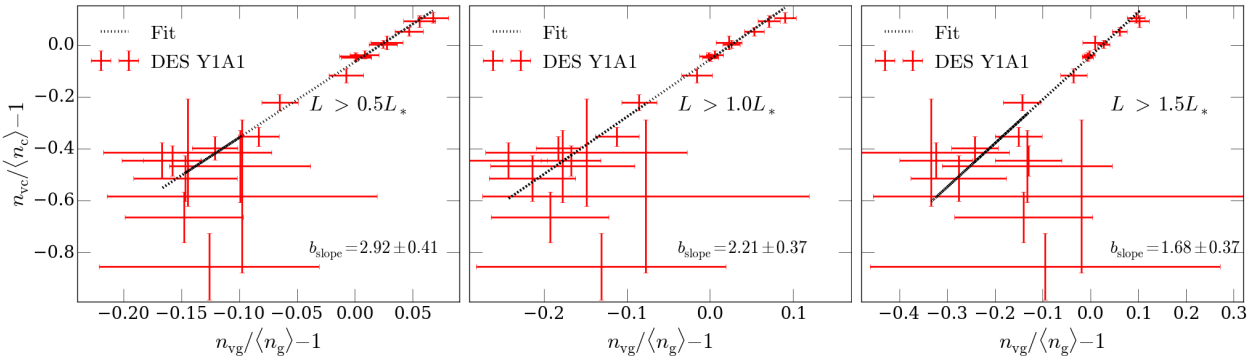

Figure 5.12: Cluster- and galaxy-density profiles from Figure 5.11 plotted against each other. The dotted black line shows the best fit obtained with Equation 5.4.1.

the data points exhibit large scatter. In all cases we find Equation 5.4.1 to provide a satisfactory fit to the data. We find no evidence for any deviation from linearity other than due to statistical noise, which argues Equation 5.4.1 to indeed be the simplest and most conservative model that is consistent with the data. Our earlier results based on simulations and mocks with much better statistics corroborate this result. We further confirm a decrease in the best-fit value of the slope b_{slope}, caused by an increase in the bias of the galaxy samples with increasing luminosity cuts. At the same time, the offsets c_{offset} remain consistent with zero. The detailed parameter constraints are reported in Table 5.4.

Finally, we test the convergence of b_{slope} to the linear relative bias b_{rel} of the employed tracers. Due to the relatively low number of voids in our sample, we can only afford to have two independent bins in effective radius. We choose to split the sample such that both bins roughly contain the same number of voids, with $r_v < 40h^{-1}\text{Mpc}$

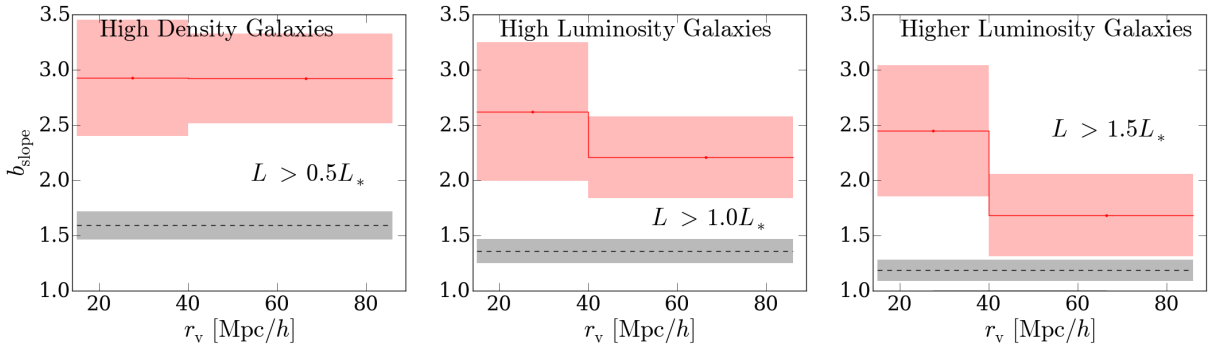

Figure 5.13: Best-fit values for $b_{\rm slope}$ (solid red) as a function of void radius in DES data. The luminosity cut for the galaxy sample varies from left to right, as indicated in each panel. Dashed black lines show the linear relative bias between clusters and galaxies, estimated via their angular power spectra on large scales.

and $r_{\rm v} > 40h^{-1}$Mpc. The corresponding best-fit values of $b_{\rm slope}$ are shown as the red dots, connected by a solid line in Figure 5.13 (which is analogous to Figure 5.7 albeit with DES data). In comparison, the linear relative bias estimated via the large-scale clustering statistics of the tracers, as described in Section 5.3.3, is shown in dashed black. Evidently, the poor statistics in the measurement do not allow any detailed conclusions about the convergence properties of $b_{\rm slope}$ towards $b_{\rm rel}$. However, at least for the galaxy samples of high and higher luminosity, an indication for a decrease in $b_{\rm slope}$ at larger $r_{\rm v}$ is apparent. A more detailed investigation of this will be possible with future DES tracer catalogues of larger size. The final DES Y5 tracer catalogues will provide similar statistics as the MICE 2 mocks employed above.

5.5 CONCLUSIONS

The aim of this Chapter's analysis was to probe the nature of tracer bias in void environments, a regime of large-scale structure that so far has little been investigated specifically for this purpose [however, see 142, 150, 222]. In contrast, the overall tracer bias, which is typically weighted towards the most overdense structures in the Universe, has remained an active topic of research for a long time, due to its complex non-linear behaviour on intermediate and small scales [e.g., 35, 68, 193, 194, 200, and references therein]. Moreover, recent evidence for additional stochasticity beyond the Poisson expectation in the clustering properties of galaxies and clusters further complicates the common treatment of bias [e.g. 11, 81, 90, 93, 148]. A consistent and reliable framework for the modelling of tracer bias is indispensable for the cosmological analysis of modern data sets of large-scale structure, because it establishes a connection between its observable luminous constituents and the invisible dark matter. As the latter is expected to be responsible for more than 80% of the mass content in

Table 5.4: Best-fit values and 1σ uncertainties on the parameters of Equation 5.4.1 for cluster-defined voids of various size and for different luminosity cuts in the galaxy sample from the DES data.

Voids	REDMAGIC ($L > 0.5L_*$)		REDMAGIC ($L > 1.0L_*$)		REDMAGIC ($L > 1.5L_*$)	
Bins in r_v [h^{-1}Mpc]	b_{slope}	c_{offset}	b_{slope}	c_{offset}	b_{slope}	c_{offset}
$15 < r_v < 40$	2.92 ± 0.53	-0.055 ± 0.122	2.62 ± 0.62	-0.038 ± 0.145	2.45 ± 0.59	-0.027 ± 0.138
$40 < r_v < 86$	2.91 ± 0.40	-0.065 ± 0.083	2.21 ± 0.37	-0.056 ± 0.084	1.68 ± 0.37	-0.043 ± 0.095

the Universe, the accuracy of cosmological constraints is often limited by the degree to which tracer bias is understood.

Summary of the conclusions

In this work we have investigated tracer bias in void environments of the distribution of galaxy clusters, based on a complete pipeline of hydrodynamical simulations, mocks, and data from the first year of DES observations. We find a remarkably linear relationship between the void-centric density fluctuations of clusters and galaxy samples of various magnitude limits across all distance scales, suggesting tracer bias to remain linear in the two-point statistics of void environments. This confirms the simulation results by Pollina et al. [165] presented in Chapter 4, but for the first time with observational data. We show that the relative clustering amplitude between any two tracers can be expressed by a single multiplicative constant b_{slope}, relating their void-tracer cross-correlation functions according to Equation 5.4.1 with an offset consistent with zero ($c_{offset} = 0$). However, the constant b_{slope} coincides with the linear relative bias b_{rel} between those tracers only when voids above a certain critical effective radius r_v^+ are used in this measurement. In case of very sparse void tracers, such as the galaxy clusters used here, the value of r_v^+ may exceed the available range of void sizes in a given area on the sky. For smaller voids, b_{slope} increases towards lower r_v.

A detailed model for this behaviour can be important in cases where the absolute value of tracer bias is needed to obtain parameter constraints, which goes beyond the scope of this analysis. It has been pointed out that tracer environment can be more relevant than host-halo mass to determine the bias of tracers [1, 168, 192], and we expect the environmental constraint from voids to be important in this respect. When tracers are selected above some mass or luminosity threshold, as done here, they are typically more biased in void environments than elsewhere in the cosmic web [150, 222]. Conversely, selecting the most extreme environments as tracers of the density field, such as the centres of voids, can lead to a vanishing, or even negative clustering bias [51, 94]. Nevertheless, the fact that tracer bias can be treated linearly with a single free parameter significantly simplifies most common two-point clustering analyses of large-scale structure. For example, it implies that different tracer-density profiles around

Discussion

voids can be described with the same universal functional form [as provided by Equation 5.3.4, 92, 207]. The analysis we presented is arguably the best approach to test such a function, as with observational data we do not have access to the entire three-dimensional distribution of luminous and dark matter. Furthermore, the presented method can be augmented with measurements of tangential shear around voids, which provides the projected surface-mass density excess between weakly lensed source galaxies and the observer. Shape catalogues of the galaxies in DES are available, a study of the absolute tracer bias with respect to the underlying dark matter distribution in void environments is underway (Fang et al., in prep.). Our conclusions are further in excellent agreement with recent analyses of weak lensing by troughs in the projected galaxy distribution [89, 90], which can be accurately modelled using linear bias [81]. While those results argue for a non-vanishing stochasticity parameter to be important for the counts-in-cells statistic, this does not apply to cross-correlation functions (as employed in this Chapter's analysis), where stochasticity does not enter at non-zero separation.

As a side product, we have constructed the first catalogue of 3D-watershed voids that are solely based on photometric redshift measurements with a controlled photo-z uncertainty.[7] Another element of novelty in our approach is that we employ galaxy clusters, rather than single galaxies, as tracers for void finding. In fact, our tests with mocks indicate that while the accuracy of redMaGiC redshift estimates for single galaxies is not sufficient to match void number counts from a spectroscopic survey, redMaPPer clusters produce remarkably similar void abundances among spec-z and photo-z catalogues. The flip side of using clusters rather than galaxies as void tracers is that they can only access fewer and larger voids, due to their sparsity. Nevertheless, for our purposes this constitutes also an advantage, as the relative impact of photo-z scatter becomes even smaller for large voids. Furthermore, the high number of clusters accessible in photometric surveys opens up a promising perspective for void science in the future. In fact forthcoming surveys, such as LSST [103] and EUCLID [116], will partially rely on photometric redshift estimates. The effort to fully exploit these kind of data in the context of void studies will thereby benefit from our analysis.

7 [87] have already extracted a 3D void catalogue from SDSS photometry, but analysed it in projection to study ISW imprints.

6

GENERAL CONCLUSION AND FUTURE OUTLOOK

In this Chapter we revise all conclusions and give a brief outlook on possible future developments of our work.

We are living a very exciting and - at the same time - very puzzling epoch for Cosmology. On one hand, the success of the current concordance model is astonishing, as, with only six parameter, we are able to describe nothing less than the whole Universe, at nearly all scales and times, implying that the physics knowledge that we currently have is sufficient to phenomenologically describe $\approx$ 14 Gyr of Universe evolution. On the other hand, considering all the evidence we have gathered until now, it seems indisputable that only $\approx$ 5% of what constitutes the Universe is made of matter known from a fundamental point of view. Roughly 25% of our Cosmos is made of dark matter, which is constituted of particles that do not belong to the current Standard Model of particle physics. The remaining $\approx$ 70% is a real conundrum: it behaves like a uniformly distributed fluid of unknown nature with an unusual Equation of State ($w = -1$), and it is responsible for the late time accelerated expansion, from which the name "Dark Energy" . Thus, while we live in the "Precision Cosmology" epoch of ΛCDM (that is, we can measure with great precision the six parameters that it relies on), the quest to understand the nature of the effectiveness of this model is still wide open.

One of the possible ways to investigate the essence of dark energy and dark matter is provided by the study of the large scale structure of the Universe. In fact, because the field equation of General Relativity relates the matter and energy content of the Universe with the geometry of the space-time, observations of the expansion history of the Cosmos allow us to infer the content of its components (see Chapter 1).

Typically, the expansion of the Universe can be studied employing standard candles or standard rulers. For example, by using SNIa as standard candles, the accelerated expansion of the Universe was discovered in the first place, calling for the introduction of a Dark Energy. Because this accelerated expansion acts as a sort of anti-gravity, such discovery might tell us something about our understanding of gravitation, which is assumed to follow GR all-over the Universe, although Einstein's Theory of Gravity has not been tested on very large scales.

The nature of Dark Energy (or of possible modification of the GR) has been studied for decades via its impact on the statistics of the large scale structure of the Universe (Chapter 2). This has been mostly

done relying on the statistics of the most massive components of the LSS - galaxy clusters. In recent years, though, a significant fraction of the sky has been mapped, allowing to access the less visible and largest constituent of the LSS - cosmic voids.

Utilizing a rather theoretical approach, voids have been extensively studied as under-densities of the dark matter: many theoretical works agree that void statistics are sensitive to different kind of competing dark energy models (or to modification of gravity) only if voids can be directly traced and studied in the spatial distribution of the CDM. This can be done with the help of synthetic Universes, created using large numerical simulations, where it is possible to access the location of a each single CDM particle. Unfortunately, in practice, this is not possible. In fact, although we can measure the effect of the dark matter mass on its surroundings, a dark matter particle cannot be directly observed by definition. For observational studies we have to rely on the tiny fraction of baryons in the Cosmos, which is visible to our telescopes. Regular matter is hosted in galaxies and clusters of galaxies, that are observable tracers of the dark matter. These tracers are not fully representative of the dark matter mass: as they arise from the highest peaks of the matter density field they do not smoothly map its distribution. Visible structures are thereby biased tracers of the matter.

This dissertation aims at investigating how the properties of voids traced within the density field of luminous galaxies might be altered, and how this might impact their potential to constrain cosmology.

In Chapter 3 we demonstrate, by means of a set of simulations of competing cosmological models, that halo bias has the power to wash out possible deviation from ΛCDM in void statistics. To disentangle the impact of sample-sparsity from that of halo-bias, we repeat our analysis twice: employing as void-tracers firstly only haloes and secondly only CDM-particles (diluted to the same density as haloes). The deviations of competing models from ΛCDM, striking when CDM particles are used as void-tracers, vanish if voids are traced in the collapsed halo sample. This result challenges the claimed potential of voids to improve our knowledge on the nature of dark energy, if bias is not properly modelled.

In Chapter 4 we make a first attempt at understanding which relation occurs between matter over-densities and tracer over-density within voids. With the help of hydro-dynamical simulations we conclude that, within void environment, this relation is always linear: we can in fact link the tracer density to the underlying matter density via a single multiplicative constant. Such multiplicative constant has the same value as the linear bias for the largest voids in the sample, while for smaller voids has a higher value.

This result validates the assumption of utilizing the linear bias to study the redshift space distortion around voids, and corroborates the creation of solid framework to use voids for cosmological purposes. Furthermore, simply relying on the linear bias value to re-scale the density of the under-dense fluctuations, Ronconi and Marulli [178] were able to extend a theoretical model to forecast void abundances in the mass to void traced in the halo sample extracted from N-body simulations. This was so far one of the nicest gains we had from the simple result presented in Chapter 4.

Another possible test of this results is provided by void-lensing. The first steps in this direction have already been taken within the DES collaboration. Fang et al. (in prep.) is investigating the lensing profile around DES voids, to establish whether this is linearly related to the density profiles of tracer-voids projected along the line of sight. This test might further validate Equation 4.4.1.

Once a clear method to study Equation 4.4.1 with data is established, we could use it to test gravity and the impact of massive neutrinos in our universe. In fact, both these models present a scale-dependence of linear bias, which should break the linear relation and give us evidence of the impact of neutrinos or possible modification of gravity on Cosmology.

A first attempt to test Equation 4.4.1 in observation was presented in Chapter 5. We analyse data by the Dark Energy Survey, currently the largest LSS survey available. The three-dimensional distribution of matter in the Universe is not directly observable, therefore, for this first observational test, we rely on the relative properties of voids traced with highly biased clusters of galaxies and that of the galaxy-sample. We show that the linearity in this case also holds. Furthermore, we are able to assess that tracing voids using clusters of galaxies rather then single galaxies mitigates photometric uncertainty. This is a remarkably useful result. Combining it with that of Ronconi and Marulli [178], one should be able in principle to infer the abundances of voids in present and future surveys that will rely on photometry, enhancing their constraining power on cosmology [157].

In the near and far future a wide variety of new observations will be available. DES has entered its 5th and last year of observations, at the end of which it will have scanned roughly 5000 square degree of the southern sky. In the next decade the Large Synoptic Survey Telescope Ivezic et al. [LSST 103] and the Euclid mission [116] will bring a tremendous amount of new information, screening an area three times larger than the DES survey. Both these experiments will at least partially rely on a photometric estimate of galaxy redshifts. Therefore, these collaborations might benefit from engaging a similar approach to that presented in Chapter 5 for voids studies.

Finally, it can be argued whether focussing on void-centric statistics might lead to other general improvements when analysing data from

photometric surveys. In this context one might study e. g. a void-centric cluster-cluster correlation function (rather than a full sample cluster-cluster correlation function), as this might alleviate for the impact of photometric uncertainty without relying on tomographic shells.

All of these possible intriguing outcomes shall be further investigated in the months and years to come.

BIBLIOGRAPHY

[1] U. Abbas and R. K. Sheth. „Strong clustering of underdense regions and the environmental dependence of clustering from Gaussian initial conditions“. In: *MNRAS* 378 (June 2007), pp. 641–648. DOI: 10.1111/j.1365-2966.2007.11806.x. eprint: astro-ph/0703391.

[2] T. M. C. Abbott et al. „The Dark Energy Survey Data Release 1“. In: *ArXiv e-prints* (Jan. 2018). arXiv: 1801.03181 [astro-ph.IM].

[3] I. Achitouv, M. Neyrinck, and A. Paranjape. „Testing spherical evolution for modelling void abundances“. In: *MNRAS* 451 (Aug. 2015), pp. 3964–3974. DOI: 10.1093/mnras/stv1228. arXiv: 1309.3799.

[4] I. Achitouv, C. Blake, P. Carter, J. Koda, and F. Beutler. „Consistency of the growth rate in different environments with the 6-degree Field Galaxy Survey: Measurement of the void-galaxy and galaxy-galaxy correlation functions“. In: *Phys. Rev. D* 95.8, 083502 (Apr. 2017), p. 083502. DOI: 10.1103/PhysRevD.95.083502. arXiv: 1606.03092.

[5] Ixandra Achitouv, Marco Baldi, Ewald Puchwein, and Jochen Weller. „The Imprint of f(R) Gravity on Non-Linear Structure Formation“. In: *arXiv:1511.01494* (2015). arXiv: 1511.01494 [astro-ph.CO].

[6] C. Alcock and B. Paczynski. „An evolution free test for non-zero cosmological constant“. In: *Nature* 281 (Oct. 1979), p. 358. DOI: 10.1038/281358a0.

[7] L. Amendola. „Linear and nonlinear perturbations in dark energy models“. In: *Phys. Rev. D* 69.10 (May 2004), pp. 103524–+. DOI: 10.1103/PhysRevD.69.103524. eprint: arXiv:astro-ph/0311175.

[8] L. Amendola et al. „Cosmology and Fundamental Physics with the Euclid Satellite“. In: *Living Reviews in Relativity* 16 (Sept. 2013), p. 6. DOI: 10.12942/lrr-2013-6. arXiv: 1206.1225 [astro-ph.CO].

[9] Luca Amendola. „Coupled quintessence“. In: *Phys. Rev.* D62 (2000), p. 043511. DOI: 10.1103/PhysRevD.62.043511. arXiv: astro-ph/9908023.

[10] Luca Amendola. „Linear and non-linear perturbations in dark energy models“. In: *Phys. Rev.* D69 (2004), p. 103524. DOI: 10.1103/PhysRevD.69.103524. arXiv: astro-ph/0311175.

[11] T. Baldauf, U. Seljak, R. E. Smith, N. Hamaus, and V. Desjacques. „Halo stochasticity from exclusion and nonlinear clustering“. In: *Phys. Rev. D* 88.8, 083507 (Oct. 2013), p. 083507. DOI: 10.1103/PhysRevD.88.083507. arXiv: 1305.2917 [astro-ph.CO].

[12] M. Baldi. *Interaction Between Dark Energy and Dark Matter*. Feb. 2009, p. 153.

[13] M. Baldi. „The CoDECS project: a publicly available suite of cosmological N-body simulations for interacting dark energy models“. In: *ArXiv e-prints* (Sept. 2011). arXiv: 1109.5695 [astro-ph.CO].

[14] M. Baldi. „The CoDECS project: a publicly available suite of cosmological N-body simulations for interacting dark energy models“. In: *MNRAS* 422 (May 2012), pp. 1028–1044. DOI: 10.1111/j.1365-2966.2012.20675.x. arXiv: 1109.5695 [astro-ph.CO].

[15] Marco Baldi. „Clarifying the effects of interacting dark energy on linear and non-linear structure formation processes“. In: *MNRAS* 414 (June 2011), pp. 116–128. DOI: 10.1111/j.1365-2966.2011.18263.x. arXiv: 1012.0002 [astro-ph.CO].

[16] Marco Baldi. „Time-dependent couplings in the dark sector: from background evolution to non-linear structure formation“. In: *MNRAS* 411 (Feb. 2011), pp. 1077–1103. DOI: 10.1111/j.1365-2966.2010.17758.x. arXiv: 1005.2188 [astro-ph.CO].

[17] Marco Baldi. „Early massive clusters and the bouncing coupled dark energy“. In: *MNRAS* 420 (Feb. 2012), pp. 430–440. DOI: 10.1111/j.1365-2966.2011.20048.x. arXiv: 1107.5049 [astro-ph.CO].

[18] Marco Baldi, V. Pettorino, G. Robbers, and V. Springel. „Hydrodynamical N-body simulations of coupled dark energy cosmologies“. In: *MNRAS* 403 (Apr. 2010), pp. 1684–1702. DOI: 10.1111/j.1365-2966.2009.15987.x.

[19] A. Banerjee and N. Dalal. „Simulating nonlinear cosmological structure formation with massive neutrinos“. In: *ArXiv e-prints* (June 2016). arXiv: 1606.06167.

[20] J. M. Bardeen, J. R. Bond, N. Kaiser, and A. S. Szalay. „The statistics of peaks of Gaussian random fields“. In: *ApJ* 304 (May 1986), pp. 15–61. DOI: 10.1086/164143.

[21] A. Barreira, M. Cautun, B. Li, C. M. Baugh, and S. Pascoli. „Weak lensing by voids in modified lensing potentials“. In: *J. Cosmology Astropart. Phys.* 8, 028 (Aug. 2015), p. 28. DOI: 10.1088/1475-7516/2015/08/028. arXiv: 1505.05809.

[22] F. Bernardeau. „The nonlinear evolution of rare events“. In: *ApJ* 427 (May 1994), pp. 51–71. DOI: 10.1086/174121. eprint: astro-ph/9311066.

[23] E. Bertschinger. „The self-similar evolution of holes in an Einstein-de Sitter universe“. In: *ApJS* 58 (May 1985), pp. 1–37. DOI: 10.1086/191027.

[24] F. Beutler et al. „The clustering of galaxies in the completed SDSS-III Baryon Oscillation Spectroscopic Survey: Anisotropic galaxy clustering in Fourier-space“. In: *ArXiv e-prints* (July 2016). arXiv: 1607.03150.

[25] Emma Beynon, Marco Baldi, David J. Bacon, Kazuya Koyama, and Cristiano Sabiu. „Weak lensing predictions for coupled dark energy cosmologies at non-linear scales“. In: *Mon.Not.Roy.Astron.Soc.* 422 (2012), pp. 3546–3553. arXiv: 1111.6974 [astro-ph.CO].

[26] D. Blas, J. Lesgourgues, and T. Tram. „The Cosmic Linear Anisotropy Solving System (CLASS). Part II: Approximation schemes“. In: *J. Cosmology Astropart. Phys.* 7, 034 (July 2011), p. 034. DOI: 10.1088/1475-7516/2011/07/034. arXiv: 1104.2933.

[27] G. R. Blumenthal, L. N. da Costa, D. S. Goldwirth, M. Lecar, and T. Piran. „The largest possible voids“. In: *ApJ* 388 (Apr. 1992), pp. 234–241. DOI: 10.1086/171147.

[28] S. Bocquet, A. Saro, K. Dolag, and J. J. Mohr. „Halo mass function: baryon impact, fitting formulae, and implications for cluster cosmology“. In: *MNRAS* 456 (Mar. 2016), pp. 2361–2373. DOI: 10.1093/mnras/stv2657. arXiv: 1502.07357.

[29] J. R. Bond, L. Kofman, and D. Pogosyan. „How filaments of galaxies are woven into the cosmic web“. In: *Nature* 380 (Apr. 1996), pp. 603–606. DOI: 10.1038/380603a0. eprint: astro-ph/9512141.

[30] J. R. Bond, S. Cole, G. Efstathiou, and N. Kaiser. „Excursion set mass functions for hierarchical Gaussian fluctuations“. In: *ApJ* 379 (Oct. 1991), pp. 440–460. DOI: 10.1086/170520.

[31] E. G. P. Bos, R. van de Weygaert, K. Dolag, and V. Pettorino. „The darkness that shaped the void: dark energy and cosmic voids“. In: *MNRAS* 426 (Oct. 2012), pp. 440–461. DOI: 10.1111/j.1365-2966.2012.21478.x. arXiv: 1205.4238 [astro-ph.CO].

[32] M. Boylan-Kolchin, J. S. Bullock, and M. Kaplinghat. „Too big to fail? The puzzling darkness of massive Milky Way subhaloes“. In: *MNRAS* 415 (July 2011), pp. L40–L44. DOI: 10.1111/j.1745-3933.2011.01074.x. arXiv: 1103.0007 [astro-ph.CO].

[33] P. H. Brax and J. Martin. „Quintessence and supergravity“. In: *Physics Letters B* 468 (Nov. 1999), pp. 40–45. DOI: 10.1016/S0370-2693(99)01209-5. eprint: arXiv:astro-ph/9905040.

[34] J. S. Bullock. „Notes on the Missing Satellites Problem“. In: *ArXiv e-prints* (Sept. 2010). arXiv: 1009.4505 [astro-ph.CO].

[35] M. Cacciato, O. Lahav, F. C. van den Bosch, H. Hoekstra, and A. Dekel. „On combining galaxy clustering and weak lensing to unveil galaxy biasing via the halo model“. In: *MNRAS* 426 (Oct. 2012), pp. 566–587. DOI: 10.1111/j.1365-2966.2012.21762.x. arXiv: 1203.2616.

[36] Y.-C. Cai, N. Padilla, and B. Li. „Testing gravity using cosmic voids“. In: *MNRAS* 451 (July 2015), pp. 1036–1055. DOI: 10.1093/mnras/stv777. arXiv: 1410.1510.

[37] Y.-C. Cai, M. C. Neyrinck, I. Szapudi, S. Cole, and C. S. Frenk. „A Possible Cold Imprint of Voids on the Microwave Background Radiation“. In: *ApJ* 786, 110 (May 2014), p. 110. DOI: 10.1088/0004-637X/786/2/110. arXiv: 1301.6136.

[38] Y.-C. Cai, A. Taylor, J. A. Peacock, and N. Padilla. „Redshift-space distortions around voids“. In: *MNRAS* 462 (Nov. 2016), pp. 2465–2477. DOI: 10.1093/mnras/stw1809. arXiv: 1603.05184.

[39] C. Carbone, M. Petkova, and K. Dolag. „DEMNUni: ISW, Rees-Sciama, and weak-lensing in the presence of massive neutrinos“. In: *J. Cosmology Astropart. Phys.* 7, 034 (July 2016), p. 034. DOI: 10.1088/1475-7516/2016/07/034. arXiv: 1605.02024.

[40] Carmelita Carbone, Marco Baldi, Valeria Pettorino, and Carlo Baccigalupi. „Maps of CMB lensing deflection from N-body simulations in Coupled Dark Energy Cosmologies“. In: *JCAP* 1309 (2013), p. 004. DOI: 10.1088/1475-7516/2013/09/004. arXiv: 1305.0829 [astro-ph.CO].

[41] E. Carlesi, A. Knebe, G. F. Lewis, S. Wales, and G. Yepes. „Hydrodynamical simulations of coupled and uncoupled quintessence models - I. Halo properties and the cosmic web“. In: *MNRAS* 439 (Apr. 2014), pp. 2943–2957. DOI: 10.1093/mnras/stu150. arXiv: 1401.5005 [astro-ph.CO].

[42] E. Carlesi, A. Knebe, G. F. Lewis, and G. Yepes. „Hydrodynamical simulations of coupled and uncoupled quintessence models - II. Galaxy clusters“. In: *MNRAS* 439 (Apr. 2014), pp. 2958–2969. DOI: 10.1093/mnras/stu151. arXiv: 1401.5326 [astro-ph.CO].

[43] Emanuele Castorina, Carmelita Carbone, Julien Bel, Emiliano Sefusatti, and Klaus Dolag. „DEMNUni: the clustering of large-scale structures in the presence of massive neutrinos“. In: *Journal of Cosmology and Astroparticle Physics* 2015.07 (2015), p. 043. URL: http://stacks.iop.org/1475-7516/2015/i=07/a=043.

[44] M. Cautun, E. Paillas, Y.-C. Cai, S. Bose, J. Armijo, B. Li, and N. Padilla. „The Santiago-Harvard-Edinburgh-Durham void comparison I: SHEDding light on chameleon gravity tests“. In: *ArXiv e-prints* (Oct. 2017). arXiv: 1710.01730.

[45] L. Ceccarelli, D. Paz, M. Lares, N. Padilla, and D. G. Lambas. „Clues on void evolution - I. Large-scale galaxy distributions around voids“. In: *MNRAS* 434 (Sept. 2013), pp. 1435–1442. DOI: 10.1093/mnras/stt1097. arXiv: 1306.5798.

[46] V. D. V. Cervantes, F. Marulli, L. Moscardini, M. Baldi, and A. Cimatti. „Exploiting the shift of baryonic acoustic oscillations as a dynamical probe for dark interactions“. In: *ArXiv e-prints* (Dec. 2012). arXiv: 1212.0853 [astro-ph.CO].

[47] G. Chon, A. Challinor, S. Prunet, E. Hivon, and I. Szapudi. „Fast estimation of polarization power spectra using correlation functions“. In: *MNRAS* 350 (May 2004), pp. 914–926. DOI: 10.1111/j.1365-2966.2004.07737.x. eprint: astro-ph/0303414.

[48] C.-H. Chuang, F.-S. Kitaura, Y. Liang, A. Font-Ribera, C. Zhao, P. McDonald, and C. Tao. „Linear redshift space distortions for cosmic voids based on galaxies in redshift space“. In: *Phys. Rev. D* 95.6, 063528 (Mar. 2017), p. 063528. DOI: 10.1103/PhysRevD.95.063528. arXiv: 1605.05352.

[49] J. Clampitt, Y.-C. Cai, and B. Li. „Voids in modified gravity: excursion set predictions“. In: *MNRAS* 431 (May 2013), pp. 749–766. DOI: 10.1093/mnras/stt219. arXiv: 1212.2216 [astro-ph.CO].

[50] J. Clampitt and B. Jain. „Lensing measurements of the mass distribution in SDSS voids“. In: *MNRAS* 454 (Dec. 2015), pp. 3357–3365. DOI: 10.1093/mnras/stv2215. arXiv: 1404.1834.

[51] J. Clampitt, B. Jain, and C. Sánchez. „Clustering and bias measurements of SDSS voids“. In: *MNRAS* 456 (Mar. 2016), pp. 4425–4431. DOI: 10.1093/mnras/stv2933. arXiv: 1507.08031.

[52] J. M. Colberg, R. K. Sheth, A. Diaferio, L. Gao, and N. Yoshida. „Voids in a ΛCDM universe“. In: *MNRAS* 360 (June 2005), pp. 216–226. DOI: 10.1111/j.1365-2966.2005.09064.x. eprint: astro-ph/0409162.

[53] J. M. Colberg et al. „The Aspen-Amsterdam void finder comparison project“. In: *MNRAS* 387 (June 2008), pp. 933–944. DOI: 10.1111/j.1365-2966.2008.13307.x. arXiv: 0803.0918.

[54] P. Coles and F. Lucchin. *Cosmology: The Origin and Evolution of Cosmic Structure, Second Edition*. July 2002, p. 512.

[55] M. Crocce, F. J. Castander, E. Gaztañaga, P. Fosalba, and J. Carretero. „The MICE Grand Challenge lightcone simulation - II. Halo and galaxy catalogues“. In: *MNRAS* 453 (Oct. 2015), pp. 1513–1530. DOI: 10.1093/mnras/stv1708. arXiv: 1312.2013.

[56] Weiguang Cui, Marco Baldi, and Stefano Borgani. „The halo mass function in interacting Dark Energy models“. In: *arXiv:1201.3568* (2012). arXiv: 1201.3568 [astro-ph.CO].

[57] G. D'Amico, M. Musso, J. Noreña, and A. Paranjape. „Excursion sets and non-Gaussian void statistics". In: *Phys. Rev. D* 83.2, 023521 (Jan. 2011), p. 023521. DOI: 10.1103/PhysRevD.83.023521. arXiv: 1011.1229 [astro-ph.CO].

[58] DES Collaboration et al. „Dark Energy Survey Year 1 Results: Cosmological Constraints from Galaxy Clustering and Weak Lensing". In: *ArXiv e-prints* (Aug. 2017). arXiv: 1708.01530.

[59] DESI Collaboration et al. „The DESI Experiment Part I: Science,Targeting, and Survey Design". In: *ArXiv e-prints* (Oct. 2016). arXiv: 1611.00036 [astro-ph.IM].

[60] M. Davis and P. J. E. Peebles. „A survey of galaxy redshifts. V - The two-point position and velocity correlations". In: *ApJ* 267 (Apr. 1983), pp. 465–482. DOI: 10.1086/160884.

[61] V. Demchenko, Y.-C. Cai, C. Heymans, and J. A Peacock. „Testing the spherical evolution of cosmic voids". In: *ArXiv e-prints* (May 2016). arXiv: 1605.05286.

[62] E. Di Dio, F. Montanari, J. Lesgourgues, and R. Durrer. „The CLASSgal code for relativistic cosmological large scale structure". In: *J. Cosmology Astropart. Phys.* 11, 044 (Nov. 2013), p. 044. DOI: 10.1088/1475-7516/2013/11/044. arXiv: 1307.1459.

[63] K. Dolag, E. Komatsu, and R. Sunyaev. „SZ effects in the Magneticum Pathfinder Simulation: Comparison with the Planck, SPT, and ACT results". In: *MNRAS* (Aug. 2016). DOI: 10.1093/mnras/stw2035. arXiv: 1509.05134.

[64] K. Dolag, F. Vazza, G. Brunetti, and G. Tormen. „Turbulent gas motions in galaxy cluster simulations: the role of smoothed particle hydrodynamics viscosity". In: *MNRAS* 364 (Dec. 2005), pp. 753–772. DOI: 10.1111/j.1365-2966.2005.09630.x.

[65] K. Dolag, S. Borgani, G. Murante, and V. Springel. „Substructures in hydrodynamical cluster simulations". In: *MNRAS* 399 (Oct. 2009), pp. 497–514. DOI: 10.1111/j.1365-2966.2009.15034.x. arXiv: 0808.3401.

[66] K. Dolag, B. M. Gaensler, A. M. Beck, and M. C. Beck. „Constraints on the distribution and energetics of fast radio bursts using cosmological hydrodynamic simulations". In: *Mon. Not. Roy. Astron. Soc.* 451.4 (2015), pp. 4277–4289. DOI: 10.1093/mnras/stv1190. arXiv: 1412.4829 [astro-ph.CO].

[67] A. Drlica-Wagner et al. „Dark Energy Survey Year 1 Results: The Photometric Data Set for Cosmology". In: *ApJS* 235, 33 (Apr. 2018), p. 33. DOI: 10.3847/1538-4365/aab4f5. arXiv: 1708.01531.

[68] A. Dvornik et al. „Unveiling Galaxy Bias via the Halo Model, KiDS and GAMA". In: *ArXiv e-prints* (Feb. 2018). arXiv: 1802.00734.

[69] G. Efstathiou, W. J. Sutherland, and S. J. Maddox. „The cosmological constant and cold dark matter“. In: *Nature* 348 (1990), pp. 705–707. DOI: 10.1038/348705a0.

[70] Albert Einstein. „On the General Theory of Relativity“. In: *Sitzungsber.Preuss.Akad.Wiss.Berlin (Math.Phys.)* 1915 (1915), pp. 778–786.

[71] Albert Einstein. „Cosmological Considerations in the General Theory of Relativity“. In: *Sitzungsber.Preuss.Akad.Wiss.Berlin (Math.Phys.)* 1917 (1917), pp. 142–152.

[72] V. R. Eke, S. Cole, and C. S. Frenk. „Cluster evolution as a diagnostic for Omega“. In: *MNRAS* 282 (Sept. 1996). DOI: 10.1093/mnras/282.1.263. eprint: astro-ph/9601088.

[73] J. Elvin-Poole et al. „Dark Energy Survey Year 1 Results: Galaxy clustering for combined probes“. In: *ArXiv e-prints* (Aug. 2017). arXiv: 1708.01536.

[74] A. Elyiv, F. Marulli, G. Pollina, M. Baldi, E. Branchini, A. Cimatti, and L. Moscardini. „Cosmic voids detection without density measurements“. In: *MNRAS* 448 (Mar. 2015), pp. 642–653. DOI: 10.1093/mnras/stv043. arXiv: 1410.4559.

[75] B. Falck and M. C. Neyrinck. „The persistent percolation of single-stream voids“. In: *MNRAS* 450 (July 2015), pp. 3239–3253. DOI: 10.1093/mnras/stv879. arXiv: 1410.4751.

[76] G. R. Farrar and P. J. E. Peebles. „Interacting Dark Matter and Dark Energy“. In: *ApJ* 604 (Mar. 2004), pp. 1–11. DOI: 10.1086/381728. eprint: arXiv:astro-ph/0307316.

[77] F. Finelli, J. García-Bellido, A. Kovács, F. Paci, and I. Szapudi. „A Supervoid Explanation of the Cosmic Microwave Background Cold Spot“. In: *IAU Symposium*. Vol. 306. IAU Symposium. May 2014, pp. 153–155. DOI: 10.1017/S1743921314013714.

[78] B. Flaugher et al. „The Dark Energy Camera“. In: *AJ* 150, 150 (Nov. 2015), p. 150. DOI: 10.1088/0004-6256/150/5/150. arXiv: 1504.02900 [astro-ph.IM].

[79] P. Fosalba, M. Crocce, E. Gaztañaga, and F. J. Castander. „The MICE grand challenge lightcone simulation - I. Dark matter clustering“. In: *MNRAS* 448 (Apr. 2015), pp. 2987–3000. DOI: 10.1093/mnras/stv138. arXiv: 1312.1707.

[80] A. Friedman. „On the curvature of space“. In: *Z. Phys.* 10 (1922), pp. 377–386. DOI: 10.1007/BF01332580.

[81] O. Friedrich et al. „Density split statistics: joint model of counts and lensing in cells“. In: *ArXiv e-prints* (Oct. 2017). arXiv: 1710.05162.

[82] J. N. Fry and E. Gaztanaga. „Biasing and hierarchical statistics in large-scale structure“. In: *ApJ* 413 (Aug. 1993), pp. 447–452. DOI: 10.1086/173015. eprint: astro-ph/9302009.

[83] Walker A. G. „On Milne's Theory of World Structure“. In: *Proceedings of the London Mathematical Society* s2-42.1 (), pp. 90–127. DOI: 10.1112/plms/s2-42.1.90. eprint: https://londmathsoc.onlinelibrary.wiley.com/doi/pdf/10.1112/plms/s2-42.1.90. URL: https://londmathsoc.onlinelibrary.wiley.com/doi/abs/10.1112/plms/s2-42.1.90.

[84] G. W. Gibbons, M. C. Werner, N. Yoshida, and S. Chon. „On de Sitter geometry in cosmic void statistics“. In: *MNRAS* 438 (Feb. 2014), pp. 1603–1610. DOI: 10.1093/mnras/stt2298. arXiv: 1308.5743 [astro-ph.CO].

[85] Carlo Giocoli, Federico Marulli, Marco Baldi, Lauro Moscardini, and R. Benton Metcalf. „Characterizing dark interactions with the halo mass accretion history and structural properties“. In: *arXiv:1301.3151* (2013). arXiv: 1301.3151 [astro-ph.CO].

[86] Carlo Giocoli, R. Benton Metcalf, Marco Baldi, Massimo Meneghetti, Lauro Moscardini, et al. „Disentangling dark sector models using weak lensing statistics“. In: (2015). arXiv: 1502.03442 [astro-ph.CO].

[87] B. R. Granett, M. C. Neyrinck, and I. Szapudi. „An Imprint of Superstructures on the Microwave Background due to the Integrated Sachs-Wolfe Effect“. In: *ApJ* 683, L99 (Aug. 2008), p. L99. DOI: 10.1086/591670. arXiv: 0805.3695.

[88] S. A. Gregory, L. A. Thompson, and W. G. Tifft. „The Perseus/Pisces Supercluster“. In: *Bulletin of the American Astronomical Society*. Vol. 10. Bulletin of the American Astronomical Society. Sept. 1978, p. 622.

[89] D. Gruen et al. „Weak lensing by galaxy troughs in DES Science Verification data“. In: *MNRAS* 455 (Jan. 2016), pp. 3367–3380. DOI: 10.1093/mnras/stv2506. arXiv: 1507.05090.

[90] D. Gruen et al. „Density split statistics: Cosmological constraints from counts and lensing in cells in DES Y1 and SDSS“. In: *ArXiv e-prints* (Oct. 2017). arXiv: 1710.05045.

[91] N. Hamaus. *Cosmic Voids*. 2017, p. 41.

[92] N. Hamaus, P. M. Sutter, and B. D. Wandelt. „Universal Density Profile for Cosmic Voids“. In: *Physical Review Letters* 112.25, 251302 (June 2014), p. 251302. DOI: 10.1103/PhysRevLett.112.251302. arXiv: 1403.5499.

[93] N. Hamaus, U. Seljak, V. Desjacques, R. E. Smith, and T. Baldauf. „Minimizing the stochasticity of halos in large-scale structure surveys“. In: *Phys. Rev. D* 82.4, 043515 (Aug. 2010), p. 043515. DOI: 10.1103/PhysRevD.82.043515. arXiv: 1004.5377.

[94] N. Hamaus, B. D. Wandelt, P. M. Sutter, G. Lavaux, and M. S. Warren. „Cosmology with Void-Galaxy Correlations“. In: *Physical Review Letters* 112.4, 041304 (Jan. 2014), p. 041304. DOI: 10.1103/PhysRevLett.112.041304. arXiv: 1307.2571 [astro-ph.CO].

[95] N. Hamaus, P. M. Sutter, G. Lavaux, and B. D. Wandelt. „Probing cosmology and gravity with redshift-space distortions around voids“. In: *J. Cosmology Astropart. Phys.* 11, 036 (Nov. 2015), p. 036. DOI: 10.1088/1475-7516/2015/11/036. arXiv: 1507.04363.

[96] N. Hamaus, A. Pisani, P. M. Sutter, G. Lavaux, S. Escoffier, B. D. Wandelt, and J. Weller. „Constraints on Cosmology and Gravity from the Dynamics of Voids“. In: *Physical Review Letters* 117.9, 091302 (Aug. 2016), p. 091302. DOI: 10.1103/PhysRevLett.117.091302. arXiv: 1602.01784.

[97] N. Hamaus, M.-C. Cousinou, A. Pisani, M. Aubert, S. Escoffier, and J. Weller. „Multipole analysis of redshift-space distortions around cosmic voids“. In: *J. Cosmology Astropart. Phys.* 7, 014 (July 2017), p. 014. DOI: 10.1088/1475-7516/2017/07/014. arXiv: 1705.05328.

[98] M. A. Hausman, D. W. Olson, and B. D. Roth. „The evolution of voids in the expanding universe“. In: *ApJ* 270 (July 1983), pp. 351–359. DOI: 10.1086/161128.

[99] A. J. Hawken, D. Michelett, B. Granett, A. Iovino, and L. Guzzo. „Measuring the growth rate of structure around cosmic voids“. In: *The Zeldovich Universe: Genesis and Growth of the Cosmic Web*. Ed. by R. van de Weygaert, S. Shandarin, E. Saar, and J. Einasto. Vol. 308. IAU Symposium. Oct. 2016, pp. 571–574. DOI: 10.1017/S1743921316010590.

[100] M. Hirschmann, K. Dolag, A. Saro, L. Bachmann, S. Borgani, and A. Burkert. „Cosmological simulations of black hole growth: AGN luminosities and downsizing“. In: *MNRAS* 442 (Aug. 2014), pp. 2304–2324. DOI: 10.1093/mnras/stu1023. arXiv: 1308.0333.

[101] K. Honscheid, D. L. DePoy, and for the DES Collaboration. „The Dark Energy Camera (DECam)“. In: *ArXiv e-prints* (Oct. 2008). arXiv: 0810.3600.

[102] Edwin Hubble. „A relation between distance and radial velocity among extra-galactic nebulae“. In: *Proc.Nat.Acad.Sci.* 15 (1929), pp. 168–173.

[103] Z. Ivezic et al. „LSST: from Science Drivers to Reference Design and Anticipated Data Products“. In: *ArXiv e-prints* (May 2008). arXiv: 0805.2366.

[104] K. Izumi, C. Hagiwara, K. Nakajima, T. Kitamura, and H. Asada. „Gravitational lensing shear by an exotic lens object with negative convergence or negative mass“. In: *Phys. Rev. D* 88.2, 024049 (July 2013), p. 024049. DOI: 10.1103/PhysRevD.88.024049. arXiv: 1305.5037 [gr-qc].

[105] E. Jennings, Y. Li, and W. Hu. „The abundance of voids and the excursion set formalism“. In: *MNRAS* 434 (Sept. 2013), pp. 2167–2181. DOI: 10.1093/mnras/stt1169. arXiv: 1304.6087.

[106] N. Kaiser. „On the spatial correlations of Abell clusters“. In: *ApJ* 284 (Sept. 1984), pp. L9–L12. DOI: 10.1086/184341.

[107] R. Kessler et al. „The Difference Imaging Pipeline for the Transient Search in the Dark Energy Survey“. In: *AJ* 150, 172 (Dec. 2015), p. 172. DOI: 10.1088/0004-6256/150/6/172. arXiv: 1507.05137 [astro-ph.IM].

[108] R. P. Kirshner, A. Oemler Jr., P. L. Schechter, and S. A. Shectman. „A million cubic megaparsec void in Bootes“. In: *ApJ* 248 (Sept. 1981), pp. L57–L60. DOI: 10.1086/183623.

[109] E. Komatsu. *Element of Cosmology*. Mar. 2011, p. 102.

[110] E. Komatsu et al. „Seven-year Wilkinson Microwave Anisotropy Probe (WMAP) Observations: Cosmological Interpretation“. In: *ApJS* 192, 18 (Feb. 2011), p. 18. DOI: 10.1088/0067-0049/192/2/18. arXiv: 1001.4538 [astro-ph.CO].

[111] A. Kovács. „The part and the whole: voids, supervoids, and their ISW imprint“. In: *MNRAS* 475 (Apr. 2018), pp. 1777–1790. DOI: 10.1093/mnras/stx3213. arXiv: 1701.08583.

[112] A. Kovács et al. „Imprint of DES superstructures on the cosmic microwave background“. In: *MNRAS* 465 (Mar. 2017), pp. 4166–4179. DOI: 10.1093/mnras/stw2968. arXiv: 1610.00637.

[113] K. Kovač et al. „zCOSMOS 20k: satellite galaxies are the main drivers of environmental effects in the galaxy population at least to z
0.7“. In: *MNRAS* 438 (Feb. 2014), pp. 717–738. DOI: 10.1093/mnras/stt2241. arXiv: 1307.4402 [astro-ph.CO].

[114] E. Krause, T.-C. Chang, O. Doré, and K. Umetsu. „The Weight of Emptiness: The Gravitational Lensing Signal of Stacked Voids“. In: *ApJ* 762, L20 (Jan. 2013), p. L20. DOI: 10.1088/2041-8205/762/2/L20. arXiv: 1210.2446 [astro-ph.CO].

[115] S. D. Landy and A. S. Szalay. „Bias and variance of angular correlation functions“. In: *ApJ* 412 (July 1993), pp. 64–71. DOI: 10.1086/172900.

[116] R. Laureijs et al. „Euclid Definition Study Report“. In: *ArXiv e-prints* (Oct. 2011). arXiv: 1110.3193 [astro-ph.CO].

[117] G. Lavaux and B. D. Wandelt. „Precision cosmology with voids: definition, methods, dynamics“. In: *MNRAS* 403 (Apr. 2010), pp. 1392–1408. DOI: 10.1111/j.1365-2966.2010.16197.x. arXiv: 0906.4101.

[118] Jounghun Lee and Marco Baldi. „Can Coupled Dark Energy Speed Up the Bullet Cluster?“ In: *ApJ in press, arXiv:1110.0015* (2011). ApJ Submitted. arXiv: 1110.0015 [astro-ph.CO].

[119] G. Lemaître. „Expansion of the universe, A homogeneous universe of constant mass and increasing radius accounting for the radial velocity of extra-galactic nebulae“. In: *MNRAS* 91 (Mar. 1931), pp. 483–490. DOI: 10.1093/mnras/91.5.483.

[120] B. Li and H. Zhao. „Structure formation by a fifth force: N-body versus linear simulations“. In: *Phys. Rev. D* 80.4, 044027 (Aug. 2009), p. 044027. DOI: 10.1103/PhysRevD.80.044027. arXiv: 0906.3880 [astro-ph.CO].

[121] Baojiu Li. „Voids in Coupled Scalar Field Cosmology“. In: *Mon.Not.Roy.Astron.Soc.* 411 (2011), p. 2615. arXiv: 1009.1406 [astro-ph.CO].

[122] Baojiu Li and John D. Barrow. „N-Body Simulations for Coupled Scalar Field Cosmology“. In: *Phys. Rev.* D83 (2011), p. 024007. DOI: 10.1103/PhysRevD.83.024007. arXiv: 1005.4231 [astro-ph.CO].

[123] M. LoVerde. „Halo bias in mixed dark matter cosmologies“. In: *Phys. Rev. D* 90.8, 083530 (Oct. 2014), p. 083530. DOI: 10.1103/PhysRevD.90.083530. arXiv: 1405.4855.

[124] Andrea V. Macciò, Claudia Quercellini, Roberto Mainini, Luca Amendola, and Silvio A. Bonometto. „N-body simulations for coupled dark energy: halo mass function and density profiles“. In: *Phys. Rev.* D69 (2004), p. 123516. DOI: 10.1103/PhysRevD.69.123516. arXiv: astro-ph/0309671.

[125] S. J. Maddox, G. Efstathiou, W. J. Sutherland, and J. Loveday. „Galaxy correlations on large scales“. In: *Mon. Not. Roy. Astron. Soc.* 242 (1990), pp. 43–49.

[126] A. Mana. *Optically selected galaxy clusters as cosmological probes*. Sept. 2013, p. 124.

[127] Q. Mao et al. „A Cosmic Void Catalog of SDSS DR12 BOSS Galaxies“. In: *ApJ* 835, 161 (Feb. 2017), p. 161. DOI: 10.3847/1538-4357/835/2/161. arXiv: 1602.02771.

[128] F. Marulli, M. Baldi, and L. Moscardini. „Clustering and redshift-space distortions in interacting dark energy cosmologies“. In: *MNRAS* 420 (Mar. 2012), pp. 2377–2386. DOI: 10.1111/j.1365-2966.2011.20199.x. arXiv: 1110.3045 [astro-ph.CO].

[129] T. McClintock et al. „Dark Energy Survey Year 1 Results: Weak Lensing Mass Calibration of redMaPPer Galaxy Clusters“. In: *ArXiv e-prints* (Apr. 2018). arXiv: 1805.00039.

[130] M. McDonald et al. „The Redshift Evolution of the Mean Temperature, Pressure, and Entropy Profiles in 80 SPT-Selected Galaxy Clusters“. In: *ApJ* 794, 67 (Oct. 2014), p. 67. DOI: 10.1088/0004-637X/794/1/67. arXiv: 1404.6250 [astro-ph.HE].

[131] P. McDonald and A. Roy. „Clustering of dark matter tracers: generalizing bias for the coming era of precision LSS“. In: *J. Cosmology Astropart. Phys.* 8, 020 (Aug. 2009), p. 020. DOI: 10.1088/1475-7516/2009/08/020. arXiv: 0902.0991 [astro-ph.CO].

[132] P. Melchior, P. M. Sutter, E. S. Sheldon, E. Krause, and B. D. Wandelt. „First measurement of gravitational lensing by cosmic voids in SDSS“. In: *MNRAS* 440 (June 2014), pp. 2922–2927. DOI: 10.1093/mnras/stu456. arXiv: 1309.2045.

[133] H. J. Mo and S. D. M. White. „An analytic model for the spatial clustering of dark matter haloes“. In: *MNRAS* 282 (Sept. 1996), pp. 347–361.

[134] M. Moresco, F. Marulli, M. Baldi, L. Moscardini, and A. Cimatti. „Disentangling interacting dark energy cosmologies with the three-point correlation function“. In: *MNRAS* 443 (Oct. 2014), pp. 2874–2886. DOI: 10.1093/mnras/stu1359. arXiv: 1312.4530.

[135] S. Nadathur and R. Crittenden. „A Detection of the Integrated Sachs-Wolfe Imprint of Cosmic Superstructures Using a Matched-filter Approach“. In: *ApJ* 830, L19 (Oct. 2016), p. L19. DOI: 10.3847/2041-8205/830/1/L19. arXiv: 1608.08638.

[136] S. Nadathur and S. Hotchkiss. „The nature of voids - I. Watershed void finders and their connection with theoretical models“. In: *MNRAS* 454 (Dec. 2015), pp. 2228–2241. DOI: 10.1093/mnras/stv2131. arXiv: 1504.06510.

[137] S. Nadathur and S. Hotchkiss. „The nature of voids - II. Tracing underdensities with biased galaxies“. In: *MNRAS* 454 (Nov. 2015), pp. 889–901. DOI: 10.1093/mnras/stv1994. arXiv: 1507.00197.

[138] S. Nadathur and W. J. Percival. „An accurate linear model for redshift space distortions in the void-galaxy correlation function“. In: *ArXiv e-prints* (Dec. 2017). arXiv: 1712.07575.

[139] S. Nadathur, M. Lavinto, S. Hotchkiss, and S. Räsänen. „Can a supervoid explain the cold spot?“ In: *Phys. Rev. D* 90.10, 103510 (Nov. 2014), p. 103510. DOI: 10.1103/PhysRevD.90.103510. arXiv: 1408.4720.

[140] Seshadri Nadathur. „Testing cosmology with a catalogue of voids in the BOSS galaxy surveys“. In: *Monthly Notices of the Royal Astronomical Society* 461.1 (2016), pp. 358–370. DOI: 10.1093/mnras/stw1340. eprint: /oup/backfile/content_public/

journal/mnras/461/1/10.1093_mnras_stw1340/2/stw1340.pdf. URL: +http://dx.doi.org/10.1093/mnras/stw1340.

[141] M. C. Neyrinck. „ZOBOV: a parameter-free void-finding algorithm“. In: *MNRAS* 386 (June 2008), pp. 2101–2109. DOI: 10.1111/j.1365-2966.2008.13180.x. arXiv: 0712.3049.

[142] M. C. Neyrinck, M. A. Aragón-Calvo, D. Jeong, and X. Wang. „A halo bias function measured deeply into voids without stochasticity“. In: *MNRAS* 441 (June 2014), pp. 646–655. DOI: 10.1093/mnras/stu589. arXiv: 1309.6641.

[143] A. Nusser, S. S. Gubser, and P. J. Peebles. „Structure formation with a long-range scalar dark matter interaction“. In: *Phys. Rev. D* 71.8, 083505 (Apr. 2005), p. 083505. DOI: 10.1103/PhysRevD.71.083505. eprint: astro-ph/0412586.

[144] C. O'Raifeartaigh and S. Mitton. „Einstein's "biggest blunder" - interrogating the legend“. In: *ArXiv e-prints* (Apr. 2018). arXiv: 1804.06768.

[145] A. Odrzywołek. „Holes in the static Einstein universe and a model of the cosmological voids“. In: *Phys. Rev. D* 80.10, 103515 (Nov. 2009), p. 103515. DOI: 10.1103/PhysRevD.80.103515. arXiv: 0909.4198 [astro-ph.CO].

[146] F. Pace, M. Baldi, L. Moscardini, D. Bacon, and R. Crittenden. „Ray-tracing simulations of coupled dark energy models“. In: *MNRAS* 447 (Feb. 2015), pp. 858–874. DOI: 10.1093/mnras/stu2513. arXiv: 1407.7548.

[147] N. D. Padilla, L. Ceccarelli, and D. G. Lambas. „Spatial and dynamical properties of voids in a Λ cold dark matter universe“. In: *MNRAS* 363 (Nov. 2005), pp. 977–990. DOI: 10.1111/j.1365-2966.2005.09500.x. eprint: astro-ph/0508297.

[148] K. Paech, N. Hamaus, B. Hoyle, M. Costanzi, T. Giannantonio, S. Hagstotz, G. Sauerwein, and J. Weller. „Cross-correlation of galaxies and galaxy clusters in the Sloan Digital Sky Survey and the importance of non-Poissonian shot noise“. In: *MNRAS* 470 (Sept. 2017), pp. 2566–2577. DOI: 10.1093/mnras/stx1354. arXiv: 1612.02018.

[149] D. C. Pan, M. S. Vogeley, F. Hoyle, Y.-Y. Choi, and C. Park. „Cosmic voids in Sloan Digital Sky Survey Data Release 7“. In: *MNRAS* 421 (Apr. 2012), pp. 926–934. DOI: 10.1111/j.1365-2966.2011.20197.x. arXiv: 1103.4156.

[150] A. Paranjape, O. Hahn, and R. K. Sheth. „Halo assembly bias and the tidal anisotropy of the local halo environment“. In: *ArXiv e-prints* (June 2017). arXiv: 1706.09906.

[151] P. J. E. Peebles. *The large-scale structure of the universe*. 1980.

[152] P. J. E. Peebles. „The Void Phenomenon“. In: *ApJ* 557 (Aug. 2001), pp. 495–504. DOI: 10.1086/322254. eprint: astro-ph/0101127.

[153] A. A. Penzias and R. W. Wilson. „A Measurement of Excess Antenna Temperature at 4080 Mc/s.“ In: *ApJ* 142 (July 1965), pp. 419–421. DOI: 10.1086/148307.

[154] S. Perlmutter et al. In: *ApJ* 517 (June 1999), pp. 565–586. DOI: 10.1086/307221. eprint: arXiv:astro-ph/9812133.

[155] V. Pettorino and C. Baccigalupi. „Coupled and extended quintessence: Theoretical differences and structure formation“. In: *Phys. Rev. D* 77.10 (May 2008), pp. 103003–+. DOI: 10.1103/PhysRevD.77.103003. arXiv: 0802.1086.

[156] A. Pisani, P. M. Sutter, N. Hamaus, E. Alizadeh, R. Biswas, B. D. Wandelt, and C. M. Hirata. „Counting voids to probe dark energy“. In: *ArXiv e-prints* (Mar. 2015). arXiv: 1503.07690.

[157] A. Pisani, P. M. Sutter, N. Hamaus, E. Alizadeh, R. Biswas, B. D. Wandelt, and C. M. Hirata. „Counting voids to probe dark energy“. In: *Phys. Rev. D* 92.8, 083531 (Oct. 2015), p. 083531. DOI: 10.1103/PhysRevD.92.083531. arXiv: 1503.07690.

[158] Planck Collaboration et al. „Planck intermediate results. V. Pressure profiles of galaxy clusters from the Sunyaev-Zeldovich effect“. In: *A&A* 550, A131 (Feb. 2013), A131. DOI: 10.1051/0004-6361/201220040. arXiv: 1207.4061.

[159] Planck Collaboration et al. „Planck 2013 results. XVI. Cosmological parameters“. In: *A&A* 571, A16 (Nov. 2014), A16. DOI: 10.1051/0004-6361/201321591. arXiv: 1303.5076.

[160] Planck Collaboration et al. „Planck 2015 results. I. Overview of products and scientific results“. In: *ArXiv e-prints* (Feb. 2015). arXiv: 1502.01582.

[161] E. Platen, R. van de Weygaert, and B. J. T. Jones. „A cosmic watershed: the WVF void detection technique“. In: *MNRAS* 380 (Sept. 2007), pp. 551–570. DOI: 10.1111/j.1365-2966.2007.12125.x. arXiv: 0706.2788.

[162] E. Platen, R. van de Weygaert, and B. J. T. Jones. „A cosmic watershed: the WVF void detection technique“. In: *MNRAS* 380 (Sept. 2007), pp. 551–570. DOI: 10.1111/j.1365-2966.2007.12125.x. arXiv: 0706.2788.

[163] D. Pogosyan, J. R. Bond, L. Kofman, and J. Wadsley. „Cosmic Web: Origin and Observables“. In: *Wide Field Surveys in Cosmology*. Ed. by S. Colombi, Y. Mellier, and B. Raban. 1998, p. 61. eprint: astro-ph/9810072.

[164] G. Pollina, M. Baldi, F. Marulli, and L. Moscardini. „Cosmic voids in coupled dark energy cosmologies: the impact of halo bias“. In: *MNRAS* 455 (Jan. 2016), pp. 3075–3085. DOI: 10.1093/mnras/stv2503. arXiv: 1506.08831.

[165] G. Pollina, N. Hamaus, K. Dolag, J. Weller, M. Baldi, and L. Moscardini. „On the linearity of tracer bias around voids“. In: *MNRAS* 469 (July 2017), pp. 787–799. DOI: 10.1093/mnras/stx785. arXiv: 1610.06176.

[166] G. Pollina et al. „On the relative bias of void tracers in the Dark Energy Survey“. In: *ArXiv e-prints* (June 2018). arXiv: 1806.06860.

[167] W. H. Press and P. Schechter. „Formation of Galaxies and Clusters of Galaxies by Self-Similar Gravitational Condensation“. In: *ApJ* 187 (Feb. 1974), pp. 425–438. DOI: 10.1086/152650.

[168] A. Pujol, K. Hoffmann, N. Jiménez, and E. Gaztañaga. „What determines large scale galaxy clustering: halo mass or local density?“ In: *A&A* 598, A103 (Feb. 2017), A103. DOI: 10.1051/0004-6361/201629121. arXiv: 1510.01692.

[169] J.-R. Pycke and E. Russell. „A New Statistical Perspective on the Cosmic Void Distribution“. In: *ApJ* 821, 110 (Apr. 2016), p. 110. DOI: 10.3847/0004-637X/821/2/110. arXiv: 1602.08770.

[170] B. Ratra and P. J. E. Peebles. „Cosmological consequences of a rolling homogeneous scalar field“. In: *Phys. Rev. D* 37 (June 1988), pp. 3406–3427. DOI: 10.1103/PhysRevD.37.3406.

[171] M. J. Rees, D. W. Sciama, and S. H. Stobbs. „Metastable Helium in Interstellar and Intergalactic Space“. In: *Astrophys. Lett.* 2 (1968), p. 243.

[172] R.-S. Remus, A. Burkert, and K. Dolag. „A 'Universal' Density Profile for the Outer Stellar Halos of Galaxies“. In: *Formation and Evolution of Galaxy Outskirts*. Ed. by A. Gil de Paz, J. H. Knapen, and J. C. Lee. Vol. 321. IAU Symposium. Mar. 2017, pp. 84–86. DOI: 10.1017/S1743921316011534. arXiv: 1605.06511.

[173] R.-S. Remus, A. Burkert, K. Dolag, P. H. Johansson, T. Naab, L. Oser, and J. Thomas. „The Dark HaloSpheroid Conspiracy and the Origin of Elliptical Galaxies“. In: *ApJ* 766, 71 (Apr. 2013), p. 71. DOI: 10.1088/0004-637X/766/2/71. arXiv: 1211.3420.

[174] E. Ricciardelli, V. Quilis, and S. Planelles. „The structure of cosmic voids in a ΛCDM Universe“. In: *MNRAS* 434 (Sept. 2013), pp. 1192–1204. DOI: 10.1093/mnras/stt1069. arXiv: 1306.2955 [astro-ph.CO].

[175] E. Ricciardelli, V. Quilis, and J. Varela. „On the universality of void density profiles“. In: *MNRAS* 440 (May 2014), pp. 601–609. DOI: 10.1093/mnras/stu307. arXiv: 1402.2976 [astro-ph.CO].

[176] A. G. Riess et al. „Observational Evidence from Supernovae for an Accelerating Universe and a Cosmological Constant“. In: *AJ* 116 (Sept. 1998), pp. 1009–1038. DOI: 10.1086/300499. eprint: arXiv:astro-ph/9805201.

[177] H. P. Robertson. „Kinematics and World-Structure“. In: *ApJ* 82 (Nov. 1935), p. 284. DOI: 10.1086/143681.

[178] T. Ronconi and F. Marulli. „Cosmological exploitation of cosmic void statistics. New numerical tools in the CosmoBolognaLib to extract cosmological constraints from the void size function“. In: *A&A* 607, A24 (Oct. 2017), A24. DOI: 10.1051/0004-6361/201730852. arXiv: 1703.07848.

[179] E. Rozo et al. „Constraining the Scatter in the Mass-richness Relation of maxBCG Clusters with Weak Lensing and X-ray Data“. In: *ApJ* 699 (July 2009), pp. 768–781. DOI: 10.1088/0004-637X/699/1/768. arXiv: 0809.2794.

[180] E. Rozo, E. Rykoff, B. Koester, B. Nord, H.-Y. Wu, A. Evrard, and R. Wechsler. „Extrinsic Sources of Scatter in the Richness-mass Relation of Galaxy Clusters“. In: *ApJ* 740, 53 (Oct. 2011), p. 53. DOI: 10.1088/0004-637X/740/2/53. arXiv: 1104.2090.

[181] E. Rozo et al. „redMaGiC: selecting luminous red galaxies from the DES Science Verification data“. In: *MNRAS* 461 (Sept. 2016), pp. 1431–1450. DOI: 10.1093/mnras/stw1281. arXiv: 1507.05460 [astro-ph.IM].

[182] E. S. Rykoff, B. P. Koester, E. Rozo, J. Annis, A. E. Evrard, S. M. Hansen, J. Hao, D. E. Johnston, T. A. McKay, and R. H. Wechsler. „Robust Optical Richness Estimation with Reduced Scatter“. In: *ApJ* 746, 178 (Feb. 2012), p. 178. DOI: 10.1088/0004-637X/746/2/178. arXiv: 1104.2089.

[183] E. S. Rykoff et al. „The RedMaPPer Galaxy Cluster Catalog From DES Science Verification Data“. In: *ApJS* 224, 1 (May 2016), p. 1. DOI: 10.3847/0067-0049/224/1/1. arXiv: 1601.00621.

[184] A. G. Sanchez et al. „The clustering of galaxies in the completed SDSS-III Baryon Oscillation Spectroscopic Survey: cosmological implications of the configuration-space clustering wedges“. In: *ArXiv e-prints* (July 2016). arXiv: 1607.03147.

[185] C. Sánchez et al. „Cosmic voids and void lensing in the Dark Energy Survey Science Verification data“. In: *MNRAS* 465 (Feb. 2017), pp. 746–759. DOI: 10.1093/mnras/stw2745. arXiv: 1605.03982.

[186] A. Saro et al. „Constraints on the CMB temperature evolution using multiband measurements of the Sunyaev-Zel'dovich effect with the South Pole Telescope". In: *MNRAS* 440 (May 2014), pp. 2610–2615. DOI: 10.1093/mnras/stu575. arXiv: 1312.2462.

[187] U. Seljak and M. S. Warren. „Large-scale bias and stochasticity of haloes and dark matter". In: *MNRAS* 355 (Nov. 2004), pp. 129–136. DOI: 10.1111/j.1365-2966.2004.08297.x. eprint: arXiv:astro-ph/0403698.

[188] R. K. Sheth, H. J. Mo, and G. Tormen. „Ellipsoidal collapse and an improved model for the number and spatial distribution of dark matter haloes". In: *MNRAS* 323 (May 2001), pp. 1–12. DOI: 10.1046/j.1365-8711.2001.04006.x. eprint: astro-ph/9907024.

[189] R. K. Sheth and G. Tormen. „Large-scale bias and the peak background split". In: *MNRAS* 308 (Sept. 1999), pp. 119–126.

[190] R. K. Sheth and G. Tormen. „An excursion set model of hierarchical clustering: ellipsoidal collapse and the moving barrier". In: *MNRAS* 329 (Jan. 2002), pp. 61–75. DOI: 10.1046/j.1365-8711.2002.04950.x. eprint: arXiv:astro-ph/0105113.

[191] R. K. Sheth and R. van de Weygaert. „A hierarchy of voids: much ado about nothing". In: *MNRAS* 350 (May 2004), pp. 517–538. DOI: 10.1111/j.1365-2966.2004.07661.x. eprint: astro-ph/0311260.

[192] J. Shi and R. K. Sheth. „Dependence of halo bias on mass and environment". In: *MNRAS* 473 (Jan. 2018), pp. 2486–2492. DOI: 10.1093/mnras/stx2277. arXiv: 1707.04096.

[193] P. Simon and S. Hilbert. „Scale dependence of galaxy biasing investigated by weak gravitational lensing: An assessment using semi-analytic galaxies and simulated lensing data". In: *ArXiv e-prints* (Nov. 2017). arXiv: 1711.02677.

[194] R. E. Smith, R. Scoccimarro, and R. K. Sheth. „Scale dependence of halo and galaxy bias: Effects in real space". In: *Phys. Rev. D* 75.6, 063512 (Mar. 2007), p. 063512. DOI: 10.1103/PhysRevD.75.063512. eprint: astro-ph/0609547.

[195] George F. Smoot, C.L. Bennett, A. Kogut, E.L. Wright, J. Aymon, et al. „Structure in the COBE differential microwave radiometer first year maps". In: *Astrophys.J.* 396 (1992), pp. L1–L5.

[196] D. Spolyar, M. Sahlén, and J. Silk. „Topology and Dark Energy: Testing Gravity in Voids". In: *Physical Review Letters* 111.24, 241103 (Dec. 2013), p. 241103. DOI: 10.1103/PhysRevLett.111.241103. arXiv: 1304.5239 [astro-ph.CO].

[197] V. Springel. „The cosmological simulation code GADGET-2“. In: *MNRAS* 364 (Dec. 2005), pp. 1105–1134. DOI: 10.1111/j.1365-2966.2005.09655.x. eprint: astro-ph/0505010.

[198] V. Springel and L. Hernquist. „Cosmological smoothed particle hydrodynamics simulations: the entropy equation“. In: *MNRAS* 333 (July 2002), pp. 649–664.

[199] V. Springel, S. D. M. White, G. Tormen, and G. Kauffmann. „Populating a cluster of galaxies - I. Results at [formmu2]z=0“. In: *MNRAS* 328 (Dec. 2001), pp. 726–750. DOI: 10.1046/j.1365-8711.2001.04912.x. eprint: arXiv:astro-ph/0012055.

[200] V. Springel et al. „First results from the IllustrisTNG simulations: matter and galaxy clustering“. In: *MNRAS* 475 (Mar. 2018), pp. 676–698. DOI: 10.1093/mnras/stx3304. arXiv: 1707.03397.

[201] Volker Springel. „The cosmological simulation code GADGET-2“. In: *Mon. Not. Roy. Astron. Soc.* 364 (2005), pp. 1105–1134. arXiv: astro-ph/0505010.

[202] L. K. Steinborn, K. Dolag, M. Hirschmann, M. A. Prieto, and R.-S. Remus. „A refined sub-grid model for black hole accretion and AGN feedback in large cosmological simulations“. In: *MNRAS* 448 (Apr. 2015), pp. 1504–1525. DOI: 10.1093/mnras/stv072. arXiv: 1409.3221.

[203] L. K. Steinborn, K. Dolag, J. M. Comerford, M. Hirschmann, R.-S. Remus, and A. F. Teklu. „Origin and properties of dual and offset active galactic nuclei in a cosmological simulation at z=2“. In: *MNRAS* 458 (May 2016), pp. 1013–1028. DOI: 10.1093/mnras/stw316. arXiv: 1510.08465.

[204] P. M. Sutter, G. Lavaux, B. D. Wandelt, and D. H. Weinberg. „A First Application of the Alcock-Paczynski Test to Stacked Cosmic Voids“. In: *ApJ* 761, 187 (Dec. 2012), p. 187. DOI: 10.1088/0004-637X/761/2/187. arXiv: 1208.1058 [astro-ph.CO].

[205] P. M. Sutter, G. Lavaux, B. D. Wandelt, and D. H. Weinberg. „A Public Void Catalog from the SDSS DR7 Galaxy Redshift Surveys Based on the Watershed Transform“. In: *ApJ* 761, 44 (Dec. 2012), p. 44. DOI: 10.1088/0004-637X/761/1/44. arXiv: 1207.2524.

[206] P. M. Sutter, A. Pisani, B. D. Wandelt, and D. H. Weinberg. „A measurement of the Alcock-Paczyński effect using cosmic voids in the SDSS“. In: *MNRAS* 443 (Oct. 2014), pp. 2983–2990. DOI: 10.1093/mnras/stu1392. arXiv: 1404.5618.

[207] P. M. Sutter, G. Lavaux, N. Hamaus, B. D. Wandelt, D. H. Weinberg, and M. S. Warren. „Sparse sampling, galaxy bias, and voids“. In: *MNRAS* 442 (July 2014), pp. 462–471. DOI: 10.1093/mnras/stu893. arXiv: 1309.5087.

[208] P. M. Sutter, G. Lavaux, B. D. Wandelt, D. H. Weinberg, and M. S. Warren. „The dark matter of galaxy voids“. In: *MNRAS* 438 (Mar. 2014), pp. 3177–3187. DOI: 10.1093/mnras/stt2425. arXiv: 1311.3301.

[209] P. M. Sutter, E. Carlesi, B. D. Wandelt, and A. Knebe. „On the observability of coupled dark energy with cosmic voids“. In: *MNRAS* 446 (Jan. 2015), pp. L1–L5. DOI: 10.1093/mnrasl/slu155. arXiv: 1406.0511.

[210] P. M. Sutter, G. Lavaux, N. Hamaus, A. Pisani, B. D. Wandelt, M. Warren, F. Villaescusa-Navarro, P. Zivick, Q. Mao, and B. B. Thompson. „VIDE: The Void IDentification and Examination toolkit“. In: *Astronomy and Computing* 9 (Mar. 2015), pp. 1–9. DOI: 10.1016/j.ascom.2014.10.002. arXiv: 1406.1191.

[211] I. Szapudi, S. Prunet, D. Pogosyan, A. S. Szalay, and J. R. Bond. „Fast Cosmic Microwave Background Analyses via Correlation Functions“. In: *ApJ* 548 (Feb. 2001), pp. L115–L118. DOI: 10.1086/319105.

[212] A. F. Teklu, R.-S. Remus, K. Dolag, A. M. Beck, A. Burkert, A. S. Schmidt, F. Schulze, and L. K. Steinborn. „Connecting Angular Momentum and Galactic Dynamics: The Complex Interplay between Spin, Mass, and Morphology“. In: *ApJ* 812, 29 (Oct. 2015), p. 29. DOI: 10.1088/0004-637X/812/1/29. arXiv: 1503.03501.

[213] The Dark Energy Survey Collaboration. „The Dark Energy Survey“. In: *ArXiv Astrophysics e-prints* (Oct. 2005). eprint: astro-ph/0510346.

[214] J. L. Tinker and C. Conroy. „The Void Phenomenon Explained“. In: *ApJ* 691 (Jan. 2009), pp. 633–639. DOI: 10.1088/0004-637X/691/1/633. arXiv: 0804.2475.

[215] J. L. Tinker, B. E. Robertson, A. V. Kravtsov, A. Klypin, M. S. Warren, G. Yepes, and S. Gottlöber. „The Large-scale Bias of Dark Matter Halos: Numerical Calibration and Model Tests“. In: *ApJ* 724 (Dec. 2010), pp. 878–886. DOI: 10.1088/0004-637X/724/2/878. arXiv: 1001.3162.

[216] G. Tormen. *Formazione di Strutture Cosmiche*. Mar. 2002, p. 92.

[217] Steven Weinberg. „The cosmological constant problem“. In: *Reviews of Modern Physics* 61.1 (1989), p. 1.

[218] J. Weller. *Cosmology And Large Scale Structure*. Oct. 2012, p. 80.

[219] C. Wetterich. „Cosmology and the fate of dilatation symmetry“. In: *Nuclear Physics B* 302 (June 1988), pp. 668–696. DOI: 10.1016/0550-3213(88)90193-9.

[220] Christof Wetterich. „The Cosmon model for an asymptotically vanishing time dependent cosmological 'constant'". In: *Astron. Astrophys.* 301 (1995), pp. 321–328. arXiv: hep-th/9408025.

[221] R. Wojtak, D. Powell, and T. Abel. „Voids in cosmological simulations over cosmic time". In: *MNRAS* 458 (June 2016), pp. 4431–4442. DOI: 10.1093/mnras/stw615. arXiv: 1602.08541.

[222] X. Yang, Y. Zhang, T. Lu, H. Wang, F. Shi, D. Tweed, S. Li, W. Luo, Y. Lu, and L. Yang. „Revealing the Cosmic Web-dependent Halo Bias". In: *ApJ* 848, 60 (Oct. 2017), p. 60. DOI: 10.3847/1538-4357/aa8c7a. arXiv: 1704.02451.

[223] A. R. Zentner. „The Excursion Set Theory of Halo Mass Functions, Halo Clustering, and Halo Growth". In: *International Journal of Modern Physics D* 16 (2007), pp. 763–815. DOI: 10.1142/S0218271807010511. eprint: astro-ph/0611454.

[224] W. J. G. de Blok. „The Core-Cusp Problem". In: *Advances in Astronomy* 2010, 789293 (2010), p. 5. DOI: 10.1155/2010/789293. arXiv: 0910.3538 [astro-ph.CO].

No man is an Iland, intire of itselfe; every man is a peece of the Continent, a part of the maine; if a Clod bee washed away by the Sea, Europe is the lesse, as well as if a Promontorie were, as well as if a Manor of thy friends or of thine owne were; any mans death diminishes me, because I am involved in Mankinde; And therefore never send to know for whom the bell tolls; It tolls for thee.

MEDITATION XVII
"Devotions upon Emergent Occasions"
John Donne

ACKNOWLEDGEMENTS

This work has benefited from financial support, infrastructures and opportunities provided by the DFG Cluster of Excellence "Origin and Structure of the Universe", the Transregio programme TR33 "The Dark Universe" and the Dark Energy Survey Collaboration.

On a more personal note, I would like to express my gratitude to the many people that were part of my tribe during these years (and please be aware that there might be many typos around here, as this has been written at the very last minute).

First of all, I am sincerely thankful to my supervisor, Professor Jochen Weller, for four wonderful years of support, fundamental and very motivating scientific discussions and loads of fun. Thank you for keeping always the spirit up, for always being open to find a solution to everything, for being supportive and spreading enthusiasm also when the typical PhD depressive phase – that I'm guessing everybody has experienced at least once – kicks in. My choice of picking this PhD position was mostly based on the impression I got of my (back then) potential supervisor, which was very right. By all means I think I won the lottery by having such a nice, understanding person and expert scientist as boss during these years.

I owe a very special thanks to Dr. Nico Hamaus for countless hours of discussion, for being always incredibly helpful, patient and available for advises during the development of my PhD projects, in which he was always closely involved.

All people I've shared something with during these years somehow contributed to this results, but I feel really obliged to thank for a lot

support and laughters my office mates Steffen Hagstotz (although I still don't know how the heck to spell his surname without checking on the office's door!), Tea Tutis, and the recurring office guests Korbinian Huber and Raffaella Capasso. Also, I would like to thank the members of our research group Ben Hoyle, Kerstin Paech and Matteo Costanzi for making this group so enjoyable, all my co-authors, and everybody else at the USM, in particular Tadziu, Keith, Adi and the staff of the Sekretariat Uta, Gudrun, Nicola, Sabine for being always extremely kind and helpful.

I thank my parents Croce and Gianni, for always being there and do what parents do.

I thank all the new and old friends I've met in Munich and around the World during these years, who I don't have the strength or the time to name one by one, as I really have to go and print this thing now! But really, thank you.

Finally, I thank Francesco for his glorious and majestic beard, that is my sweet and warm home.